

Realization of half-metallicity in disorder controlled Full Heusler compound Fe_2TiSn

A THESIS

*Submitted in partial fulfilment of the
requirements for the award of the degree
of*

DOCTOR OF PHILOSOPHY

By

SAYAN CHAUDHURI



DISCIPLINE OF PHYSICS

INDIAN INSTITUTE OF TECHNOLOGY INDORE

December 2019



INDIAN INSTITUTE OF TECHNOLOGY INDORE

CANDIDATE'S DECLARATION

I hereby certify that the work which is being presented in the thesis entitled **REALIZATION OF HALF METALLICITY IN DISORDER CONTROLLED FULL HEUSLER ALLOY Fe_2TiSn** in the partial fulfillment of the requirements for the award of the degree of **DOCTOR OF PHILOSOPHY** and submitted in the **DISCIPLINE OF PHYSICS, Indian Institute of Technology Indore**, is an authentic record of my own work carried out during the time period from December, 2014 to December, 2019 under the supervision of Dr. Preeti A. Bhohe, Associate Professor, Discipline of Physics, Indian Institute of Technology Indore.

The matter presented in this thesis has not been submitted by me for the award of any other degree of this or any other institute.

Sayan Chaudhuri

(SAYAN CHAUDHURI)

This is to certify that the above statement made by the candidate is correct to the best of my knowledge.

P. A. Bhohe

(Dr. PREETI A. BHOBE)

SAYAN CHAUDHURI has successfully given his Ph.D. Oral Examination held on 28th May 2020

Signature of Chairperson (OEB)

Date:

[Signature]
Signature of External Examiner

Date: 28-5-20

Signature(s) of Thesis Supervisor(s)

Date:

Signature of PSPC Member #1

Date:

Signature of PSPC Member #2

Date:

Signature of Convener, DPGC

Date:

Signature of Head of Discipline

Date:

Dedicated

to

My Parents

Acknowledgements

I take this opportunity to profoundly acknowledge my thesis supervisor Dr. Preeti A. Bhobe. This accomplishment would not have been possible without her constant support, guidance and active involvement. I am very thankful for her patience which she dealt with me during my hard time, her critical remarks and valuable suggestions.

I am extremely grateful to Prof. A. K. Nigam, Department of Condensed Matter and Material Science, Tata Institute of Fundamental Research Center, Mumbai for extending the facilities required for my thesis work. I also thank Mr. Devendra Buddhikot for his technical help during the measurements.

I am extremely thankful to Prof. Kaustav R. S. Priolkar for his crucial inputs and help in measurements in various stages of the thesis work.

I want to thank my PSPC members Dr. Somaditya Sen, Dr. Anabarasu M. and Dr. Rupesh Devan for their valuable suggestions, insightful comments and encouragement.

I would also like to thank all the faculty members and staff members of the IIT Indore for their help and support. I am very thankful to the Physics Discipline of IIT Indore for providing me all required facilities.

I would like to thank my lab members Priyadarshini, Mithunda, Gowtham and Tamalika for their help and encouragement. A special appreciation goes to Tamalika for her very crucial comments in research paper in several times.

I want to thank Prof. Aparna Chakraborty and Dr. Tufan Roy, RRCAT Indore for discussion and suggestions on theoretical calculations.

Also I would like to acknowledge Shweta Jindal and Sourav Kumar for helping me in learning DFT and the calculation software.

I must thank Mr. P. K. Parthiban, Mr. Nitin Upadhyay, Mr. Kinny Pandey for helping me in sample preparation process and Powder XRD and EDX measurements in Sophisticated Instrument center (SIC) at IIT Indore.

I gratefully acknowledge Ministry of Human Resource Development, Govt. of India and Council of Scientific and Industrial Research, Govt. of India for providing me the fellowship.

A special mention of profound thanks to all of my friend in IIT Indore. I acknowledge Amitesh, Shweta, Siddhartha, Hasan, Kushalda, Sujata for their constant support and cooperation during the stay.

Finally I would like to acknowledge my parents and my brother for all the blessings, love and care.

(Sayan Chaudhuri)

List of publications related to PhD thesis:

1. “Possible half-metallicity and variable range hopping transport in Sb-substituted Fe_2TiSn Heusler alloys”
Sayan Chaudhuri, P. A. Bhobe, A. K. Nigam,
J. Phys.: Cond. Matter. Vol. 30(1), 015703 (2018).
DOI: <https://doi.org/10.1088/1361-648X/aa9c10> IF: 2.711
2. “Unraveling the physical properties and superparamagnetism in anti-site disorder controlled Fe_2TiSn ”
Sayan Chaudhuri, P. A. Bhobe, Arpan Bhattacharya, A. K. Nigam
J. Phys.: Cond. Matter. Vol. 31(4), 045801 (2019).
DOI: <https://doi.org/10.1088/1361-648X/aaf0c7> IF: 2.711
3. “Origin of the magnetic ground state developed upon Si, Ge, and Sb-substitution at Sn site in Fe_2TiSn ”
Sayan Chaudhuri, V. Srihari, A. K. Nigam, P. A. Bhobe,
J. Appl. Phys. Vol. 126 (8), 083904 (2019).
DOI: <https://doi.org/10.1063/1.5110229> IF: 2.328
4. “Evolution of magnetic ordering and half metallicity in Cr substituted Fe_2TiSn ”
Sayan Chaudhuri, P. A. Bhobe
To be submitted soon

Conference proceedings:

1. “Electronic properties of $\text{Fe}_2\text{TiSn}_{1-x}\text{Si}_x$ ”
Sayan Chaudhuri, P. A. Bhobe, A. K. Nigam,
AIP Conf. Proc. Vol. 1832 (1), 110027 (2017).
DOI: <https://doi.org/10.1063/1.4980651> IF: 0.4

List of publications outside PhD thesis:

1. “ Structural, electronic, magnetic, and transport properties of the equiatomic Ni-based quaternary Heusler alloys”
Tamalika Samanta, **Sayan Chaudhuri**, Sukriti Singh, V. Srihari,
A. K. Nigam, Preeti A. Bhobe
Journal of Alloys and Compounds
DOI: <https://doi.org/10.1016/j.jallcom.2019.153029> IF: 3.779
2. “ Electronic structure and magnetic properties of a new quaternary Heusler alloy: NiFeTiGa”
Tamalika Samanta, **Sayan Chaudhuri**, Sukriti Singh, V. Srihari,
A. K. Nigam, Preeti A. Bhobe
Accepted in AIP Conference Proceedings

Presentation at conferences/meetings:

1. Presented poster at DAE Solid State Physics Symposium(DAE SSPS 2016), on “Electronic properties of $\text{Fe}_2\text{TiSn}_{1-x}\text{Si}_x$ ” , KIT, Bhubaneswar;
2. Presented poster at Euro-Asian symposium in Trends in Magnetism (EASTMAG 2019) on “Half metallic ferromagnetism in Sb substituted Fe_2TiSn ”, Institute of Metal Physics, Russia;

Achievement

1. Awarded CSIR-SRF Fellowship.
2. International travel grant from DST-SERB (2019) for attending conference.

Contents

Acknowledgements	iii
Figures	x
Tables	xviii
1 Introduction	1
1.1 Spintronics	1
1.2 Half metallic ferromagnet	3
1.3 Heusler alloy	4
1.3.1 Fe ₂ TiSn: An interesting Full-Heusler alloy	11
1.4 Aim of the research work	12
2 Experimental techniques and computational details	15
2.1 Preamble	15
2.2 Experimental Techniques	16
2.2.1 Sample Preparation	16
2.2.2 Powder X-Ray Diffraction	17
2.2.3 Energy Dispersive X-ray Spectroscopy	19
2.2.4 X-ray Absorption Fine Structure	20
2.2.5 Magnetic property measurements	24
2.2.6 Transport properties measurement	26

2.3	Theoretical Techniques	29
2.3.1	Density Functional Theory	29
2.3.2	Quantum Espresso	31
2.3.3	SPR-KKR	32
3	Study of anti-site disorder in Fe₂TiSn	35
3.1	Preamble	35
3.2	Results	36
3.2.1	Structural analysis	36
3.2.2	Seebeck Coefficient	41
3.2.3	Resistivity	42
3.2.4	Heat capacity	46
3.2.5	Magnetism	49
3.3	Summary	53
4	Half metallicity in Sb substituted Fe₂TiSn	55
4.1	Preamble	55
4.2	Results and Discussion	56
4.2.1	X-Ray diffraction analysis	56
4.2.2	Resistivity analysis	58
4.2.3	Density of States calculation	63
4.3	Summary	67
5	On the origin of magnetic ordering in Z site substituted Fe₂TiSn	69
5.1	Preamble	69
5.2	Results and discussion	70
5.2.1	X-ray diffraction analysis	70

5.2.2	Resistivity measurement	72
5.2.3	Magnetic measurement	75
5.2.4	Local structure measurements	79
5.2.5	Theoretical calculations	82
5.3	Summary	86
6	Half-metallicity in Cr substituted Fe_2TiSn	87
6.1	Preamble	87
6.2	Results and Discussion	88
6.2.1	X ray diffraction	88
6.2.2	Magnetic properties	90
6.2.3	Heat capacity Measurement	97
6.2.4	Local structure analysis	100
6.2.5	Theoretical calculation	106
6.2.6	Resistivity Measurement	108
6.2.7	Magnetoresistance	111
6.2.8	Summary	114
7	Conclusions and Future scope	115
7.1	Preamble	115
7.2	Major findings	115
7.3	Future scope	117
8	Appendix	119
8.1	Preamble	119
8.2	Resistivity measurement set up	119
8.3	Seebeck co-efficient measurement set up	120
	References	123

Figures

1.1	Schematic diagram of electronic states near Fermi level for metal, semiconductor and half metallic systems.	4
1.2	Density of states for Fe_2TiSb , an HMF system.	4
1.3	Cubic struture of a Heusler system.	5
1.4	Illustration of atom exchange of different types of chemical disordering in the unit cell.	7
1.5	d - d hybridization scheme in Fe_2TiZ	9
1.6	Calculated total magnetic moment for some half metallic Heusler alloys. The dotted line represents the Slater–Pauling line [26].	11
2.1	(a)Image of the Arc melting furnace used. (b) A close up view of the melting chamber.	16
2.2	A quartz ampule with a sample bead inside. A measuring scale is placed to indicate the size of the ampoule.	17
2.3	The X–ray absorption mechanism showing the absorption and scattering of X–ray wave from atom. [85].	21
2.4	A typical XAFS data for Fe_2TiSn is shown. (a)Fisrt the raw data is background subtracted and normalized. (b)Trnasformed into k space and scaled by k^2 to magnify the subtle features. (c)Fourier transformation into R space (d) Inverse Fourier transformed into $k(q)$ space again. . . .	22

2.5	(a)Schematics of SQUID device demonstrating the working principle. [1] and (b) showing the working of the magnetometer. [10].	25
2.6	(a)Schematic diagram of a four probe resistivity measurement system. [2].	27
2.7	Schematic diagram of the heat capacity measurement technique. [3]	28
3.1	(a)XRD patterns of $\text{Fe}_{2-x}\text{Ti}_{1+x}\text{Sn}$ series recorded using Mo-target along with the Rietveld refinement fitting.	37
3.2	Left axis: Extent of order parameters as a function of Ti concentration. Right axis: variation in the FWHM of the XRD peaks in $\text{Fe}_{2-x}\text{Ti}_{1+x}\text{Sn}$ series	37
3.3	Change in intensity of the 111 peak for X ray wavelength of 7132 eV, Inset shows the normalized intensity variation for two X ray incident energies.	40
3.4	Seebeck coefficient as a function of temperature for $\text{Fe}_{2-x}\text{Ti}_{1+x}\text{Sn}$ series.	42
3.5	Resistivity measured as a function of temperature for $\text{Fe}_{2-x}\text{Ti}_{1+x}\text{Sn}$ series.	43
3.6	Fit to $\rho(T)$ of Fe_2TiSn in the low temperature regime (for $H = 0, 5 \text{ T}$) for two nominal compositions, showing the presence of weak localization.	44
3.7	Fitting of the high temperature $\rho(T)$ for two nominal Ti – substituted compositions showing $\rho(T) = AT^{\frac{5}{3}} + B$ dependence.	44
3.8	Heat capacity measured as a function of temperature for $\text{Fe}_{2-x}\text{Ti}_{1+x}\text{Sn}$ series.	47
3.9	$C_P = \gamma T + \beta T^3$ fit to the low temperature data of all the compositions.	48

3.10	Linear variation of C_P with $T \log(T)$ in the high temperature regime.	48
3.11	(a) M–H curves for $\text{Fe}_{2-x}\text{Ti}_{1+x}\text{Sn}$ recorded at 5 K. (b) Fit to the M vs H/T curve at 5K using the Langevin equation (see text for details).	49
3.12	Average magnetic moment per cluster extracted from the fitting to M(H) plots in $\text{Fe}_{2-x}\text{Ti}_{1+x}\text{Sn}$ series.	51
3.13	AC susceptibility as function of temperature for $\text{Fe}_{2-x}\text{Ti}_{1+x}\text{Sn}$. Inset shows the susceptibility data for Fe_2TiSn sample measured at different frequencies.	51
4.1	Powder XRD patterns of $\text{Fe}_2\text{TiSn}_{1-x}\text{Sb}_x$ ($x = 0, 0.1, 0.25, 0.5, 0.6$) series with Rietveld refinement fitting.	57
4.2	Right axis in the figure shows Lattice constant versus Sb concentration following Vegard’s law, left axis are for Intensity ratios of the (111) and (200) peaks with the main (222) peak versus Sb concentration. The lines are guide to the eye.	57
4.3	Resistivity of $\text{Fe}_2\text{TiSn}_{1-x}\text{Sb}_x$ series. (a) Absolute resistivity as a function of temperature of $x = 0$ and 0.1 samples to show the order of change with doping. (b) Resistivity of all samples versus temperature normalized by their value at 380 K.	58
4.4	(a) Fitted curve for low temperature resistivity of Fe_2TiSn sample, solid line indicates the fit to the equation $\rho(T) = A + BT + CT^5 - D\sqrt{T}$. Inset: Effect of application of magnetic field on the low temperature resistivity of same sample, (b) Effect of application of magnetic field on the resistivity of $\text{Fe}_2\text{TiSn}_{0.75}\text{Sb}_{0.25}$ sample.	59
4.5	$\text{MR} = \frac{\rho(H) - \rho(0)}{\rho(0)} \times 100\%$ as a function of applied magnetic field for $\text{Fe}_2\text{TiSn}_{1-x}\text{Sb}_x$ samples.	60

4.6	Fitted curves of $\ln(\sigma)$ versus $T^{-\frac{1}{4}}$ for (a) $x=0.25$, (b) $x = 0.5$ and (c) $x = 0.6$ samples with and without the application of magnetic field. Solid line indicates the linear fit. Value of characteristic temperature obtained from the fit are shown in the graph.	62
4.7	Fitted curves for high temperature resistivity as a function of temperature. (a) $x = 0$, (b) $x = 0.6$. Solid line indicates the fit to the equation $\rho(T) = \rho_0 + \rho_{ep}T + \rho_{em}T^2$	62
4.8	Calculated total DOS for $\text{Fe}_2\text{TiSn}_{1-x}\text{Sb}_x$ samples. x values are shown in the graph.	64
4.9	Hall resistivity versus temperature for $\text{Fe}_2\text{TiSn}_{0.75}\text{Sb}_{0.25}$ samples. (a) $x = 0$, (b) $x = 0.1$, (c) $x = 0.25$, (d) $x = 0.6$	65
4.10	Charge carrier density of $\text{Fe}_2\text{TiSn}_{1-x}\text{Sb}_x$ samples as a function of Sb concentration measured at 10 K.	65
4.11	Fitted graph of anomalous hall resistivity (ρ_{xy}^{AHE}) versus zero field resistivity (ρ_{xx}), Solid line indicates the fitting with the equation $\rho_{xy}^{AHE}(H) = C(\rho - \rho_R)^2$	66
5.1	Synchrotron X-ray diffraction ($\lambda = 0.776 \text{ \AA}$) patterns obtained for $\text{Fe}_2\text{TiSn}_{0.95}\text{M}_{0.05}$ with $M = \text{Si}$ and Ge	70
5.2	Resistivity measured as a function of temperature for (a) $\text{Fe}_2\text{TiSn}_{0.95}\text{M}_{0.05}$ ($M = \text{Si}, \text{Ge}$) and, (b) $\text{Fe}_2\text{TiSn}_{1-x}\text{Sb}_x$ ($x = 0.25, 0.5$) compositions.	72
5.3	Low temperature region of resistivity data for $\text{Fe}_2\text{TiSn}_{0.95}\text{M}_{0.05}$ ($M = \text{Si}, \text{Ge}$), fitted with the equation given in the text. Bottom panels represent the data recorded with the application of constant magnetic field of 5 T.	73
5.4	χ_{ac} recorded as a function of temperature for $\text{Fe}_2\text{TiSn}_{1-x}\text{Sb}_x$ (left panel) and $\text{Fe}_2\text{TiSn}_{0.95}\text{M}_{0.05}$ ($M = \text{Si}, \text{Ge}$) (right panel). The frequency dependence of peak-like feature at the blocking temperature is shown in the inset.	75

5.5	M–H curves recorded at 10 K for all the studied compositions.	77
5.6	(a) M vs. H/T fitted using modified Langevin’s function and (b) measured values of saturation magnetization (M_S) plotted along with the Slater-Pauling empirical rule (dotted line) for the Sb–substituted compositions.	77
5.7	k^2 weighted raw Fe K–edge EXAFS spectra for all the present compositions.	80
5.8	Fe K–edge EXAFS spectra fitted in real and k space for all the compositions investigated here.	80
5.9	Heisenberg exchange coupling parameter, J_{ij} , plotted against Fe – Fe and Fe – Ti distance normalized to the lattice parameter, in Fe_2TiSn (solid line) and 50% Sb substituted (dotted line) composition (see text for details).	83
5.10	Spin projected total and partial DOS for pristine Fe_2TiSn . For clarity of the figure, partial DOS for Sn p -states is shown in the lower panel.	85
5.11	Spin projected total and partial DOS for 50% Sb substituted Fe_2TiSn . For clarity of the figure, partial DOS for Sn and Sb p -states is shown in the lower panels.	85
6.1	X ray diffraction pattern for $\text{Fe}_2\text{Ti}_{1-x}\text{Cr}_x\text{Sn}$ composition recorded using synchrotron based source. Rietveld refinement of the XRD pattern for all compositions are also shown.	89
6.2	Change in lattice parameter and intensity ratio of $\frac{I_{200}}{I_{200}}$ with concentration of Cr.	89
6.3	(Main Panel) Zero field cooling curve as a function of temperature measured for all prepared composition. (Insets) ZFC and FC curves for (upper) $x = 0$ and (lower) $x = 0.25$ compositions to highlight the bifurcation.	90
6.4	χ_{ac} as a function of temperature for $\text{Fe}_2\text{Ti}_{1-x}\text{Cr}_x\text{Sn}$ series. .	93

6.5	Inverse magnetic susceptibility as a function of temperature for $\text{Fe}_2\text{Ti}_{1-x}\text{Cr}_x\text{Sn}$ series.	93
6.6	Inverse magnetic susceptibility as a function of temperature for $\text{Fe}_2\text{Ti}_{1-x}\text{Cr}_x\text{Sn}$ compositions. The solid line represents a guide to the eye to show the intersection at temperature axis.	95
6.7	(Main Panel) Zero field cooling curve as a function of temperature measured for all prepared composition. (Insets) ZFC and FC curves for (upper) $x = 0$ and (lower) $x = 0.25$ compositions to highlight the bifurcation.	96
6.8	Specific heat as a function of temperature of $\text{Fe}_2\text{Ti}_{1-x}\text{Cr}_x\text{Sn}$ compositions. Inset (a) shows the low temperature upturn in C/T	98
6.9	Low temperature heat capacity data fitted with the equation $C(T) = C_0 + \gamma T + \beta T^3 + \delta T^5$. The extracted parameters are summarized in Tab. 6.2.	98
6.10	EXAFS patterns measured at 30 K for $\text{Fe}_2\text{Ti}_{1-x}\text{Cr}_x\text{Sn}$ compositions.	100
6.11	EXAFS patterns measured at 30 K for $\text{Fe}_2\text{Ti}_{1-x}\text{Cr}_x\text{Sn}$ compositions.	102
6.12	EXAFS patterns measured at different temperatures for $\text{Fe}_2\text{Ti}_{0.75}\text{Cr}_{0.25}\text{Sn}$ compositions.	102
6.13	(a) XANES pattern for $\text{Fe}_2\text{Ti}_{1-x}\text{Cr}_x\text{Sn}$ compositions at 30 K temperature. (b) Simulated XANES patterns for Fe_2TiSn and Fe_2CrSn	104
6.14	Heisenberg exchange coupling parameter, J_{ij} , plotted against Fe–Fe, Fe–Cr and Fe–Ti distance normalized to the lattice parameter, in Fe_2TiSn (solid line) and 25% Cr–substituted composition.	105
6.15	Spin projected total and partial DOS for pristine Fe_2TiSn composition.	107

6.16	Spin projected total and partial DOS for 25% Cr substituted Fe ₂ TiSn. For clarity pDOS of the Cr <i>d</i> state is shown in the lower panel.	107
6.17	Variation of resistivity as a function of temperature for all prepared compositions of Fe ₂ Ti _{1-x} Cr _x Sn series. The dotted line represents $\rho(T)$ under the application of 5T magnetic field.	109
6.18	Power law fitting of resistivity for two nominal compositions, the red line represents the fitting. Fitting equation and values of the α are shown in the figure.	113
6.19	(a) Magnetoresistance of the prepared compositions as a function of temperature. inset shows the same as a function of applied magnetic field. (b) MR of the 25% Cr substituted Fe ₂ TiSn measured at different temperatures.	113
8.1	Resistivity measurement probe with a standard sample mounted on it.	119
8.2	Resistivity measurement probe with a standard sample mounted on it.	121
8.3	Front panel of resistivity measurement program in LabView.	121
8.4	Schematic of the seebeck co-efficient measurement set-up. . .	122
8.5	The seebeck co-efficient measurement set-up.	122
8.6	Front panel of the seebeck co-efficient measurement set-up program in LabView.	122

Tables

1.1	Different Heusler alloys with their respective atomic arrangement.	6
3.1	Lattice parameters obtained from the Rietveld refinement, goodness of fit parameters (R_{Bragg} and χ^2), Order parameters for $L2_1$ order calculated from peak intensities and FWHM of the peak in the XRD pattern.	39
4.1	Lattice parameter obtained from reitveld refinement of the XRD patterns and the fitting parameters obtained from the fit shown in figure (4.7).	58
5.1	Lattice parameters obtained from the Rietveld refinement of the XRD profiles, goodness of fit parameters (R_{Bragg} and χ^2)	71
5.2	Electrical resistivity fitting parameters obtained for the prepared compositions.	74
5.3	Magnetic moment values measured from $M(H)$ data (M_{exp}), calculated using DFT (M_{cal}), and estimated by from modified Lagrangian fit ($M_{cluster}$), for the present compositions. .	78
5.4	Bond distances, thermal mean square variation (σ^2), coordination number (CN),extracted from EXAFS data fitting. .	81
6.1	Lattice parameter and goodness of fit parameters for Rietveld refinement of XRD profiles.	88
6.2	Fitting parameters for magnetization data.	95

6.3	Heat capacity fitting parameters obtained for the prepared compositions.	100
6.4	Bond distances, thermal mean square variation (σ^2), coordination number (CN), extracted from EXAFS data fitting of $\text{Fe}_2\text{Ti}_{1-x}\text{Cr}_x\text{Sn}$ samples measured at 30K. Values of x are shown in the table.	103

Chapter 1

Introduction

1.1 Spintronics

Magnetic materials have been the focus of immense research interest for many decades due to their multipurpose applications in practical devices. Among various possibilities, magnetic recording is by far the most significant technological application of the magnetic materials. Continuous industrial demand for smaller size, more reliable, more memory capable, cheaper and more energy efficient memory devices keeps the research in this area thriving even today.

Moor's law states that any electronic device becomes half by size in each 1.5 years [53]. Although a huge amount of research is going on to increase the areal density (quantity of information stored in bits per length) of a memory device, over the time it is getting saturated, due to superparamagnetic limit. Superparamagnetic limit is the lowest value of magnetic anisotropy, below which the magnetic moments in the system get spontaneously reversed due to the thermal fluctuation. Increasing the areal density decreases magnetic anisotropy of a system. To avoid the limit, a number of different approaches, like using higher uniaxial anisotropy material, or using longitudinal magnetic recording and perpendicular magnetic recording is being explored. But all these solutions come with their own set of drawbacks.

Use of solid state drives is another solution, which gives very high areal density and are faster than conventional magnetic hard

drives and have no moving parts. But this devices are incapable to recover old data and have a high price tag.

Another technique to advance the field of memory device is the use of spintronics, where electron spin carries the information in addition to the electron charge in normal HDD devices. Addition of spin degree of freedom to the normal semiconductor devices churns out many advantages, such as, non-volatility, higher processing speed and increased integration densities. In current days devices utilizing the spin polarized current are available in market, for example we can name spin-transfer-torque magnetic RAM (STT-MRAM), where the data is stored in the magnetic state of nano-magnet, but the data is read and written electronically. This devices have low access speed of only 10nS and have high endurance due to absence of any moving parts.

Spintronic devices utilize the electron magnetic moment arising due to their spin. Since in these devices, spin is the quantum of charge carriers, polarization of the spin current and spin scattering are the factors that can improve the efficiency of the device.

Spin current and its effects Most of spintronic devices available today are memory devices that use the electron spin to store data and works in spin current. When current with oppositely polarized electrons moves in opposite direction, through same conductor, spin current is generated. In this way there is only the electronic spin moves through the cross section of the conductor. The current has a some very striking differences from normal electric current. First of all, since there is no net particle transfer, resistivity of the system is suppressed. Spin current is invariant under time reversal, i.e if the time move backwards, still the spin current will flow in the same direction. Most importantly, spin current is associated with spin angular momentum flow, which allows quantum information to be sent to a device via spin current.

1.2 Half metallic ferromagnet

Generating ideal spin current is very difficult, and needs new type of materials that have a completely spin polarized electronic band structure. For this purpose, de Groot in 1983 defined a fully spin polarized system as half metallic ferromagnet (HMF) [16]. These HMFs are unique class of materials having two distinct band structure for two spin bands: the majority spin band has metallic character whereas the minority spin band is a semiconductor with an electronic band gap at the Fermi level (E_F). Band structure of HMF system is shown in figure 1.1. For more clarity, density of States (DOS) structure of a HMF, Fe_2TiSb is shown in figure 1.2. Due to the unique electronic structure HMFs exhibit 100% spin polarization at E_F . Thus, such materials are ideal candidates for spin injection in non-magnetic materials.

For a successful device application, an HMF system needs to follow two basic criteria. Firstly, high Curie temperature over room temperature and second a good interface quality. In general application, HMF materials are used in layer with semiconductor materials for better spin injection efficiency, so the materials are also preferred to have a good conductance matching with the substrate [77].

Mainly, four type of materials have been theoretically and experimentally estimated to be HMF: Zinc Blend compounds (CrAs [5]), Perovskites (LaMnO_3 [60]), Intermetallic Heusler alloys (Mn_2CoAl [61]) and Oxide compounds (CrO_2 [8]). Among them, LaMnO_3 perovskites have a high spin polarization of 78% at low temperature, but at RT it almost becomes zero, although T_c of the system is higher than RT. Because of this issue perovskites are not suitable for device application. CrO_2 and CrAs, both systems have Curie temperature higher than room temperature, but the band gap present in the minority spin band decreases at non zero temperature [5, 6, 37, 46]. On the other hand, few Heusler alloys like

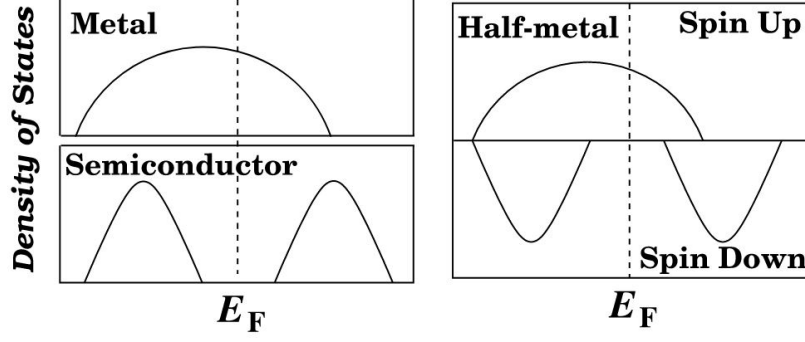


Figure 1.1: Schematic diagram of electronic states near Fermi level for metal, semiconductor and half metallic systems.

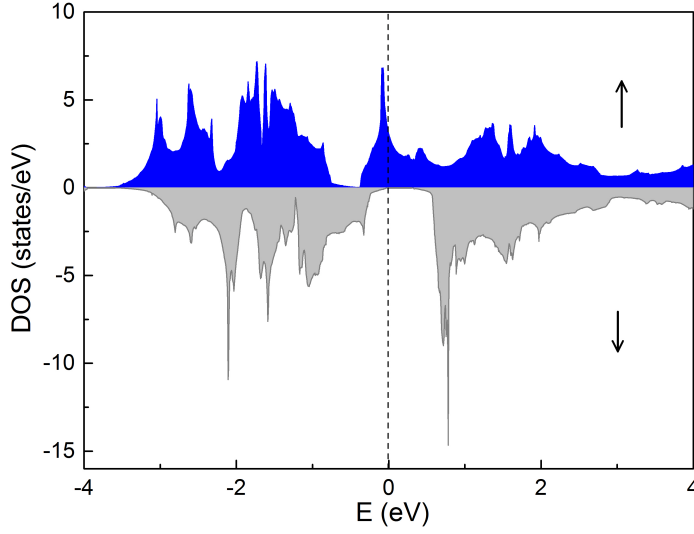


Figure 1.2: Density of states for Fe_2TiSb , an HMF system.

NiMnSb [16], Co_2FeSi [48, 96] etc have demonstrated very high spin polarization with Curie temperature as high as 1100K. Heusler alloys have been selected for the study in this thesis work, so this compound will be discussed in details in the next section.

1.3 Heusler alloy

After the discovery in 1903 by Fritz Heusler, Heusler alloy gained immense interest due to its multifunctional properties. The first studied Heusler compound was Cu_2MnAl , which cultivated so much interest because of the ferromagnetism observed in this compound, despite of its three non-magnetic constituent elements. On a side

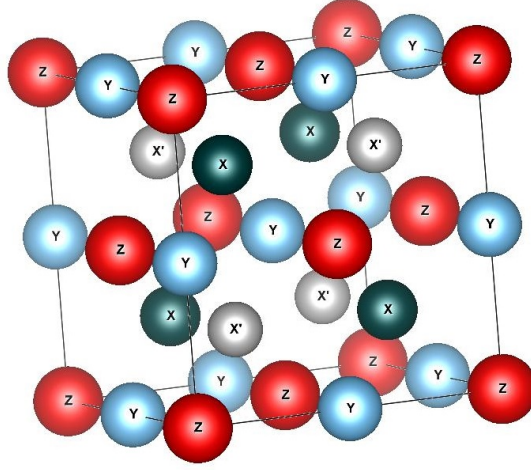






Figure 1.3: Cubic struture of a Heusler system.

note, Mn was identified as antiferromagnet much later, in 1940, after the work by Néel. After the initial discovery, Heusler alloys have been in focus of research work due to its interesting yet simple multifunctional properties. Upto now Heusler family has grown to accomodate over 2200 compositions exhibiting a wide range of physical properties such as, spin-gapless semiconductivity, high-temperature ferri and ferro-magnetism, thermoelectrics, shape-memory compounds, Weyl or Dirac semimetals, Kondo insulator and tunable topological insulators [22]. This properties have huge potential applications in spintronics, energy and sensor technologies.

Full-Heusler compounds have the general chemical formula - X_2YZ , where X and Y are 3d transitional metal and Z is a main group element. This compounds crystallize in $L2_1$ structure with $Fm\bar{3}m$ space group, formed by 4 inter-penetrating FCC sub-lattice, 2 of which are occupied by X atoms and the remaining two by Y and Z atoms. The corresponding *wycoff* positions are given by 4a (0, 0, 0), 8b ($\frac{1}{4}$, $\frac{1}{4}$, $\frac{1}{4}$) and 4c ($\frac{1}{2}$, $\frac{1}{2}$, $\frac{1}{2}$). Structure of a cubic Heusler alloys is shown in figure 1.3. In the unit cell the most electro-positive and electronegative elements, Y and Z atoms, forms a NaCl type structure, because of their ionic-like character. Whereas the X atoms occupy tetrahedral positions and makes covalent bonding with the Y atoms.

Depending on the stoichiometry and character of the constituting elements, few other variants of Heusler alloys are also present. Heusler alloys with stoichiometry XYZ are called half-Heusler, one of the 2 FCC sublattices for X atom remains vacant in this case. Half-Heusler systems crystallizes in $C1_b$ structure($F\bar{4}3m$ space group). On the other hand if in a full Heusler system, X is more electropositive than Y, then X and Z makes the ionic bonding and remaining X and Y atoms occupies the tetrahedral positions. Such systems are called inverse Heusler systems. Further, Heusler alloys with $XX'YZ$ stoichiometry are called quaternary Heusler alloys. Table 1.1 shows the atomic arrangements for different type of Heusler structures.

Table 1.1: Different Heusler alloys with their respective atomic arrangement.

Heusler alloy	Chemical composition				
Full Heusler	X_2YZ	X	X	Y	Z
Half Heusler	XYZ	X		Y	Z
Inverse Heusler	X_2YZ	X	Y	X	Z
Quaternary Heusler	$XX'YZ$	X	X'	Y	Z

Chemical Disorder in Heusler compounds Perfectly ordered crystals, with all constituent atoms at their intended positions are rare in nature. Almost all naturally occurring compositions or those synthesized in a laboratory, does show some small amount of atomic disorder. According to the origin this disorder can be extrinsic, if the reason is due to impurity or intrinsic, if the origin is only thermally activated. Intrinsic disorder can be further classified in three categories as follows,

1. **Frenkel Disorder**, when an atom is displaced from its natural lattice site to an interstitial site.
2. **Schottky Disorder**, when vacancy is created in a lattice in stoichiometric ratio

3. **Antisite Disorder**, when atoms of different species exchange their lattice position.

While the first two type of disorders are common in binary alloys, the antisite disorder normally occurs in ternary or more complex alloys and oxides. Thus in full heusler alloys with chemical composition X_2YZ , antisite disorder is the dominant type of disorder. There exists many examples in condensed matter physics where such partial swiipe amongst atoms, results in fascinating properties. Near-room temperature colossal magnetodielectricity in $\text{La}_2\text{NiMnO}_6$ [15], introduction of localized states at Fermi level giving rise to hopping conduction in $\text{Cu}_2\text{ZnSnS}_4$ [97], preamorphization swelling in $\text{Lu}_2\text{Ti}_2\text{O}_7$ [42], are some of the examples where disorder has played a vital role. In Heusler alloys too, the physical properties are sensitive to the atomic arrangement in the X_2YZ composition [22], and an anti-site disorder is often seen to create undesirable effects like decrease in the spin polarization of half metallic systems [70], or dilute magnetism in a non-magnetic background [43].

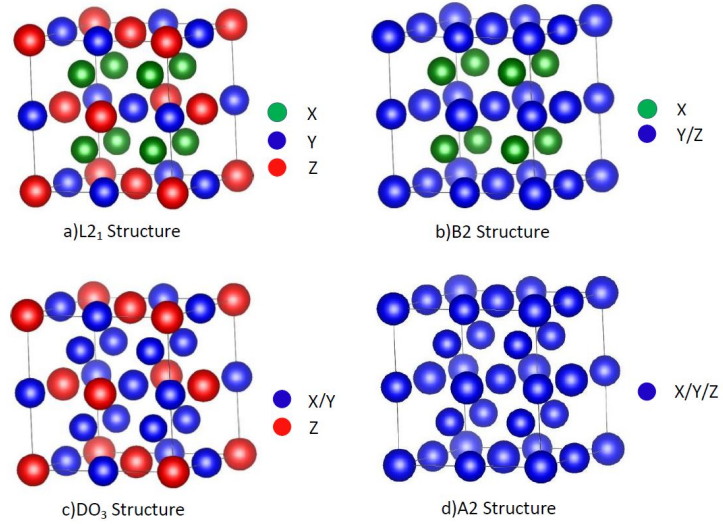


Figure 1.4: Illustration of atom exchange of different types of chemical disordering in the unit cell.

In full Heusler alloys each Y or Z atoms find 8 X atoms as its nearest neighbour in octahedral symmetry position, whereas each X

atom has 4 Y and 4 Z atoms at its nearest neighbouring position in tetrahedra symmetry. Depending on different site exchange between the atoms there can be different disorder in a Heusler structure. If there is exchange between Y and Z atoms, the structure is called B2 type disordered. When there is site swapping between X atoms and Y atoms, it is called DO₃ type disorder. A2 type disorder occurs when there is a complete mixing between X, Y and Z sites. a schematic of different type of disorder is shown in figure 1.4.

In this thesis work, the disorder has been analysed using Webster approach [92]. The basics of this approach is that the disorder in these compositions can be qualitatively and quantitatively estimated from the relation between atomic ordering and superlattice diffraction lines in XRD.

In the XRD profile of a full Heusler alloy, three primary peaks can be observed with hkl values, (111), (200), (220). Without any disorder, the structure factors for these three main peaks can be given by,

$$\begin{aligned} F_{111} &= 4|f_Y - f_Z| \\ F_{200} &= 4|f_Y + f_Z - 2f_X| \\ F_{220} &= 4|f_Y + f_Z + 2f_X| \end{aligned}$$

Where f_i is the total atomic structure factor for the element i . So, by looking at the equations it can be clearly said that, in case of B₂ type disorder the (111) peak will get affected, whereas in case of A2 or DO₃ type disorder, the (200) peak intensity will get affected. The (220) peak is disorder independent, since the intensity is dependent on the sum of all atomic structure factors. So, clearly the intensity ratios of the two peaks (111) and (200) with (220) can give an estimate of the amount of disorder present in the sample.

Origin of the spin gap The origin of the electronic band gap in Full heusler systems can be explained from the hybridization model

discussed by E. Galanakis [26] for full Heusler alloys. In L2₁ struc-

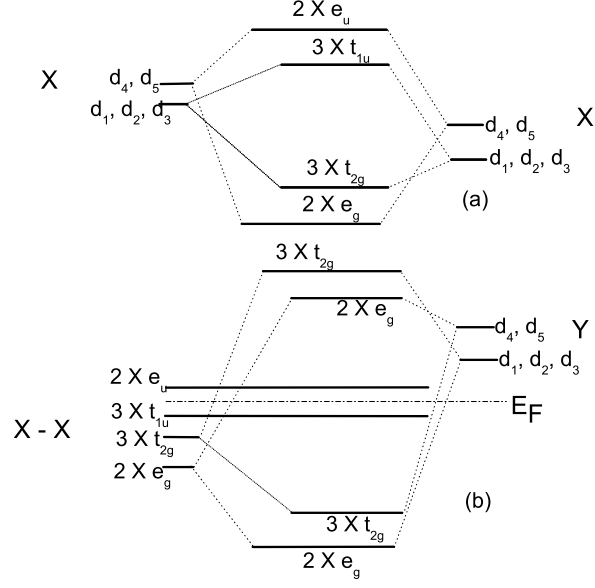


Figure 1.5: d - d hybridization scheme in Fe₂TiZ

ture the atom at the X (8c, (0.25, 0.25, 0.25)) has 4 Y and 4 Z atom as its nearest neighbor at a distance of 0.433a (a is the lattice parameter) sharing a tetrahedral symmetry position. It has another X atom as the second nearest neighbor at 0.5a distance. So, the bond length of these two type of bonds are very close and not only the interaction X(3d) and Y(3d) interaction is important, but the X(3d) – X(3d) interaction is also responsible for the electronic structure near the Fermi level.

In order to explain the *d*- electron behavior in the system, all possible hybridizations are shown in the Figure 1.5. The d_{1,2,...,5} represents the d_{xy}, d_{yz}, d_{zx}, d_{3z²-r²} and d_{x²-y²} orbitals respectively. At first the neighboring X atoms *d* orbits hybridization are shown in figure 1.5(a). The d₄ and d₅ orbitals form 2 bonding e_g states and 2 anti-bonding e_u states. The coefficients in figure 1.5 represents the degeneracy of the corresponding level. Similarly the d₁, d₂ and d₃ orbitals also hybridize, creating triply degenerate bonding t_{2g} and anti-bonding t_{1u} orbital. In figure 1.5(b) the e_g orbitals of X-X interaction (shown in figure 1.5(a)) hybridize with d₄ and d₅ orbitals

of Y and creates doubly degenerate bonding and anti bonding states. Similarly the t_{2g} orbitals also hybridize with d_1 , d_2 and d_3 states of Y atom and transforms into orbitals with same representation and degeneracy. But the anti bonding states e_u and t_{1u} , can not couple with any Y- d orbitals, and become non bonding states for Y and Z both atoms. This lack of hybridization of e_u and t_{1u} of Fe results in a band gap in both the spin bands of the samples. Among them t_{1u} states are occupied and e_u are not. So the hybridization generates a total of 8 d bands after hybridization and along with the 4 low lying s - p bands from the Z element, which can accommodate a maximum of 12 electrons at each spin band [31]. Any deviation from the 12 valance electron number in any spin band can move the E_F out of the gap and make the system half-metallic. Magnetic moment in a half-metallic full Heusler system is known to follow a simple linear law with respect to the valance electron number. This linear law is known as Slater–Pauling rule.

Slater-Pauling rule Slater [81] and Pauling [63] individually discovered that, total magnetic moment (M) of 3d transition metals and their binary compounds can be estimated from the total number of valance electron (Z_t) in the system. Depending on the Z_t value, the rule distinguishes in two regions: For $Z_t \geq 8$, it indicates itinerant magnetism and $Z_t \leq 8$ localized moment, with Fe as the borderline case. The rule dictates that in the localized moment part the magnetic moment per atom approximately takes the form, $M = Z_t - 6$. The HMF full Heusler alloys strictly follow this rule and since a full Heusler alloy have four atoms in a unit cell, the equation takes the form, $M_t = Z_t - 24$, where, M_t is the magnetic moment of a unit cell. Figure 1.6 shows total magnetic moment of some HMF full Heusler alloys plotted with their respective valance electron number.

Half-metallicity was first coined by de Groot [16] in half-

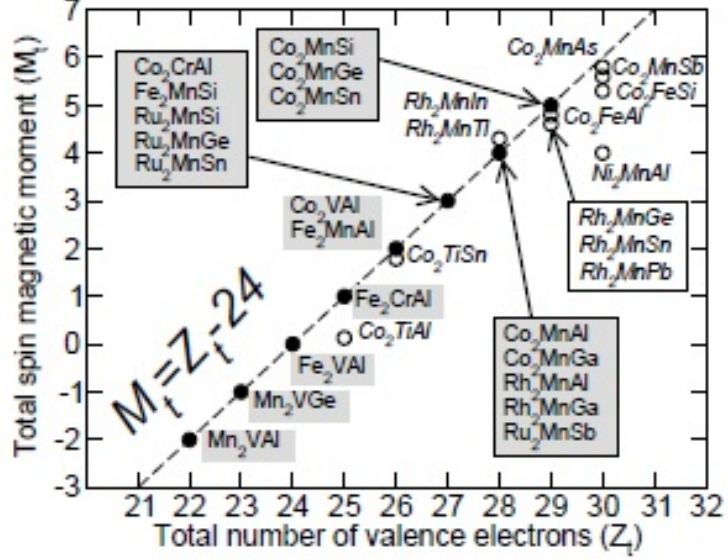


Figure 1.6: Calculated total magnetic moment for some half metallic Heusler alloys. The dotted line represents the Slater–Pauling line [26].

Heusler NiMnSb. First nanoscale thin film was fabricated from Co_2MnSi for spintronic device application by Geiersbach *et al* [27] and Raphael *et al* [71]. Till now most of the research in this context has been focused on Co and Mn based full Heusler systems, mainly due to their comparatively high Curie temperatureS [9, 61]. Fe-based full Heusler alloys also show very interesting and significant structural, electronic and magnetic properties. These compositions also show high Curie temperature and half-metallicity at room temperature [69, 95]. Further, a recent theoretical study on Fe-based full Heusler systems by Bilc *et al* [12] have shown huge potential of these systems to be used for thermo-power generation. However, the issue with Fe based full-Heusler system is, most of them are metastable at room temperature.

1.3.1 Fe_2TiSn : An interesting Full-Heusler alloy

Fe_2TiSn is a full-Heusler composition that is classified as a non-magnetic semi-metal with a pseudo-gap of 0.07eV at Fermi level [93].

This composition shows very unusual characteristics, the reason for which is due to its almost flat bands at E_F . Based on the specific heat measurement Fe_2TiSn was speculated to be a heavy fermionic metal with an effective mass of almost 40 times the free electron mass [83], and its unusual electrical transport beared a resemblance to Kondo insulator [84]. Later infrared and optical spectroscopy measurement suggested that the low-temperature upturn in resistivity was due to Schottky anomaly arising from magnetic clusters formation [19].

This system has 24 valance electrons and thus the Fermi level stays inside the gap between t_{1u} and e_u states, giving rise to the small pseudo-gap at E_F . A small change in the valance electron number in one spin band can shift the E_F outside the gap creating a half metallic ground state in the system.

Experimentally, it was also found that there is a high probability of anti-site disorder between Fe and Ti in the system [82]. This antisite disorder affects the ground state properties of Fe_2TiSn , resulting in a weak ferromagnetic state at low temperature [83], further affecting its prospects of exhibiting a half metallic ground state.

1.4 Aim of the research work

The objective of this thesis work is to generate half metallicity in Fe_2TiSn with simultaneously decreasing the anti-site disorder. For this we adopted a two-pronged strategy: To decrease the disorder, a small amount of Ti was substituted at Fe site, which can decrease the Fe concentration in the system thereby decreasing the probability of Fe going to Ti site. In second approach higher electronegative element like Sb, Ge, Si was substituted at Sn site. In a full Heusler system, Ti and Sn make a rock-salt(NaCl)structure by ionic-like bonding, so substitution of higher electronegative elements at Sn

site strengthen the Ti–Sn bonding and prevents Fe to Ti site. Since Sb has one electron more than Sn, it can successfully shift the Fermi level out of the small pseudo gap. Following similar procedure Cr was substituted at Ti site, as Cr has two electrons more than Ti, thus generating half-metallicity in this system.

Hence, $\text{Fe}_{2-x}\text{Ti}_{1+x}\text{Sn}$ (with $0 \leq x \leq 0.1$), $\text{Fe}_2\text{TiSn}_{1-x}\text{Sb}_x$ (with $0 \leq x \leq 0.6$), $\text{Fe}_2\text{TiSn}_{0.95}\text{M}_{0.5}$ (with $\text{M} = \text{Si, Ge}$) and $\text{Fe}_2\text{Ti}_{1-x}\text{Cr}_x\text{Sn}$ (with $0 \leq x \leq 0.25$) series were prepared by arc -melting technique and analyzed by different structural, electronic and magnetometry measurements. The results of such study are compiled in the form of various chapters discussed in this thesis.

Chapter 2

Experimental techniques and computational details

2.1 Preamble

This chapter aims to discuss the principles of various experimental and theoretical techniques employed in the thesis work. The first section describes the experimental techniques including the experimental tools and analysis methods. At the beginning of the section the arc melting technique and the procedure to synthesize bulk Heusler alloy is introduced. The following sections describe X-ray diffraction(XRD) measurements, energy dispersive X-ray analysis(EDAX), X-ray absorption fine structure measurement(XAFS). This measurements were employed for overall and local structural analysis of the prepared compositions. The third and fourth sections describe the instruments used for magnetometry and electrical transport measurements, respectively.

Density of states and Heisenberg exchange coupling parameters were calculated implementing density functional theory in order to look into the electronic structure of the compositions. Details of the calculation method and used software are described in brief at the end of this chapter.

2.2 Experimental Techniques

2.2.1 Sample Preparation

The intermetallic compositions have been prepared using an Arc Melting furnace. The metals are melted using an electric arc formed between a Tungsten electrode and the Copper hearth on which the constituent elements are placed. . As shown in figure 2.1, an arc

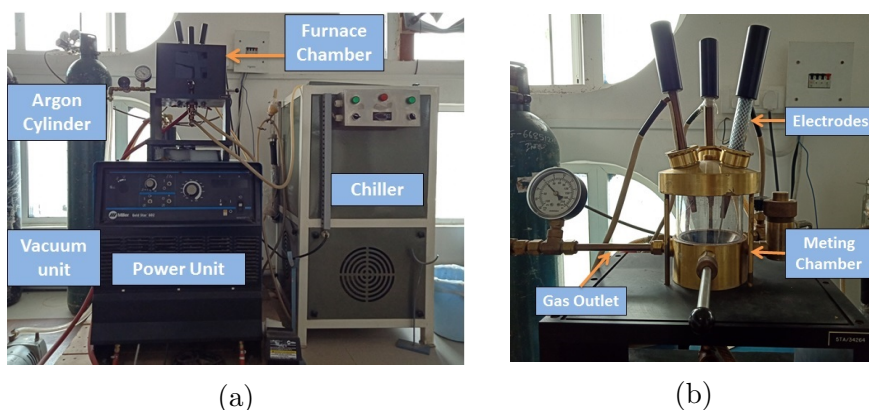


Figure 2.1: (a)Image of the Arc melting furnace used. (b) A close up view of the melting chamber.

melting furnace consists of four major parts, a furnace chamber where the melting takes place, a power source, water chiller, and a vacuum unit. The furnace chamber is attached to a water cooled Copper hearth and electrodes made of Tungsten. Other end of the electrodes are connected to a high range power source. The constituent elements according to required stoichiometry are placed on the Copper hearth and evacuated up to 10^{-4} Bar followed by purging Argon gas into the chamber with a pressure slightly above the atmospheric pressure. The evacuation and gas purging procedure is repeated 6 – 7 times to ensure a completely inert atmosphere in the arc melting chamber. Finally, the constituents elements were melted by generating an arc by momentarily striking the electrode on the Copper hearth. Both, the Copper hearth and the electrodes are attached to the chilled water circulating unit.

The metallic beads that are obtained after melting the elements, are sealed in quartz ampoule under high vacuum(10^{-6} bar) and was heat-treated for 72 hours at 800° C followed by quenching in ice-cold water. Figure 2.2 shows a typical sealed quartz ampoule with a sample bead inside. The sample bead was cut into different size and shape using low-speed diamond saw, to be used in different characterization techniques.

A part of the sample bead was grounded to fine powder using Agate Morter and pastel and was passed through a 0.09mm sieve. This finely grounded powder was used for structural studies using X-ray diffraction (XRD) and Extended X-ray absorption fine structure (EXAFS) studies, whereas the remaining pieces were used for different transport, magnetic, magneto-transport studies. The basic principle used for all the measurements are described in the following sections.



Figure 2.2: A quartz ampoule with a sample bead inside. A measuring scale is placed to indicate the size of the ampoule.

2.2.2 Powder X-Ray Diffraction

X-Ray diffraction is one of the basic tools to analyze the crystal structure, internal stress, atomic order, occupancy of a system and so forth. In this technique, monochromatic beam of X-ray is made incident on finely powdered sample. If the wavelength of the X-ray

beam is comparable to the distance between two planes of the crystal, the rays get scattered elastically from the atomic electrons. The scattered waves interfere constructively in some particular directions determined by the well known Bragg's law given by,

$$2d \sin \theta = n\lambda \quad (2.1)$$

where, d is the inter-planar distance, θ is the angle of diffraction, n is the order of diffraction and λ is the wavelength of X-ray. The obtained XRD pattern is a plot of diffracted X ray intensity against the specific Bragg angles. In case of powder XRD each particle of the powder works as a tiny crystal oriented randomly with respect to the incident beam. Thus Bragg's law is satisfied for all lattice planes, and Bragg's reflection is achieved for all planes with high relative intensity.

The XRD patterns for $\text{Fe}_2\text{TiSn}_{1-x}\text{Sb}_x$ and $\text{Fe}_{2-x}\text{Ti}_{1+x}\text{Sn}$ compositions was carried out using a commercial lab based RIGAKU make Smartlab X ray diffractometer system with $\text{Cu } k_\alpha$ source ($\lambda = 1.544\text{\AA}$) XRD patterns for some samples were also recorded using the rotating anode, $\text{Mo } k_\alpha$ source ($\lambda = 0.72\text{ \AA}$).

Measurements were also carried out using synchrotron-based source at RRCAT, India and Photon Factory, KEK, Japan. In particular, the XRD for $\text{Fe}_2\text{TiSn}_{1-x}\text{M}_x$ ($\text{M}=\text{Si, Ge}$) and $\text{Fe}_2\text{Ti}_{1-x}\text{Cr}_x\text{Sn}$ compositions were recorded in "Extreme Conditions Angle Dispersive/Energy dispersive x-ray diffraction (EC-AD/ED-XRD) beamline (BL-11) at Indus-2 synchrotron source, Raja Ramanna Centre for Advanced Technology (RRCAT), Indore, India. Measurements were carried out in capillary mode and the capillary was rotated at 150 rpm to reduce any orientation effects. Desired wave length for XRD experiments was selected from a bending magnet using a $\text{Si}(111)$ channel cut monochromator.

To determine the amount of atomic site disorder between Fe

and Ti, a unique experiment with XRD measurement was designed and carried out on $\text{Fe}_{1-x}\text{Ti}_x\text{Sn}$ compositions using synchrotron source at the Indian Beamline (BL18B), KEK, Photon Factory, Japan. In this technique, the anomalous dispersion of X-ray beam diffracted from the particular sample is recorded, when the incident beams wavelength is tuned to the absorption edge of a constituent atoms. At absorption edge scattering factor of the probed atom changes drastically, which helps to identify the presence of the atom at a particular site. Details of the experiment is in chapter 3.3. The measurement was done using a four-circle goniometer and Fe K absorption edge was probed.

All the diffraction patterns were analysed using Rietveld refinement techniques, as implemented in FullProf package [75]. This method of data analysis was proposed by Hugo Rietveld [74], and till date it is one of the most powerful tools to analyze XRD and neutron diffraction pattern. In this technique, a diffraction profile is simulated from the initial crystal structure information like space group, Wyckoff positions of constituent atoms etc and the experimental data is matched using a least squared fitting method. The fitting involves both crystal and instrumental parameters. The goodness of the fit is indicated by χ^2 and R_{Bragg} . The fitting parameters are varied till χ^2 value reaches unity and R_{Bragg} value tends to zero.

2.2.3 Energy Dispersive X-ray Spectroscopy

Energy Dispersive X-ray Spectroscopy(EDX) is used to determine the elemental ratios present in a prepared composition. Such measurement helps confirm the formation of intended composition of the prepared samples. In this method, the sample is bombarded by a beam of electron from an electron gun. For sufficiently high energy, the bombarded electron can knock-off core level electrons from the

system. The vacancy in the inner shell is filled by outer level electrons, giving rise to emission spectrum. This emission spectrum is characteristic of particular atoms and analysis of this spectra provides information about the concentration of the elements present in the system. In our thesis work Carl Zeiss, Model–Supra 55 field-emission scanning electron microscope equipped with an Oxford instruments AZtec energy dispersive microanalysis system, was used.

2.2.4 X–ray Absorption Fine Structure

This experimental technique was used to study the local crystal structure of the prepared compositions. X-ray absorption fine structure(XAFS) is basically the modulation of absorption probability of an atom, at or near the core level (K shell) binding energy of the atom in the given chemical environment. This technique is very sensitive to the oxidation state, chemical co-ordination, properties of chemical bonding with the surrounding atoms of the absorbing atom. Due to this characteristic the experiment is a simple, practical and reliable way to determine the local atomic structure surrounding the probing atom, and regularly used in biology, environmental and material research. Most importantly, this measurement can be carried out on highly disordered and liquid materials.

An XAFS spectrum can be divided into two regions, as demonstrated in figure 2.3.:

1. The near absorption edge region, called X – ray absorption near edge structure or XANES which extends ~ 150 eV from the main absorption edge.
2. The extended region after the main absorption edge(can stretch upto ~ 200 eV), referred to as extended absorption fine structure or EXAFS

XANES spectra mostly includes the electron transition into bound or quasi bound states, and multiple scattering from all the neighbouring atoms contribute here. So XANES is a reliable probe for local chemical environment which includes, oxidation state, unoccupied DOS etc. Whereas EXAFS spectra is mostly consists of single scattering from nearest neighbour atoms, which makes it a better local probe for bond length or bond angle.

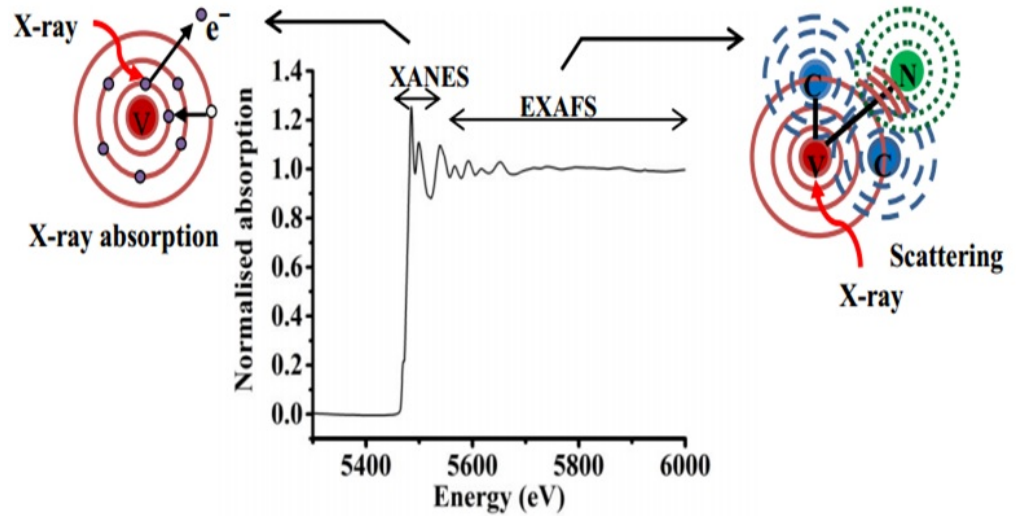


Figure 2.3: The X-ray absorption mechanism showing the absorption and scattering of X-ray wave from atom. [85].

Basically in this experiment a core level electron is emitted by absorbing a high energy X-ray photon if the photon energy exceeds its binding energy. This results in a sharp drop in the transmitted energy, which is called the absorption edge. The outgoing photon works as a spherical wave expanding in all direction, as shown schematically in figure 2.3. This waves partially back-scatters from the neighbouring atoms. When the back-scattered wave interferes with another outgoing wave, it give rise to constructive or destructive interference. The interference pattern thus generated primarily depends on distance, number and nature of the neighbouring atoms.

Considering different factors controlling the EXAFS spectra,

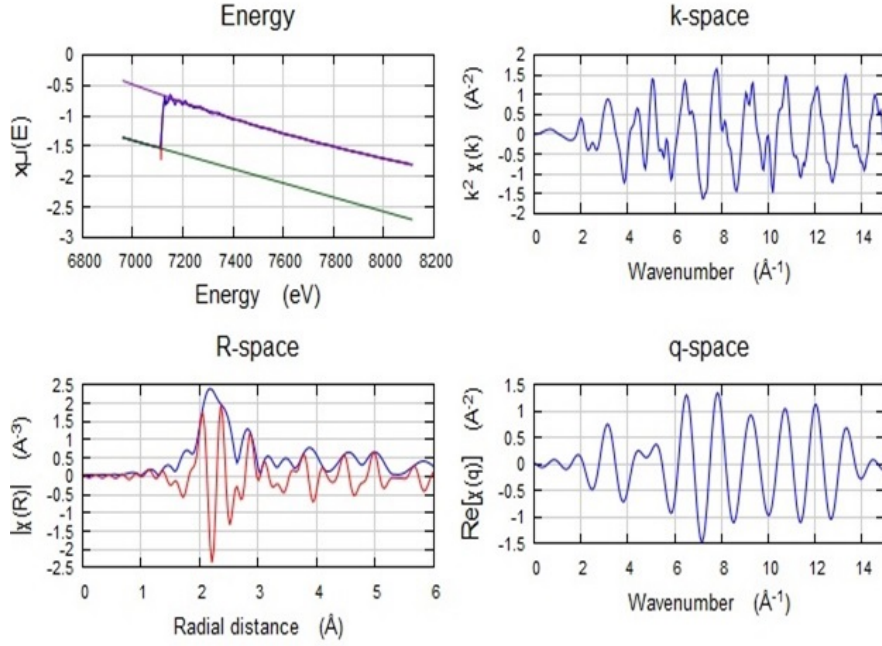


Figure 2.4: A typical XAFS data for Fe_2TiSn is shown. (a) First the raw data is background subtracted and normalized. (b) Transformed into k space and scaled by k^2 to magnify the subtle features. (c) Fourier transformation into R space (d) Inverse Fourier transformed into $k(q)$ space again.

the X ray absorption function, $\chi(k)$ can be expressed as [14],

$$\chi(k) = \sum_i \frac{N_i S_0^2 e^{-2k^2 \sigma_i^2} e^{\frac{-2R_i}{\lambda(k)}} f_i(k)}{k R_i^2} \sin[2k R_i + \delta_i(k)] \quad (2.2)$$

Here, N is the coordination number of the probing atom, σ_i^2 thermal mean square displacement or the Debye–Waller factor of the bond distance given by R_i , λ is the mean free path of the photoelectrons, and the subscript, i , represents the individual coordination shells of identical atoms at approximately same distance from the absorbing atom. From the above equation following very important conclusions can be drawn,

1. Because of the presence of R_i term the EXAFS signal intensity falls off very quickly and is generally not able to see much further than $\sim 5\text{\AA}$.
2. The EXAFS signal consists of signals of different frequencies

from each individual coordination shell. Thus to separate out contribution from each shell, Fourier transform is used.

To conduct the measurement, samples are made into absorbers with special care taken to maintain the homogeneity and thickness of the absorbers, and to avoid any pinhole. The thickness of the absorbers is adjusted until a good signal to noise ratio is obtained, such that $\Delta\mu_x \leq 1$. The data can be recorded in fluorescence as well as transmission mode. The recorded XAFS spectra is basically, a variation of absorption co-efficient ($\mu(E)$) as a function of the incident energy. XAFS function $\chi(E)$ is then calculated from the $\mu(E)$ profile as,

$$\chi(E) = \frac{\mu(E) - \mu_o(E)}{\Delta\mu_o(E)} \quad (2.3)$$

Where $\mu_o(E)$ is the background function and $\Delta\mu_o(E)$ is the absorption jump determined from the difference between background and absorption co-efficient at the absorption edge. Since XAFS is basically the interference pattern between scattered waves of photoelectron it is commonly converted to a function of wave number k using the following formula,

$$k = \sqrt{\frac{2m_e(E - E_o)}{\hbar^2}} \quad (2.4)$$

For analysis, the data is then Fourier transformed into real space to separate out the contribution from different scatterers. The data is background subtracted and normalized before converting into momentum (k) space. Data analysis is carried out by using the available software (ex. ARTEMIS) that incorporates the theoretical simulation done using the FEFF code [72, 73]. The experimental spectra remodeled as a sum of contribution from different scattering paths and made to fit to a model structure, the basis for which is the information obtained from the XRD analysis of the absorbing

species. Several iterations of the model are carried out by refining the variable parameters until a satisfactory fit of the model to the experimental spectrum, is obtained.

All the measurements presented in this thesis have been measured, probing Fe k absorption edge($E = 7110$ eV) and in transmission mode.

For the measurement of $\text{Fe}_2\text{TiSn}_{1-x}\text{Sb}_x$ series of compositions, a Rigaku R-XAS made spectrometer was used. The instrument is equipped with a 3kW X ray source and Ge(311) monochromator. The incident and transmitted beam intensity was measured using gas filled ionization chamber and scintillation detector respectively.

XAFS spectra for rest of the compositions were taken using high intensity synchrotron based source at BL65 of PETRA III, DESY, Germany in transmission mode. Ionization chamber filled with 80% N_2 and 20% Ne_2 was used as X – Ray detector. Each measurement was repeated multiple times in order to acquire good signal to noise ratio. For each measurement a standard(pure Fe film) spectra was taken to adjust the absorption edge.

2.2.5 Magnetic property measurements

Investigation of the magnetic properties of all the prepared compositions has been a major part of the thesis work. All the experiments were performed using the Quantum Design inc. Inc. Magnetic Properties Measurement System (MPMS) SQUID–VSM and physical property measurement system(PPMS)–Vibrating Sample Magnetometer (VSM).

The central part of an MPMS is superconducting quantum interference device(SQUID), an extremely sensitive flux to voltage converter. A SQUID is basically two parallel Josephson junction connected in a loop. A Josephson junction is made by sandwich-

ing an insulating layer between two superconducting layers. A schematic of Josephson junction is shown in figure 2.5a. The electrical current density through this device depends solely on the phase difference, $\Delta\phi$ of the two superconducting wave functions at two ends. Also the time derivative of $\Delta\phi$ is correlated with the voltage that appears across the insulating layer. The $\Delta\phi$ gets affected by magnetic flux through the ring. This way it can work as a flux to voltage converter and capable to resolve 10^{-15} T of magnetic field.

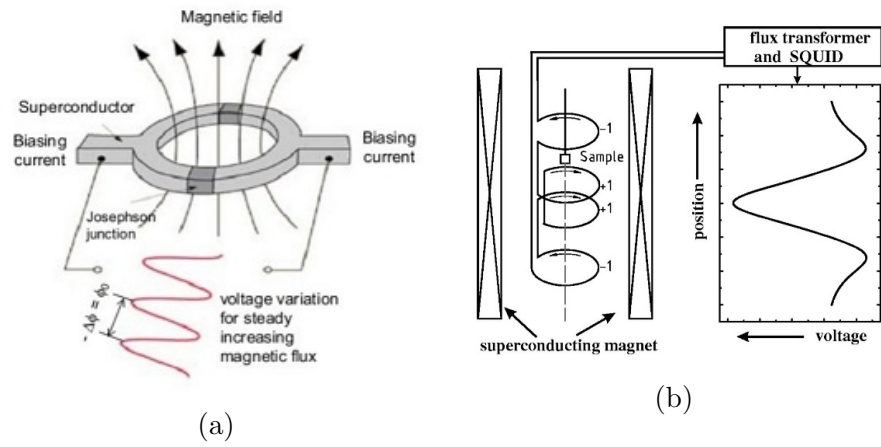


Figure 2.5: (a) Schematics of SQUID device demonstrating the working principle. [1] and (b) showing the working of the magnetometer. [10].

A schematic of the MPMS system is shown in figure 2.5b. The magnetometer device is two superconducting loops, made of Josephson junction in the current path of the loop. During operation a sample is moved up and down, through the superconducting coils. The flux lines from the samples intersect the coils and the magnetic signal is then transferred to the SQUID, which acts as a flux to voltage converter. The measured voltage is then amplified and converted by magnetometers electronics.

The MPMS does not have the option for measurement of ac susceptibility of the sample under investigation. For this, and various other transport and magneto-transport properties were measured using a Quantum design made Physical property measurement

system or PPMS. PPMS is a versatile low temperature magnet system, designed for measuring various physical properties like, ac and dc magnetic susceptibility, specific heat, both electrical and thermal transport properties(ac and dc resistivity, Seebeck co-efficient) and so forth. The instrument consists of a Helium dewar with superconducting magnet and an universal 12 pin platform, which can be used to mount samples for various different measurements.

Ac susceptibility measurement The VSM mode of PPMS is used to measure the ac susceptibility. The sample was weighed(normally 20 mg – 50 mg) before putting in the PPMS system. The sample is placed between the superconducting magnets and in a uniform magnetic field region, which induces a magnetic moment in the sample. During a measurement the sample vibrates in a sinusoidal motion, which further induces sinusoidal signal in appropriately placed pick-up coils. The voltage induced in the pick-up coil is amplified and measured using lock-in amplifier in the VSM detection module.

2.2.6 Transport properties measurement

Analysis of electronic and magnetic transport property has been another major part of the thesis work. Transport properties have been measured by recording the resistivity, heat capacity, Hall effect and Seebeck coefficient, as a function of temperature and magnetic field. Seebeck co-efficient was also measured using a home-built thermopower measurement system(Details are discussed in chapter [8.3](#)).

Resistivity measurement

Resistivity of the compositions were measured using standard four probe measurement technique. A schematic of the technique is

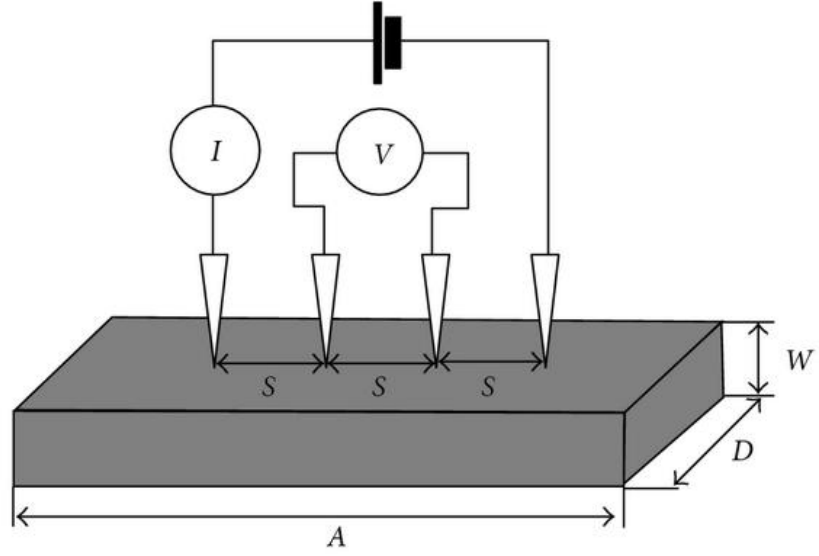


Figure 2.6: (a) Schematic diagram of a four probe resistivity measurement system. [2].

shown in figure 2.6. Outer two probe are used for current injection whereas the inner probes are for voltage measurement. The technique is used for accurate measure of very small resistance as the voltmeter ideally has infinite resistance and thus very less current flows through the voltage probes.

The sample is mounted on the PPMS puck and electrical contacts are made using Indium solder along the length of the sample. The same arrangement was used for magnetoresistance and Hall-effect measurement as well. Here, magnetic field was applied perpendicular to the sample plane.

Heat capacity measurement

Heat capacity measurement was carried out on $\text{Fe}_{2-x}\text{Ti}_{1+x}\text{Sn}$ and $\text{Fe}_2\text{Ti}_{1-x}\text{Cr}_x\text{Sn}$ series of compositions, to probe the spin fluctuation and formation of magnetic clusters. The data was measured in a temperature range 2K – 300K using the heat capacity module of PPMS, that employs the thermal relaxation method to derive the heat capacity of the sample. . Schematic diagram of the same is

shown in figure 2.7.

To thermally isolate the sample platform from rest of the system, it is suspended by thin wires. A pulsed current is passed through the wires to increase the temperature of the sample from an initial temperature T_o to T_f . The time taken by the system to reach T_f and finally going back to T_o is measured, and from the fitting of time dependence of sample temperature the heat capacity can be calculated at the particular temperature T_o .

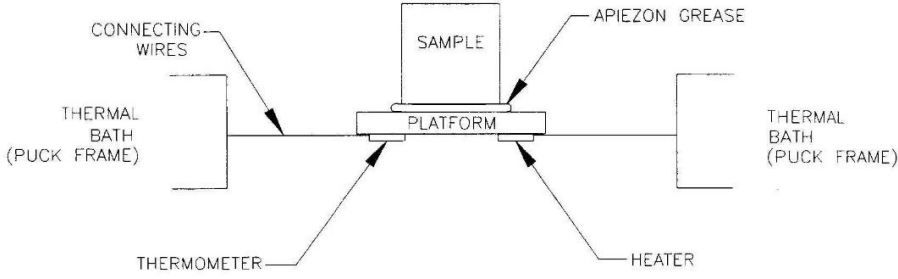


Figure 2.7: Schematic diagram of the heat capacity measurement technique. [3]

Seebeck coefficient measurement

Seebeck co-efficient of the $\text{Fe}_{1-x}\text{Ti}_{1+x}\text{Sn}$ composition was measured using a lab based system (details in the chapter 8.3). The sample was mounted between two heaters bobbins and electrical contacts with thermal isolation are made with the sample. In a typical measurement, a temperature gradient of $\sim 2\text{K}$ is generated between the heaters and Seebeck voltage generated between the two ends of the sample is measured using a fast detection electronics of Keithley 2000 digital multimeter. Temperature gradient versus Seebeck voltage gradient graph follows a linear equation, the slope of which gives the Seebeck co-efficient at a particular system temperature.

2.3 Theoretical Techniques

2.3.1 Density Functional Theory

Since the introduction of density functional theory (DFT) in 1970's, it has been used extensively to study the electronic properties of solid, molecules and atoms. It is more accurate and computationally cost effective than any other more elaborate methods under that falls under many body theorem. The formalism is based on Hohenbubrg–Kohn theorem, which states that, ground state energy of a system can be expressed as a functional of ground state single particle electron density. Since, the theorem does not provide the form of the functional, a number of different approximation techniques have been made. Using DFT the total energy of an interacting system can be written as,

$$E[n] = T[N] + \int V(r)n(r)d^3r + \frac{1}{2} \int \frac{n(r)n(r')}{r-r'}d^3rd^3r' + E_{xc}[n(r)] \quad (2.5)$$

$n(r)$ is the electron density, given by, $\sum_i |\phi_i(r)|^2$. Here i represents the single particle states and the sum is all over the occupied states. $T[N]$ represents the kinetic energy of the non-interacting electronic system, which can be written as,

$$T[N] = -\frac{1}{2} \sum_i \int \phi_i \nabla^2 \phi_i^* d^3r \quad (2.6)$$

$V(r)$ is the electron–ion potential energy. The third term represent the Coulomb repulsion energy and the last term is the exchange correlation potential energy to take care the interaction between electrons. The exact form of E_{xc} is unknown and needs to be approximate.

The most popular approach to solve the equation is by Kohn

– Sham. According their theorem the equation 2.5 simplifies to,

$$[-\frac{1}{2}\nabla^2 + V(r) + V_H(r) + V_{xc}(r)]\phi_i(r) = \epsilon_i\phi_i(r) \quad (2.7)$$

Where $\phi_i(r)$ is the wavefunction for a single electron. And $V_H(r)$ is the Hartree potential, given by,

$$V_H(r) = \frac{1}{2} \int \frac{n(r')}{|r - r'|} d^3r' \quad (2.8)$$

$V_{xc}(r)$ is the exchange correlation potential, given by,

$$V_{xc} = \frac{\delta E_{xc}[n(r)]}{\delta n(r)} \quad (2.9)$$

Here the interacting electrons are simplified into non-interacting electrons moving in an effective potential, and the $\phi_i(r)$ is the wavefunction for each individual electron. The total particle density of the N electron system is just the sum of the individual densities $|\phi_i(r)|^2$. Thus,

$$n(r) = 2 \sum_i |\phi_i(r)|^2 \quad (2.10)$$

The factor 2 comes for two spin states. The exchange term in both of the equations, can not be calculated exactly, and thus needs to be approximated. Mainly there are two types of approximation used, local density approximation(LDA) and generalized gradient approximation(GGA). The LDA method is commonly used by spin densities and was introduced by Vosko, Wilk and Nusair [90]. The second method of approximation was introduced by Perdew, Burke and Ernzerhof [64]. Here along with local spin densities, spin density gradients are also taken into consideration.

Plane wave basis and pseudopotential: To solve the Kohn–Sham equations a basis set is chosen to expand the wave–function

$\phi_i(r)$ and then truncated in order to complete the calculation in finite time. The most natural choice of basis set is plane wave in this case, simply because it can be easily expanded into Fourier series. A cut off energy is used to involve finite number of plane waves in the calculation.

Mathematically it is possible to achieve any level of accuracy by employing large number of plane waves in the calculation, but in practice it does not work for two reasons. Firstly the core electrons are tightly bound to the nuclei. So, their wave function changes rapidly and decay away in a very small region. In order to describe the wave function a large number of plane waves are required. Secondly, the core electrons are so tightly bound to the core, that they affect very little in the formation of bond. So simple use of plane wave basis set does not help much to decrease the calculation time. To solve this issue, the core electrons are treated as immobile entities stuck to nucleus and is replaced by a fixed potential. This is called frozen core approximation and the potential as pseudopotential. There are quite a few different types of pseudo-potentials that can be found in literature [33, 88].

2.3.2 Quantum Espresso

Quantum Espresso package [28] was used for calculation of band structure and DOS structure of the compositions investigated in the thesis. The DFT base package of codes are freely available to researchers around the world under the terms of the GNU General Public License. It uses pseudopotential method and plane wave basis set to solve the Kohn–Sham equation. The package utilizes different functions for various applications, such as pw.x for self-consistent calculations and atomic relaxation, pp.x for post processing of the calculated results, projwfc.x for projection of atomic orbitals *etc.*

The unit cell was built using VESTA [51] and XCRYSDEN [35]

software. The exchange correlation potential was calculated within generalised gradient approximation (GGA) using PBEsol pseudopotential [65]. To describe the Kohn-Sham orbitals, plane wave basis set was used and an energy cut off of 75 Ry was employed for all samples, to truncate the expansion of the wave functions. The charge density cut-off was set at 1000 Ry. The Brillouin zone integration was performed over a Monkhorst – Pack $8 \times 8 \times 8$ mesh and was carried out using smearing with Methfessel - Paxton spreading of 0.02 Ry. For density of states (DOS) calculation a denser mesh of $20 \times 20 \times 20$ was used with tetrahedral occupation. In all cases the calculations yield an energy convergence of 10^{-7} Ry.

2.3.3 SPR–KKR

The Munich Spin polarized Koring–Kohn–Rostokar approach was used in the thesis to calculate Heisenberg exchange coupling parameters of the compositions. The KKR method uses Green’s function method to solve the Kohn – Sham equation. Apart from the calculation of basic Self-consistent fields and DOS calculation, SPRKKR have become a very useful tool to calculate various spectroscopic properties, such as X ray magnetic circular dichroism(XMCD), X ray absorption spectra(XAS), Magnetic Compton profile etc. It is thought to provide good result in case of metallic and magnetic compositions in a shorter time. The most important feature of this code is its ability to consider atomic disorder, which is simulated with the use of the coherent potential approximation (CPA). Here effective potential of a certain site is defined by the sum of potentials from several chemical species, representing a random interchange of atoms throughout the whole system. Implementing the small disorder is complex in DFT, since it requires a supercell to deal with the disorder.

SPRKKR codes attempt to solve the similar Kohn–Sham

equation using a slightly different nomenclature. Here the starting equation is,

$$\left[\frac{\hbar^2}{2m} \nabla^2 + \beta mc^2 + V(r) \right] \phi(r) = E \phi(r) \quad (2.11)$$

The equation is almost identical to the Schrödinger equation, except the relativistic energy term, βmc^2 . The potential $V(r)$ can be written as, $V = V_n + V_H + V_{xc} + \beta \vec{\sigma} \cdot \vec{B}_{eff}$, where V_n and V_H are Coulomb potential due to nuclei and other electrons respectively. The exchange correlation part has been divided into two parts, a spin averaged part V_{xc} and a spin dependent part $\beta \vec{\sigma} \cdot \vec{B}_{eff}$. The last term represents the dependence of electron exchange correlation energy on the spin magnetization density.

Considering the Green's function, $G(r, r', E)$, the equation 2.3.3 becomes,

$$\left[\frac{\hbar^2}{2m} \nabla^2 + \beta mc^2 + V(r) - E \right] G(r, r', E) = \delta(r - r') \quad (2.12)$$

SPRKKR utilizes the muffin-tin orbital approximation, where nuclear potentials are considered to be spherically symmetric within a region called muffin-tin, around a nucleus. The radius of these muffin-tins are dependent on the atoms they represent. Generally, size of a muffin -tin is considered to be within 1 Å to 2 Å. Outside this sphere, the interstitial region is represented by a constant potential. The wavefunctions inside and outside of the muffin -tin are made of linear combinations of spherical harmonics and plane waves, respectively. Total basis set considered in this calculation are much smaller than any normal plane wave DFT calculation. Thus this method is faster than any DFT calculation.

Chapter 3

Study of anti-site disorder in Fe_2TiSn

3.1 Preamble

Fe_2TiSn is a full Heusler alloy, predicted to be a non magnetic semimetal with a pseudo gap of 0.07 eV at the Fermi level [93]. A lot of research, both theoretical and experimental has been carried out on this composition, to study its inherent anti-site disorder and unusual physical properties. However, a systematic study that directly addresses the perspective of anti-site disorder and its electronic and magnetic nature *vis-à-vis* the Fe – Ti anti-site disorder, is lacking in literature.

In this work we control the anti-site disorder in Fe_2TiSn by intentionally substituting small percentage of Ti in place of Fe atoms to yield the $\text{Fe}_{2-x}\text{Ti}_{1+x}\text{Sn}$ (with $x = 0, 0.05, 0.07, 0.1$) compounds. Using a combination of the high-resolution synchrotron radiation and laboratory Mo-target X-rays as a source for diffraction, we study the crystal structure of these compositions and unambiguously show the decrease in anti-site disorder. A thorough investigation into the electrical transport, thermal, and magnetic properties of the entire series has been carried out. Thermopower measurements reveal the *p*-type nature of charge carriers. Systematic changes in the residual resistivity and weak localization effect with changing Ti – concentration provide further evidence to the decrease in anti-site disorder.

Temperature dependence of resistivity and heat capacity provide strong evidence for spin-fluctuations being present in these compositions. Analysis of the magnetization measurements carried out as a function of applied field identify the distinctive magnetic cluster phase. Temperature and frequency dependence of ac susceptibility confirm the non-glassy nature of this low temperature magnetic state.

3.2 Results

3.2.1 Structural analysis

Room temperature XRD profiles of all the prepared compositions of $\text{Fe}_{2-x}\text{Ti}_{1+x}\text{Sn}$ series, measured using Mo target source, are shown in figure 3.1. The experimental profiles were analysed using Rietveld refinement method, implemented in the Fullprof suite [75]. The fitted profiles are shown in the same figure using solid line. Presence of strong (111) and (200) superlattice reflections clearly indicate the formation of L_{21} phase in all the compositions. Moreover, absence of any extra peak confirms the phase purity of the prepared compositions. Extracted lattice parameters from the analysis are summarized in table 3.1. Since the amount of Ti substitution in Fe site is quite small, no appreciable change in lattice parameters is seen. Although, a slight broadening of the XRD peaks are observed, which indicates that, the small difference in atomic radius of Fe and Ti gives rise to some atomic strain in the unit cell. The strain parameter in a crystal is proportional to the full width half maximum or $\text{FWHM}(\beta)$ of the peaks observed in XRD pattern and can be estimated using the Williamson-Hall relation [55], $\beta \propto 4\epsilon \tan \theta$, where ϵ represents the strain in a crystal. We extract the β values for the (220) principal reflection by fitting it with a pseudo-Voigt function and the values obtained are shown in table 3.1. Since the effect

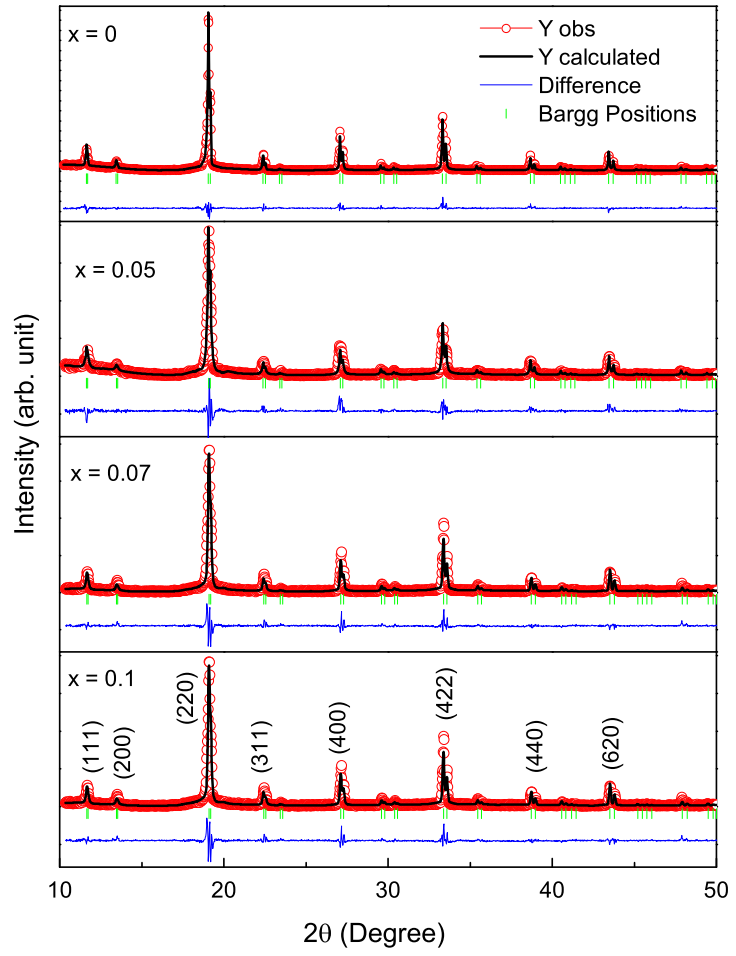


Figure 3.1: (a)XRD patterns of $\text{Fe}_{2-x}\text{Ti}_{1+x}\text{Sn}$ series recorded using Mo-target along with the Rietveld refinement fitting.

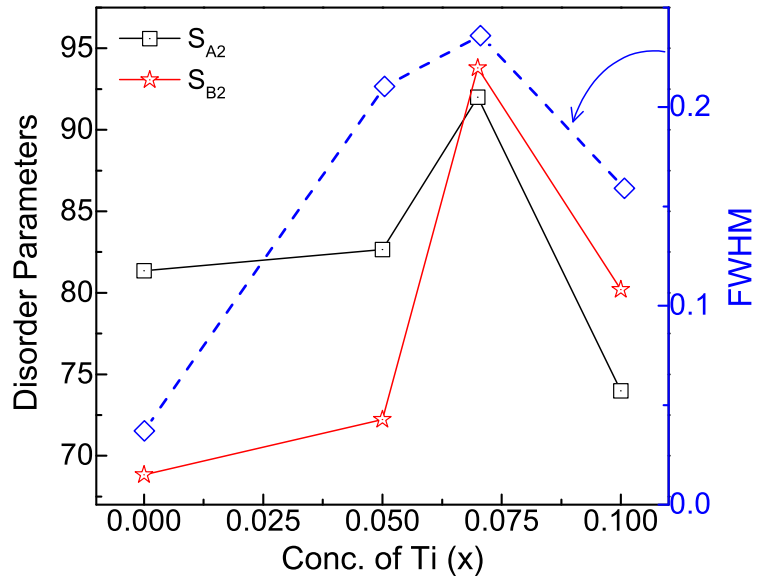


Figure 3.2: Left axis: Extent of order parameters as a function of Ti concentration. Right axis: variation in the FWHM of the XRD peaks in $\text{Fe}_{2-x}\text{Ti}_{1+x}\text{Sn}$ series

of instrumental broadening should be similar in all samples of the present set, a comparison between the values of β implies that the strain increases rapidly with increasing Ti – substitution, reaches a maximum at $x = 0.07$ and decreases thereafter for $x = 0.1$.

The major factor that needs to be addressed in these compositions is the anti-site disorder. In the X_2YZ compositions anti-site disorder between Y and Z atoms is known as B2 type disorder whereas a complete disordered structure, *i.e.* when there is disorder between all atoms in the system, it is known as A2 type disorder. In $Fe_{2-x}Ti_{1+x}Sn$ system, the rising Ti – content at the expense of Fe simply reduces the chances of Fe atoms occupying Ti – site, thus controlling the A2 – type disorder. Secondly, the rising Ti – content increases the chances of a B2 disorder. Analysis of the XRD profiles can estimate the extent of such disorder. The three primary reflections for the $L2_1$ order correspond to (111), (200), (220) planes. The structure factor(F) associated with each of these planes are related to the atomic form factor(f) of the constituting atoms by the below equations,

$$\begin{aligned} F(111) &\rightarrow |f_{Ti} - f_{Sn}| \\ F200 &\rightarrow |2f_{Fe} - (f_{Ti} + f_{Sn})| \\ F220 &\rightarrow |2f_{Fe} + f_{Ti} + f_{Sn}| \end{aligned}$$

The relations are such that, any disorder or mixing between Y and Z atoms will reduce the intensity of (111) peak, while disorder at X site due to Y or Z atoms will lessen the intensity of (200) peak. The (220) reflection is a fundamental peak where the structure factors of X, Y and Z atoms are all additive. Hence the intensity of this reflection is independent of any site-disorder. So apparently the intensity ratios of the (111) and (200) reflection with the (220) reflection can give an estimate of the amount of disorder present in the sample.

Here, (111) and (200) superlattice reflections were monitored

Table 3.1: Lattice parameters obtained from the Rietveld refinement, goodness of fit parameters (R_{Bragg} and χ^2), Order parameters for $L2_1$ order calculated from peak intensities and FWHM of the peak in the XRD pattern.

Excess Ti x	Lattice Parameter (Å)	R_{Bragg}	χ^2	S_{A2} in %	S_{B2} in %	Strain
0	6.0607(± 52)	7.02	1.81	81	69	0.037
0.05	6.0584 (± 45)	11.81	2.35	82	72	0.21
0.07	6.0505(± 31)	12.27	2.89	92	94	0.24
0.1	6.0580(± 19)	6.01	1.85	74	80	0.16

against the (220) principal reflection for all the sample compositions and the structural ordering parameters, S_{A2} and S_{B2} , were calculated using Webster approach [86, 92]. In this approach the ordering parameters are defined by the relations,

$$\frac{I_{200}}{I_{220}} = S_{A2}^2 \times \frac{I_{200}^{L2_1}}{I_{220}^{L2_1}}$$

$$\frac{I_{111}}{I_{220}} = \left[S_{B2} \left(\frac{3 - S_{A2}}{2} \right) \right]^2 \times \frac{I_{111}^{L2_1}}{I_{220}^{L2_1}}$$

where $I_{hkl}^{L2_1}$ refers to ideal peak intensities for a fully ordered $L2_1$ structure. The area-integrated intensities of the peaks obtained from the XRD pattern were used to calculate the above and extracted values are given in table 3.1. It must be noted that the table presents values for both, S_{A2} and S_{B2} , and the highly ordered composition is the one that has high value for both these parameters.

A plot of S_{A2} and S_{B2} obtained as a function of rising Ti – content is presented in figure 3.3. The ordering between Fe - Ti/Sn increases with Ti substitution, reaches a maximum for x 0.07, and decreases thereafter. Similarly, the B2 ordering increases, reaches a maximum at $x = 0.07$ and drops with $x = 0.1$. Hence, the overall disorder decreases with rising Ti substitution, with $x = 0.07$ having the least degree of anti-site disorder. It may be recollected that same trend was observed for the strain within the unit cell. Both these results indicate that the $Fe_{2-x}Ti_{1+x}Sn$ system tries to balance

between the rising strain and atomic order within the unit cell. Rising Ti concentration increases strain in the system, but also brings in atomic order and beyond $x = 0.07$, the system relieves the strain with the atoms rearranging itself and increasing the site-disorder.

Anomalous X ray diffraction study: To prove presence of Fe at Ti site we carry out anomalous X ray diffraction measurement. We monitor the intensity of (111) peak by changing the incident

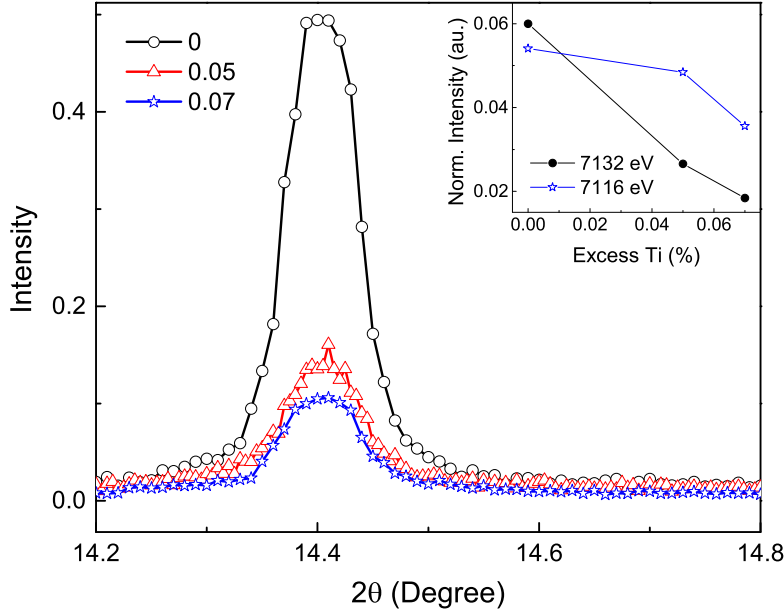


Figure 3.3: Change in intensity of the 111 peak for X ray wavelength of 7132 eV, Inset shows the normalized intensity variation for two X ray incident energies.

photon energy across the absorption edge of Fe K-edge (7112 eV). Total scattering factors of any atoms can be given by $f = f_0 + f'(\omega) + if''(\omega)$. The first term Thompson scattering factor, f_0 , which is almost proportional to the atomic number of the corresponding atom and independent of incident energy. The second and third term changes rapidly with incident energy at the absorption edge. In the ideal Heusler structure, the contribution to (111) peak intensity comes purely from the Y and Z sites (Ti and Sn in our case). Hence, any increase in the intensity of the (111) peak at the Fe absorption edge energy would confirm the presence of Fe at Ti – site.

Figure 3.3 shows the normalized intensity of (111) peak at X-ray wavelength of 7132 eV and the integrated area under the peak for different compositions, recorded at two different incident X-ray energies is shown in the inset of figure 3.3. This plot clearly shows a decrease in intensity of the (111) peak with increasing Ti concentration. As discussed previously, the change in peak intensity being the measure of the anti-site disorder between Fe and Ti atoms, the decrease seen in figure 3.3 confirms the decrease in anti-site disorder.

3.2.2 Seebeck Coefficient

Seebeck co-efficient (S) measured in the temperature range 100 K to 300 K for $\text{Fe}_{2-x}\text{Ti}_{1+x}\text{Sn}$ series is shown in figure 3.4. All the compositions display a positive S value that increases almost linearly with temperature. The positive value of Seebeck coefficient clarifies a hole dominated transport in the system. The parent composition, Fe_2TiSn , has the highest Seebeck coefficient of $\sim 26 \mu\text{V/K}$, matching with that reported in literature [76]. The overall magnitude of S in the entire range of temperature measured here shows a decrease with Ti substitution, reaching a minimum for $x = 0.07$, and thereafter shows a slight increase for $x = 0.1$. In case of $x = 0.07$, the overall value of Seebeck co-efficient being very low, we were able to carry out the measurement only above 150 K using our experimental setup.

In Boltzmann picture, the Seebeck coefficient can be expressed as a function of logarithmic energy derivative of electrical conductivity (σ) as, [45]

$$S = \frac{\pi^2}{3} \frac{k_B^2 T}{e} \left[\frac{\partial \ln \sigma(\epsilon)}{\partial \epsilon} \right]_{\epsilon=\epsilon_F}$$

In zero temperature limit and for free electron gas this equation

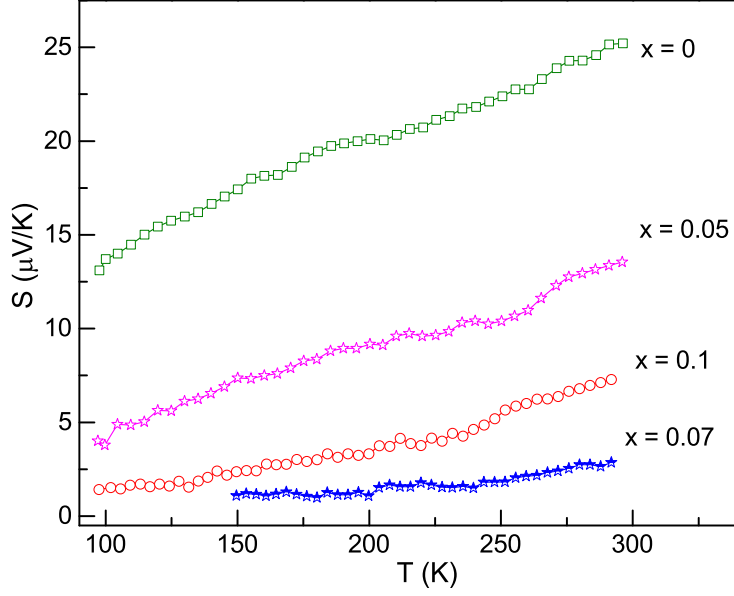


Figure 3.4: Seebeck coefficient as a function of temperature for $\text{Fe}_{2-x}\text{Ti}_{1+x}\text{Sn}$ series.

simplifies to,

$$S = \frac{\pi^2}{3} \frac{k_B^2 T}{e} \frac{N(\epsilon_F)}{n} \left(1 + \frac{2\zeta}{3} \right)$$

where $N(\epsilon_F)$ is the density of states at the Fermi level, n is the carrier concentration and ζ is the exponent of energy dependence of scattering time (τ) in the relation, $\tau = \tau_0 \epsilon^\zeta$. With Ti substitution, the parameters that get affected are n and ζ . Substitution of Ti increases carrier (hole) concentration in the series which in turn decreases the Seebeck coefficient. On the other hand, value of ζ or the scattering time, τ , in general depends directly on the ordering of the system [50, 80]. Since the disorder decreases up to $x = 0.07$ and then increases once again for $x = 0.1$, the influence of ζ is seen in raising S for $x = 0.1$ after systematic fall until $x = 0.07$ of Ti substitution.

3.2.3 Resistivity

Resistivity measured as a function of temperature for $\text{Fe}_{2-x}\text{Ti}_{1+x}\text{Sn}$ series is shown in figure 3.5. It is found that overall magnitude of

resistivity (ρ) decreases drastically with increase in Ti concentration. Fe_2TiSn has a ρ value of $421 \mu\Omega \text{ cm}$ at room temperature, classifying the sample in a dirty metal regime. After only 2.5% Ti substitution (i.e. $x = 0.05$), this value comes down to $69.17 \mu\Omega \text{ cm}$, bringing it to the moderate resistivity regime [58]. The p – type nature of $\text{Fe}_{2-x}\text{Ti}_{1+x}\text{Sn}$ series is unambiguously proved from the thermopower measurements discussed above. Replacing Fe with Ti adds holes to the system fully justifying the fall in its overall resistivity.

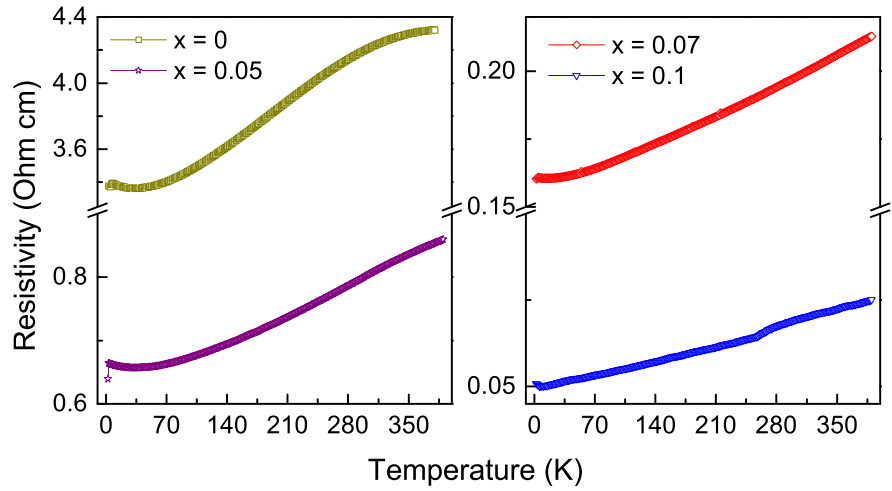


Figure 3.5: Resistivity measured as a function of temperature for $\text{Fe}_{2-x}\text{Ti}_{1+x}\text{Sn}$ series.

In the low-temperature region of $\rho(T)$, we obtain a small upturn below 50 K for Fe_2TiSn that matches with the reports in literature [83]. As discussed in the chapter 4.2.1, the origin of this shallow minimum is debatable with equally contended arguments in favour of heavy fermionic metal [83], and of Schottky anomaly arising from magnetic clusters [19]. In the present study, we find that the upturn decreases conveniently after substitution of only 5% Ti in the system. This observation leads us to believe that the origin of the rise in $\rho(T)$ lies in Fe-Ti anti-site disorder present in the parent system. Disordered systems lead to coherent backscattering of charge carriers, resulting in negative temperature coefficient of $\rho(T)$, especially at low temperatures [67]. As shown in figure 3.6

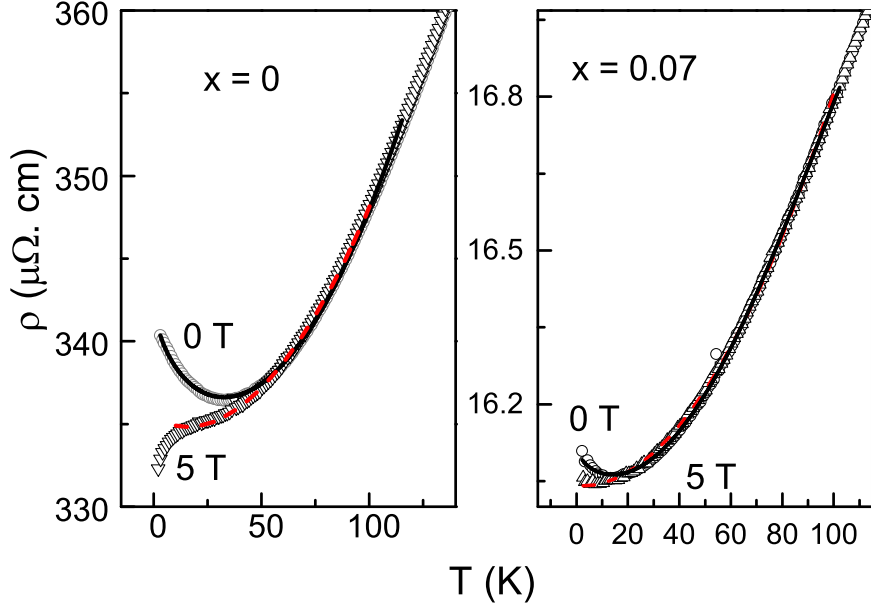


Figure 3.6: Fit to $\rho(T)$ of Fe_2TiSn in the low temperature regime (for $H = 0, 5 \text{ T}$) for two nominal compositions, showing the presence of weak localization.

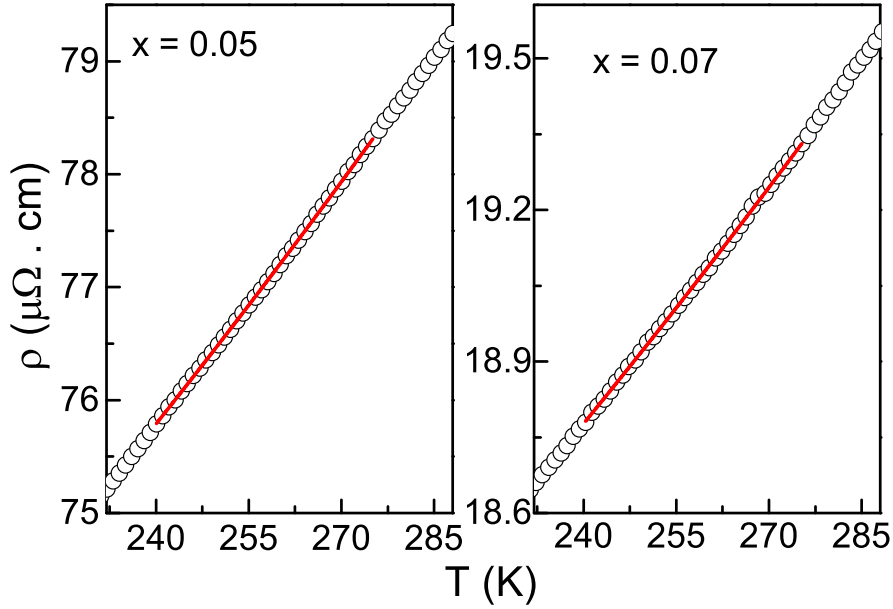


Figure 3.7: Fitting of the high temperature $\rho(T)$ for two nominal Ti – substituted compositions showing $\rho(T) = AT^{\frac{5}{3}} + B$ dependence.

the low temperature upturn in Fe_2TiSn can be very well described by the equation, $\rho(T) = A + BT^2 + CT^5 - D\sqrt{T}$, where A , B , C are residual resistivity, electron-electron scattering and electron phonon scattering respectively, and $-D\sqrt{T}$ represents the weak localization term [41] that represents the coherent backscattering of charge carriers. Weak localization directly depends on the randomness of the system. Since mere 5% substitution of Ti brings down anti-site disorder in Fe_2TiSn as seen in the XRD profile analysis and thermopower results discussed in the preceding section, the systematic fall in the weak localization feature with rising Ti – content directly correlates with the reduction in the anti-site disorder. Another point to be noted from the plots shown in figure 3.6 is that the T^2 dependence that is quite high in $x = 0$, seems to decrease with rising Ti concentration. A similar enhanced T^2 dependence has been found in some weak itinerant ferromagnets like Ni_3Al [23] or Y_4Co_3 [36].

In weak itinerant ferromagnets the quadratic dependence in $\rho(T)$ represents spin fluctuations in the temperature range, $T < T_c$ [54]. Hence the T^2 dependence observed in the present $\rho(T)$ data for $\text{Fe}_{2-x}\text{Ti}_{1+x}\text{Sn}$ series hints towards the presence of spin – flip scattering of charge carriers from the spin density fluctuation of d electrons. Further, as seen from figure 3.6, the temperature range of T^2 variation decreases for $\rho(T)$ measured under an applied magnetic field. The applied field tries to quench the spin fluctuation leading to a decrease in Fermi liquid like state [87].

To further strengthen our argument of presence of spin fluctuations in $\text{Fe}_{2-x}\text{Ti}_{1+x}\text{Sn}$, we find that our high temperature resistivity data (above 240K) displays a $T^{\frac{5}{3}}$ dependence, as predicted by the spin fluctuation theory for itinerant ferromagnets just below and above the T_c [54]. This kind of temperature dependence has also been seen experimentally in other itinerant ferromagnets like, Y_4Co_3 [36] and Y_2Ni_7 [11]. The reported Curie temperature for

Fe_2TiSn is $\sim 260\text{K}$, and assuming that small amount of Ti substitution does not change the T_C to a great extent, we fit the resistivity around 260 K. The resultant fit for two of the compositions are shown in the figure 3.7, proving the itinerant nature of magnetism in the high temperature region and thus complementing our argument.

3.2.4 Heat capacity

Heat capacity (C_P) for the entire $\text{Fe}_{2-x}\text{Ti}_{1+x}\text{Sn}$ series has been measured in the temperature range 1.5 K – 300 K, as presented in figure 3.8. All the compositions show similar temperature variation, a flat low temperature region followed by a rapid increase in C_P at higher temperature, a common for metallic systems. The specific heat at low temperature consists of a sum of two independent contributions, electronic and lattice (or phonon) vibrations and can be expressed as, $C_P(T) = \gamma T + \beta T^3$, where the first term represent the electronic contribution with γ as the Sommerfeld co-efficient and the next term is the phononic contribution. The data fits well to this equation over a wide temperature range (1.5 K - 31 K) as shown in figure 3.9 The point of interest here is the enhanced value of γ in all the compositions. The highest value of $21.3 \text{ mJ mol}^{-1}\text{K}^{-2}$ is obtained for Fe_2TiSn , which decreases monotonically with increasing Ti – content, reaching a value of $\sim 8 \text{ mJ mol}^{-1}\text{K}^{-2}$ for $x = 0.1$, yet considerably higher than that observed for standard metals like copper ($\sim 1 \text{ mJ mol}^{-1}\text{K}^{-2}$).

The enhanced value of γ for Fe_2TiSn corresponds to an effective mass of almost 70 times the free electron mass which is very unusual for a $3d$ transition metal alloy [54]. On the other hand, this kind of enhancement in γ value is common in weakly ferromagnetic samples having strong spin fluctuation. For example, the weak itinerant ferromagnet, ZrZn_2 , displays a γ value [94] of 45 mJ

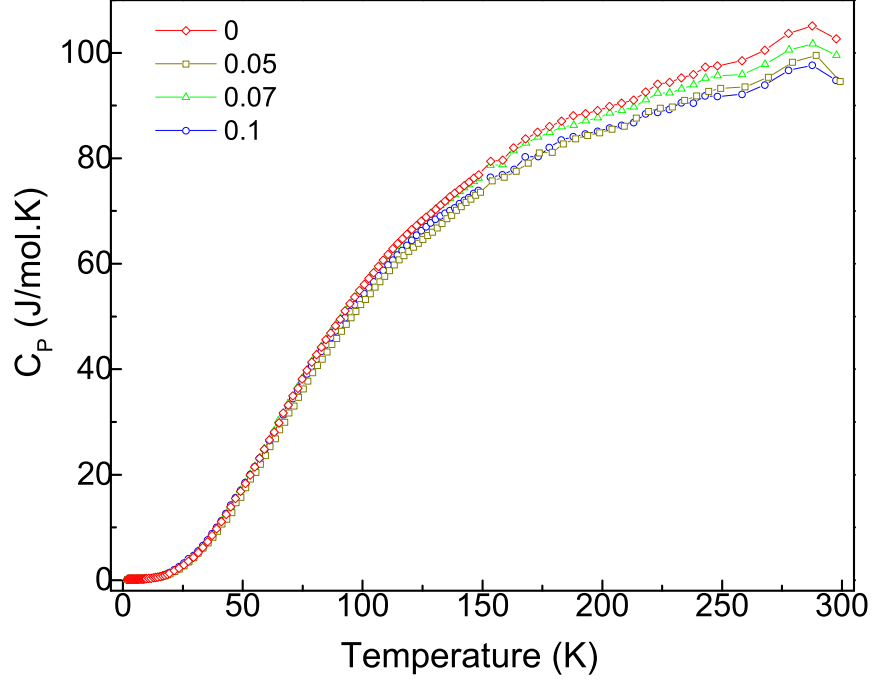


Figure 3.8: Heat capacity measured as a function of temperature for $\text{Fe}_{2-x}\text{Ti}_{1+x}\text{Sn}$ series.

$\text{mol}^{-1}\text{K}^{-2}$. Another composition, Y_4Co_3 , displays a slightly lower value of γ of $3.45 \text{ mJ mol}^{-1}\text{K}^{-2}$ and has been proved to have spin fluctuations [36]. Heat capacity generally gets enhanced by the effect of spin fluctuation as $\gamma \propto \log|1 - \alpha|$ at sufficiently low temperatures, much below the magnetic ordering temperature. $(1-\alpha)^{-1}$ is the Stoner enhancement factor in an itinerant ferromagnet, and $\alpha = 1$ represents the critical boundary for ferromagnetism. Substitution of Ti in $\text{Fe}_{2-x}\text{Ti}_{1+x}\text{Sn}$ decreases the spin fluctuation in the system as evident from the systematic decrease in γ values. The anti-site disorder that is brought down by Ti-substitution, should decrease the overall magnetic moment of the composition which in turn should decrease the spin fluctuations.

As can be seen from figure 3.9, the low temperature fitting deviates from the experimental data beyond $\sim 35 \text{ K}$. This can be understood from the fact that spin fluctuations are directly correlated to the linear coefficient γ , which itself changes with temperature in case of weak ferromagnet as, $\gamma \propto \log T$ [49] in the high tempera-

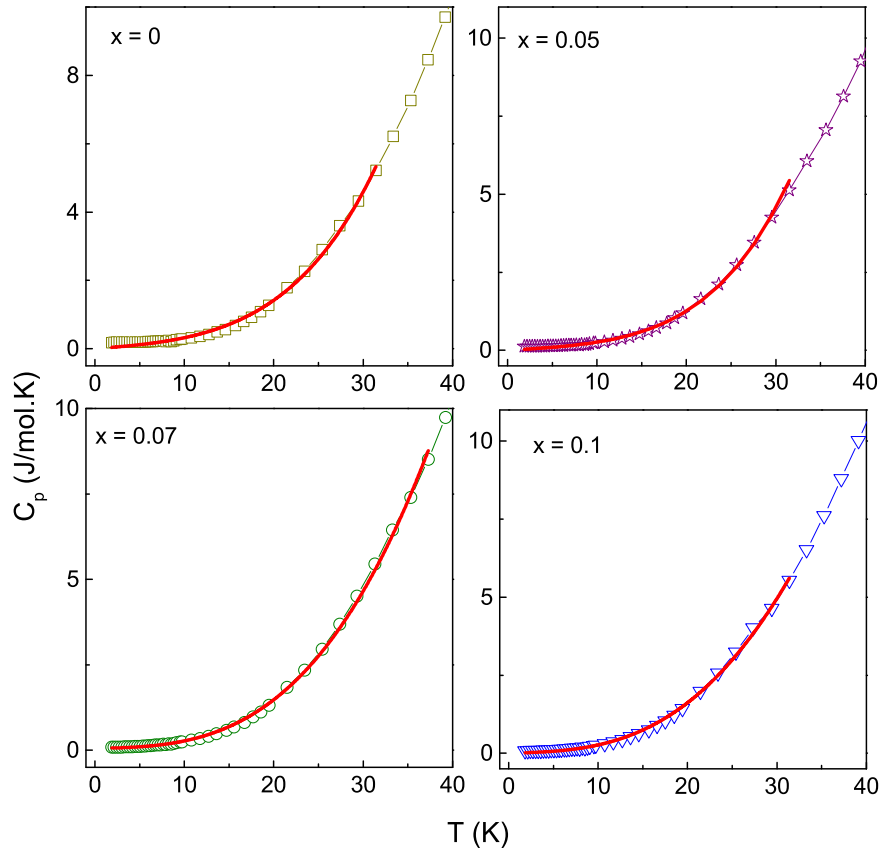


Figure 3.9: $C_p = \gamma T + \beta T^3$ fit to the low temperature data of all the compositions.

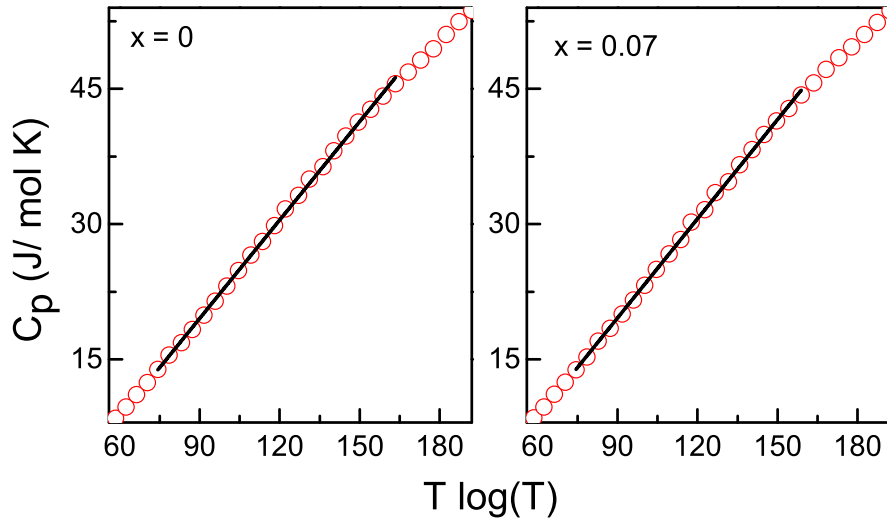


Figure 3.10: Linear variation of C_p with $T \log(T)$ in the high temperature regime.

ture regime. Increase of temperature and hence the spin fluctuation, makes it the dominant effect for heat capacity. So, neglecting the small phonon contribution term the higher temperature heat capacity should follow a $T \log(T)$ dependence [54]. As can be seen from the figure 3.10 the high temperature data for $\text{Fe}_{2-x}\text{Ti}_{1+x}\text{Sn}$ series does show a linear fit of heat capacity data to $T \log(T)$ in the temperature range of 40 K to 85 K, further confirming the presence of spin fluctuations in this system.

3.2.5 Magnetism

Resistivity and heat capacity data suggests presence of itinerant ferromagnetism and strong spin fluctuation in the $\text{Fe}_{2-x}\text{Ti}_{1+x}\text{Sn}$ samples. In an ideal fully ordered L2_1 structure, Fe atoms of Fe_2TiSn occupy the *fcc* lattice and such a system should be non-magnetic in nature. Magnetic correlations, if any, should develop only when Fe swaps position with Ti. Thus magnetic strength in such a system is proportional to Fe site disorder. Hence, to examine the magnetic ground state of these compositions, magnetization was recorded as a function of applied field ($M(H)$) with the sample temperature fixed to 5 K. The field was varied in the range 0 to 5 T.

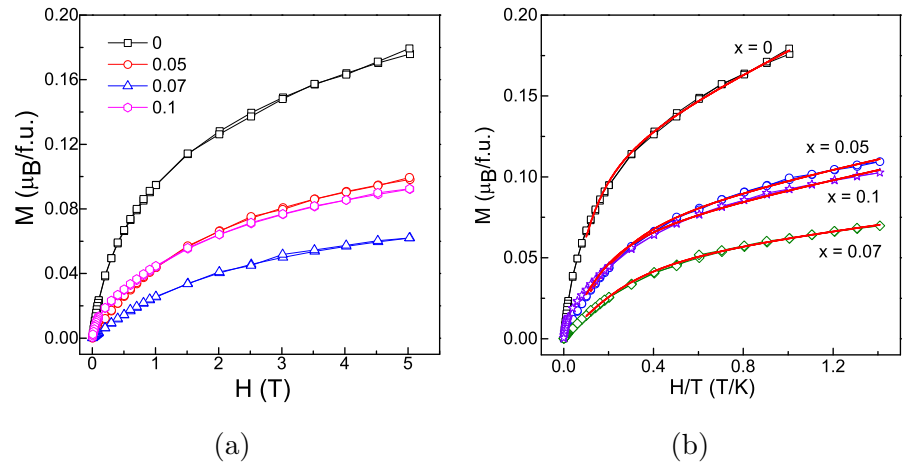


Figure 3.11: (a) M - H curves for $\text{Fe}_{2-x}\text{Ti}_{1+x}\text{Sn}$ recorded at 5 K. (b) Fit to the M vs H/T curve at 5K using the Langevin equation (see text for details).

As can be seen from figure 3.11(a), all the compositions show a ferromagnet-like increase in magnetization with rising field, though full saturation of magnetization is not achieved even with an applied field of 5 T. Also, all the curves are single valued with respect to field reversal and show no sign of hysteresis. This implies no long range ferromagnetic order to be present in the system even at the lowest measured temperature of 5 K. The saturation magnetization (M_s) was estimated by extrapolating the $M - 1/H$ curve to $1/H \rightarrow 0$ T. M_s in case of parent Fe_2TiSn composition is $0.18\mu_B/\text{f.u.}$ and decreases for higher Ti content, reaching a minimum of $0.06\mu_B/\text{f.u.}$ for $x = 0.07$ and then increases again for $x = 0.1$. The change in saturation magnetization with Ti concentration follows the same trend as structural order, supporting the anti-site disorder estimation from the XRD studies.

The situation in $\text{Fe}_{2-x}\text{Ti}_{1+x}\text{Sn}$ system can be compared to the dispersion of magnetic entities, in the otherwise non-magnetic (or paramagnetic) background. Here the excess Fe present on the disordered atomic sites acts as the magnetic scatterer. Such a system can give rise to signatures depicting a superparamagnetic ground state. Indeed, the magnetization data at 5K fits to the modified Langevin function that includes superparamagnetic and paramagnetic contribution, and represented by, $M(H) = M_s [\coth(\alpha) - \frac{1}{\alpha}] + \chi H$, with $\alpha = \frac{\mu H}{k_B T}$. Here μ is the average magnetic moment of the magnetic clusters, M_s is the saturation magnetization and χH represents the paramagnetic contribution. The measured $M(H)$ data fits nicely to this equation as shown in figure 3.11(b). The value of average magnetic moment per cluster, μ , is plotted as a function of Ti – concentration (x) in figure 3.12. In accordance with the anti-site disorder in the system, μ falls from a value of $24.4\mu_B$ for $x = 0$ to reach a minimum of $10.6\mu_B$ for $x = 0.07$. High μ values for such weak magnetic systems is generally expected when in magnetic cluster phase because each cluster consists of sizeable number of atomic

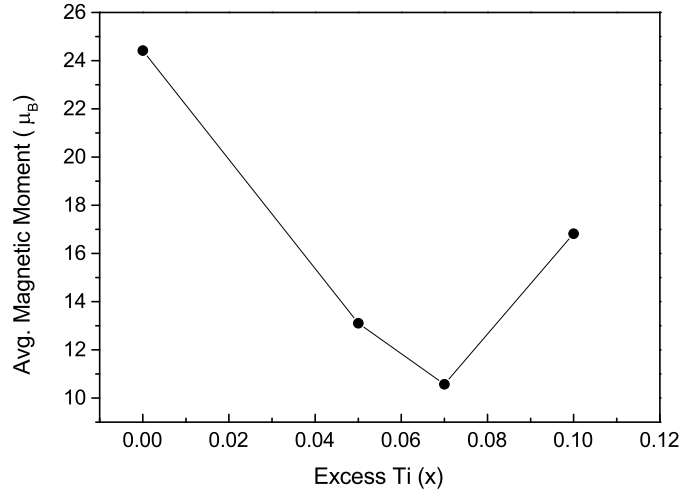


Figure 3.12: Average magnetic moment per cluster extracted from the fitting to $M(H)$ plots in $\text{Fe}_{2-x}\text{Ti}_{1+x}\text{Sn}$ series.

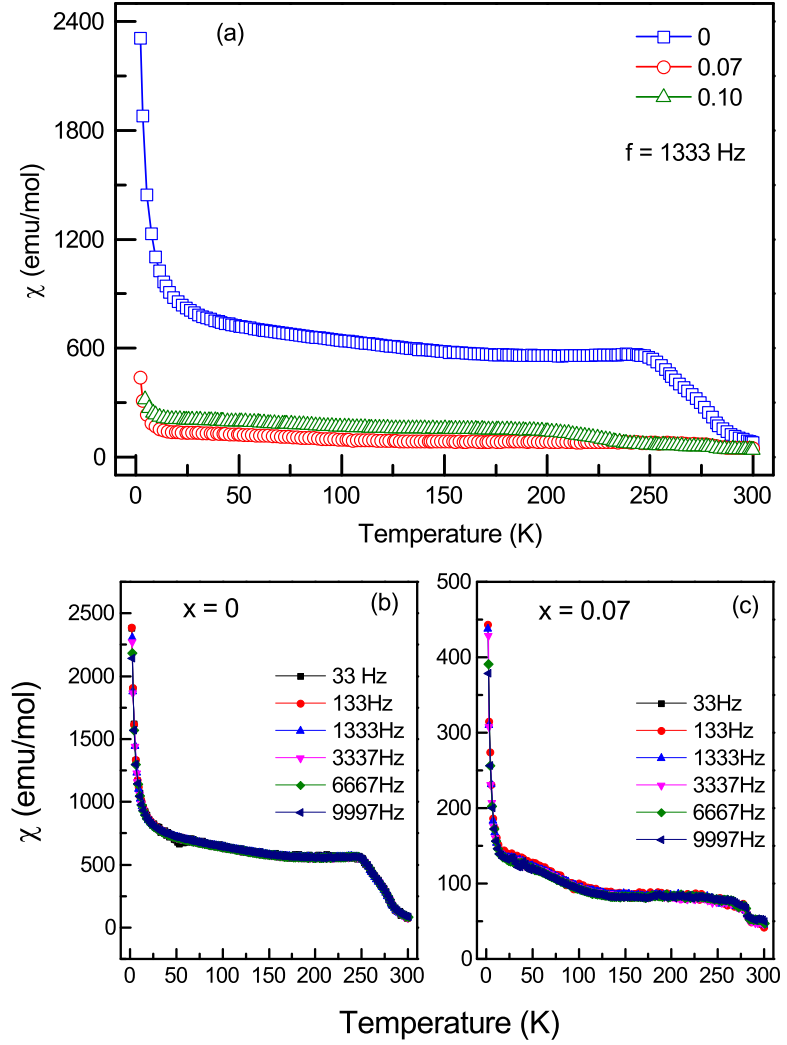


Figure 3.13: AC susceptibility as function of temperature for $\text{Fe}_{2-x}\text{Ti}_{1+x}\text{Sn}$. Inset shows the susceptibility data for Fe_2TiSn sample measured at different frequencies.

spins each having an atomic moment of few μ_B . Since each Fe atom has an atomic magnetic moment of $3.63 \mu_B$, it can be conjectured that the magnetic moment of $24.4 \mu_B$ of a cluster roughly translates to a maximum of ~ 7 Fe atomic moments being present in the cluster. An actual picture of the atomic scale magnetism and site specific moments remains to be explored unambiguously using specialized experimental techniques.

Nonetheless, the cluster dimensions can be estimated from its moment values using the relation $\mu = M_s V$, where M_s is the saturation magnetization and V is the volume of the cluster. If we assume a spherical geometry for each of these clusters, the average diameter of such entity comes out to be ~ 3 nm. Since the lattice parameter of all the compositions falls in the range of $\sim 6.06 \text{ \AA}$, around 5 unit cells can be considered to be participating in a single cluster.

The superparamagnetic nature of the compositions is also seen from the ac susceptibility (χ_{ac}) plots presented in figure 3.13. It is clear from this plot that the $x = 0$ composition is most magnetic and with a slight change in x to 0.07 or 0.1, the magnetic interactions in the system are drastically reduced. All the samples show an upturn at low temperature and a step-like feature in the high temperature regime.

Magnetization of small magnetic cluster in this case flip their spins randomly with an average time, $\tau \propto \exp(\frac{\Delta E}{kT})$. Due to highly reduced thermal effects, τ becomes larger than the measurement time at low temperature, and a higher value of magnetization is recorded. The upturn in χ_{ac} is basically the magnetic moments quickly acquiring a stable state with decreasing temperature. Thus the enhancement in susceptibility at low temperature is in accordance with the signature associated with superparamagnets. Besides, absence of any frequency dependence in the χ_{ac} measurements (see figure 3.13(b) and (c)) rules out the possibility of it being a

glassy magnetic phase.

3.3 Summary

In summary, we manipulated the anti-site disorder by systematically substituting small percentage of Ti for Fe to obtain a series of $\text{Fe}_{2-x}\text{Ti}_{1+x}\text{Sn}$ compositions. The B2 and L2_1 ordering parameters determined using synchrotron XRD studies show that the anti-site disorder indeed decreases after Ti substitution. It is also noticed that beyond a mere 3.5% Ti substitution, the disorder increases again probably due to release of the strain in the crystal structure. Analysis of the temperature dependent electrical resistivity hints towards presence of spin fluctuations in the system. This view is further supported by high value of Sommerfeld parameter extracted from the heat capacity data. Measurement of magnetic properties unambiguously prove the presence of strong spin polarization in the system. Superparamagnetic ground state is observed from the low temperature magnetization that yields a cluster consisting of ~ 5 unit cells.

Chapter 4

Half metallicity in Sb substituted Fe_2TiSn

4.1 Preamble

In chapter 3.3 we have seen that substitution of maximum 7% extra Ti in the Fe_2TiSn system can effectively decrease the antisite disorder. But in the way it also increases the internal strain in the system, which can affect the ground state physical properties. So, here we tried our second approach to decrease the antisite disorder, by substituting higher electronegative element at the Sn site.

In the present study, we substitute the Sn atoms with a higher electronegative element, Sb and explore the resulting electronic and magnetotransport properties. In particular, we present temperature dependent electrical resistivity and magnetotransport measurement of $\text{Fe}_2\text{TiSn}_{1-x}\text{Sb}_x$ with $0 \leq x \leq 1.0$, and supplement our results with *ab initio* electronic structure calculations using the GGA formalism. With its magnitude lying in dirty metal regime and a negative temperature coefficient, the electrical resistivity measurement of $\text{Fe}_2\text{TiSn}_{1-x}\text{Sb}_x$ poses an unusual electronic structure. While the conduction at low temperature can be understood from Mott's variable range hopping model, higher temperature regime is dominated by electron-phonon interaction. This is in spite of presence of sizable magneto-resistance and high anomalous Hall resistivity. Substituting Sn by Sb results in a highly polarized DOS at the Fermi level

(E_F) in Fe_2TiSn , indicative of a half metallic ground state.

4.2 Results and Discussion

4.2.1 X-Ray diffraction analysis

Figure 4.1 presents the XRD profiles of the prepared compositions. The existence of strong reflections from (111), (200), (220) planes confirms the formation of $L2_1$ phase in all the samples. As the Sb concentration increases to 80% and beyond, an extra peak starts to appear at $2\theta \sim 44.7^\circ$. As per the JCPDS database, this additional peak belongs to elemental Fe phase. A previous report suggests that Fe_2TiSb crystallizes with some percentage of elemental Fe precipitating out of the composition and influences its structural and magnetic properties [59]. Hence, in the present study further investigation of $\text{Fe}_2\text{TiSn}_{1-x}\text{Sb}_x$ was restricted only to phase pure compositions with Sb concentrations limiting to 60%. Lattice parameters (a) of the samples were obtained using Rietveld refinement method implemented in the FullProf suite [75]. The value obtained for Fe_2TiSn is $a = 6.06544 \text{ \AA}$ and agrees well with that reported in literature [82]. This value of a was taken as the initial guess to refine all other XRD profiles of Sb-substituted compositions. The obtained values as listed in table 4.1 and plotted in figure 4.2 (left axis), show monotonous decrease with rising Sb concentration. The systematic decrease in lattice parameter satisfies Vegard's law [18] as small sized Sb ion replaces Sn.

As have been discussed in chapter , the intensity ratios of the (111) and (200) reflection with the (220) reflection can give an estimate of the amount of disorder present in the sample. For the present case, both the ratios ($\frac{I_{111}}{I_{220}}$, $\frac{I_{200}}{I_{220}}$) increase with Sb content as plotted along the right axis of figure 4.2. In other words, Sb substitution increases the $L2_1$ order in an otherwise disorder prone

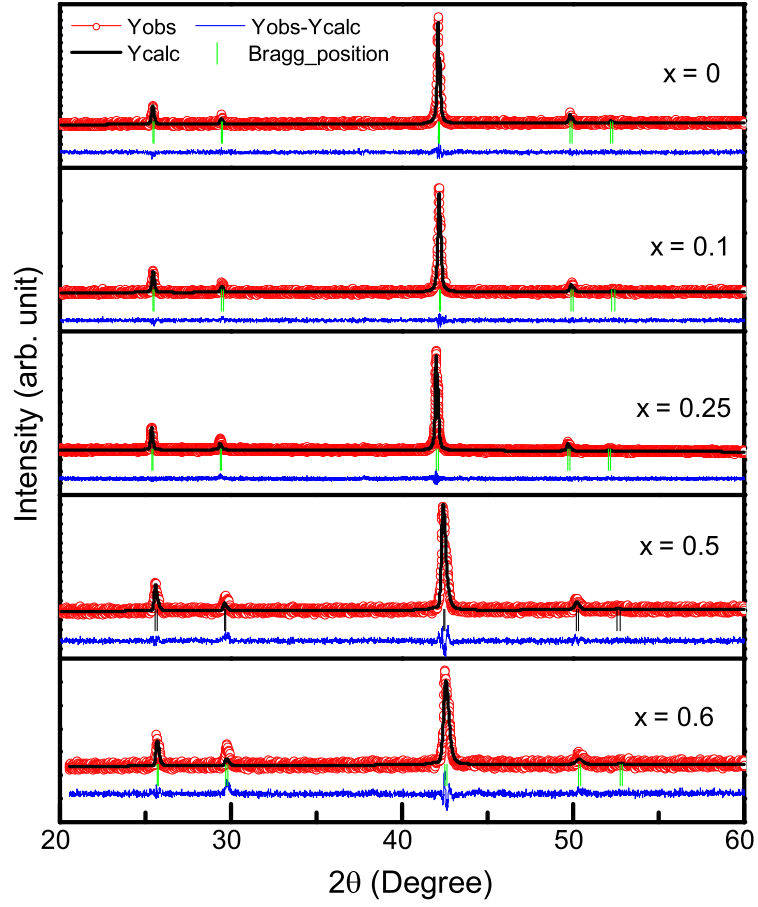


Figure 4.1: Powder XRD patterns of $\text{Fe}_2\text{TiSn}_{1-x}\text{Sb}_x$ ($x = 0, 0.1, 0.25, 0.5, 0.6$) series with Rietveld refinement fitting.

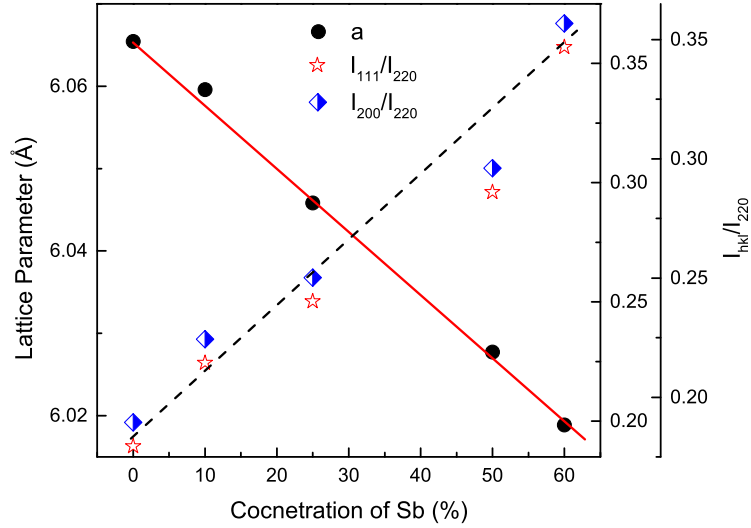


Figure 4.2: Right axis in the figure shows Lattice constant versus Sb concentration following Vegard's law, left axis are for Intensity ratios of the (111) and (200) peaks with the main (222) peak versus Sb concentration. The lines are guide to the eye.

Table 4.1: Lattice parameter obtained from reitveld refinement of the XRD patterns and the fitting parameters obtained from the fit shown in figure (4.7).

Conc of Sb %	Lattice Parameter (\AA)	R_{Bragg}	χ^2	ρ_{e-p} $\frac{n\Omega.cm}{K}$	ρ_{e-m} $\frac{p\Omega.cm}{K^2}$
0	6.06544(± 19)	7.18	1.10	0.2667	0.342
10	6.05969(± 21)	9.96	1.22	1.9557	-3.1741
25	6.04582(± 23)	5.87	1.12	1.7927	-5.5683
50	6.02772(± 29)	13.52	1.31	0.1665	-3.2857
60	6.01887(± 31)	16.92	1.32	0.0901	-4.1846

Fe_2TiSn composition, as expected, since the higher electronegativity of Sb in comparison to Sn, aids in the formation of a stronger bond with Ti, leading to decrease in the probability of Ti leaving its own (Y) site and occupying some of the Fe (X) sites.

4.2.2 Resistivity analysis

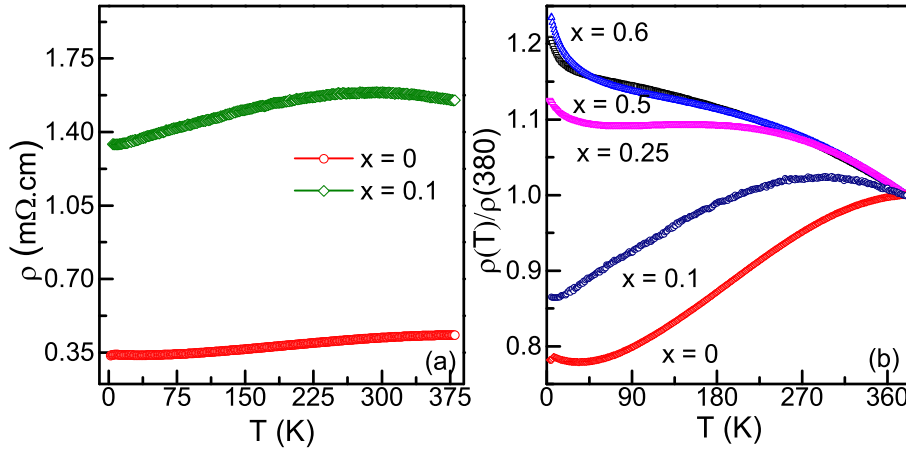


Figure 4.3: Resistivity of $\text{Fe}_2\text{TiSn}_{1-x}\text{Sb}_x$ series. (a) Absolute resistivity as a function of temperature of $x = 0$ and 0.1 samples to show the order of change with doping. (b) Resistivity of all samples versus temperature normalized by their value at 380 K.

Next, we discuss the temperature variation of electrical resistivity ($\rho(T)$), measured for all the samples in the temperature range 5 K to 380 K and an applied magnetic field, $H = 0, 5, 8$ T. The plots obtained for $H = 0$ are shown in figure 4.3. Fe_2TiSn displays a metallic nature of resistivity in the entire measurement range, with room

temperature value of $\sim 421 \mu\Omega(\text{cm})^{-1}$. With just 10% Sb substitution the overall resistivity increases giving a room temperature value of $\sim 1.588 \text{ m}\Omega(\text{cm})^{-1}$ as shown in figure 4.3(a). As there is a further rise in Sb content to 25% and above, resistivity begins to decrease with increasing temperature depicting a semiconducting nature, as shown in figure 4.3(b). The overall magnitude of conductivity ($\sigma_{xx} \sim 3000 - 200 (\Omega\text{cm})^{-1}$) can be classified to be in a dirty metal regime. In the low-temperature region of $\rho(T)$, we obtain a small upturn be-

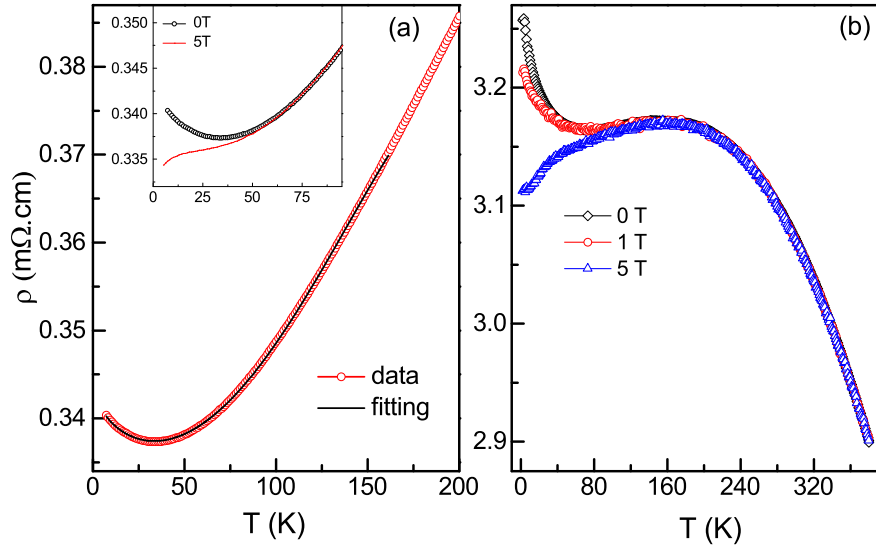


Figure 4.4: (a) Fitted curve for low temperature resistivity of Fe_2TiSn sample, solid line indicates the fit to the equation $\rho(T) = A + BT + CT^5 - D\sqrt{T}$. Inset: Effect of application of magnetic field on the low temperature resistivity of same sample, (b) Effect of application of magnetic field on the resistivity of $\text{Fe}_2\text{TiSn}_{0.75}\text{Sb}_{0.25}$ sample.

low 50 K for Fe_2TiSn , resulting from weak localization of electrons, as discussed in chapter 3.3. In the present study, we find that the upturn disappears with 10% Sb substitution. As shown in figure 4.4(a) the low temperature upturn in Fe_2TiSn can be very well described by the equation, $\rho(T) = A + BT^2 + CT^5 - D\sqrt{T}$, where A, B, C are residual resistivity, electron-electron scattering and electron phonon scattering respectively, and $-D\sqrt{T}$ represents the weak localization term [41] that represents the coherent backscattering of charge carriers. Weak localization directly depends on the randomness of the

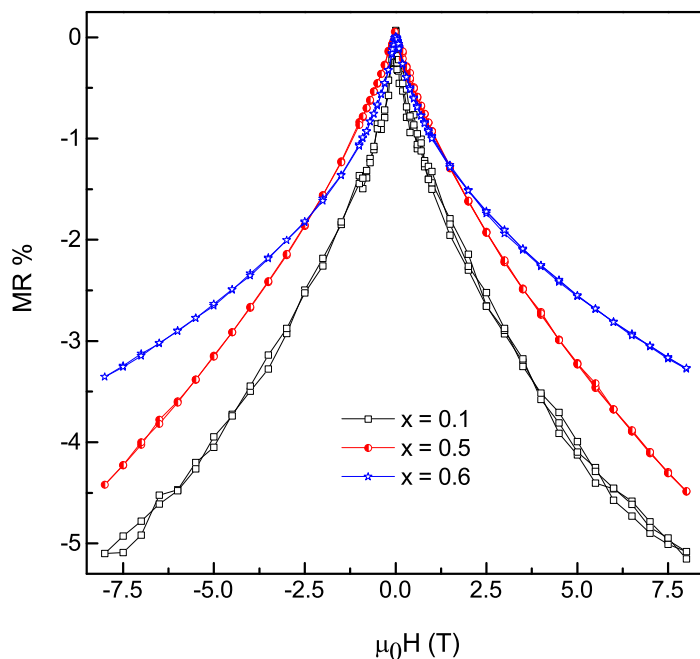


Figure 4.5: $MR = \frac{\rho(H) - \rho(0)}{\rho(0)} \times 100\%$ as a function of applied magnetic field for $Fe_2TiSn_{1-x}Sb_x$ samples.

system. Since mere 10% substitution of Sb brings down anti-site disorder in Fe_2TiSn as seen in the XRD profile, its electrical resistivity does not show any upturn at low temperature. However, with Sb-content rising to 25% and higher, a semiconductor-like behavior of $\rho(T)$ is observed with the magnitude of $\rho(T)$ lying in the dirty metal regime. On application of magnetic field, the semiconductor-like rise changes to metallic for $x = 0.25$ (see figure 4.4), supporting the weak localization scenario in these materials.

On the other hand, application of magnetic field to $\rho(T)$ of $x = 0.5$ and 0.6 samples though successful in reducing its overall magnitude, does not change its negative temperature coefficient of resistance. The decrease in resistance with application of magnetic field is also seen from the $\rho(H)$ measured at 5 K by ramping the magnetic field from +8 T to -8 T (see figure 4.5). However, to understand negative temperature coefficient of resistance in the $x = 0.5$ and 0.6 samples, we consider the universal conduction mech-

anism in bad metals that proceeds via electron hopping between spatially localized states. Such a type of conduction is known as the Mott - *variable range hopping*(VRH) [56]. The hopping conduction takes place from narrow bands near Fermi level and the hopping probability is given by the expression, $A \exp(-2\alpha a - \frac{W}{k_B T})$, where a is the hopping length and α is the inverse fall of length of the electronic wave function. W is the hopping energy given by the expression, $W = \frac{3}{4\pi R^3 g(\mu)}$, where $g(\mu)$ is the density of state at the Fermi level; an electron hops to a state where it finds a minimum W . The temperature dependence of resistivity in Mott's VRH model is described by $\sigma = \sigma_0 \exp -(\frac{T_0}{T})^\nu$, with $T_0 = \frac{\beta}{k_B g(\mu) a^3}$. Here β is a numerical constant, and the exponent ν is $\frac{1}{4}$ for bulk systems. We plot the recorded resistivity data in the form of $\log \sigma(T)$ vs $T^{-\frac{1}{4}}$ as can be seen from figure 4.6. Samples with $x = 0.5$, and 0.6 give a good fit over a relatively broad temperature range, down to ~ 8 K. Application of the magnetic field aids the sample in overcoming the localization potential as the VRH model fit to the $\rho(T)$ (with $H = 5, 8$ T) curves yield a characteristic temperature, T_0 (listed alongside the plots in figure 4.6), that decreases with increasing magnetic field. Referring to the expression for T_0 , it is easy to notice that application of magnetic field implies an increase in hopping length of the carriers.

The high temperature resistivity behaviour is manifestation of electron-phonon, and electron-magnon interaction. As already seen from figure 4.5, the quadratic nature of $\rho(H)$ reveals the ferromagnetic order of these samples. Hence, at temperatures higher than the VRH limit (~ 80 K), and up to 300 K, the resistivity data fits the equation, $\rho(T) = \rho_0 + \rho_{ep}T + \rho_{em}T^2$, where $\rho_{ep}T$ and $\rho_{em}T^2$ represent the electron-phonon, and electron-magnon interaction (or electron-electron interaction), respectively. The fittings are shown in figure 4.7 and the parameter values are given in table 4.1. Except in the case of Fe_2TiSn , the values obtained for ρ_{em} are al-

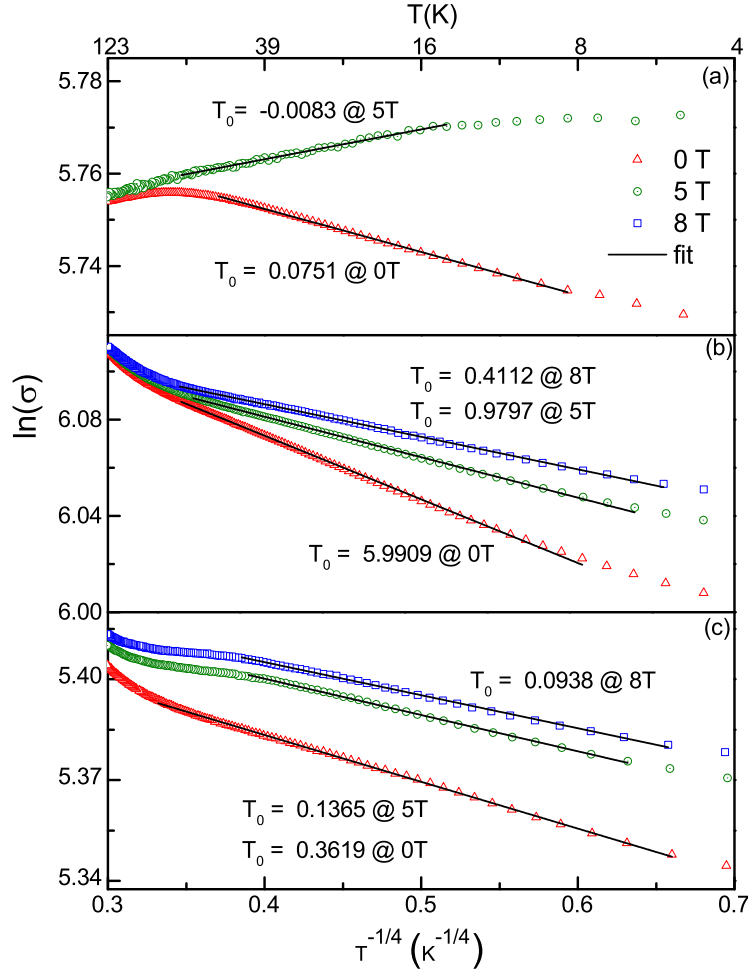


Figure 4.6: Fitted curves of $\ln(\sigma)$ versus $T^{-1/4}$ for (a) $x=0.25$, (b) $x=0.5$ and (c) $x=0.6$ samples with and without the application of magnetic field. Solid line indicates the linear fit. Value of characteristic temperature obtained from the fit are shown in the graph.

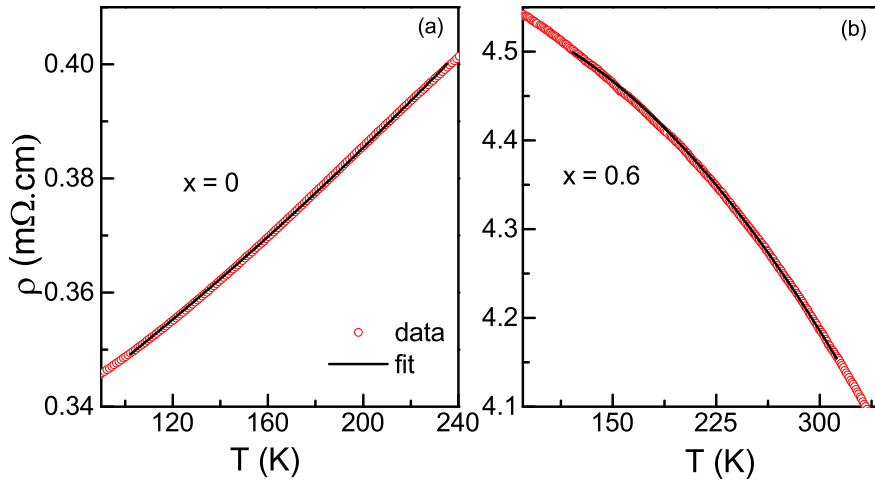


Figure 4.7: Fitted curves for high temperature resistivity as a function of temperature. (a) $x=0$, (b) $x=0.6$. Solid line indicates the fit to the equation $\rho(T) = \rho_0 + \rho_{ep}T + \rho_{em}T^2$.

ways negative and small compared to ρ_{ep} , suggesting the dominance of electron-phonon interaction in the fitted region. The electron - magnon scattering is a spin flip process and requires minority spins to complete. So, the negligible electron - magnon interaction in ferromagnetically ordered regime indicates a lack of minority spin electrons at the Fermi level. L. Bainsla *et. al* [7] showed that such type of fitting to the resistivity data of $\text{Fe}_{3-x}\text{Mn}_x\text{Si}$ was an indication of its half metallic ground state. Moreover, the previously reported DOS calculations for Fe_2TiSn and Fe_2TiSb , predict a semi-metallic [82] and half-metallic ground state [59], respectively, for the two end-members of the present series.

4.2.3 Density of States calculation

The DOS for $\text{Fe}_2\text{TiSn}_{1-x}\text{Sb}_x$ compositions was hence calculated using the plane wave pseudopotential method. Ultrasoft Pseudopotential with GGA exchange correlation as implemented using Quantum Espresso package was used and the obtained DOS for $x = 0, 0.25$, and 0.5 and 1.0 are plotted at figure 4.8. While we were able to successfully replicate the reported DOS structure for Fe_2TiSn and Fe_2TiSb , the DOS obtained for Sb-substituted compositions match the behaviour anticipated from its transport properties. Here, we observe a clear half-metallic nature with a band gap of 0.133 eV and 0.285 eV in case of $x = 0.25$ and $x = 0.5$, respectively. Substitution of Sb at Sn site shifts the Fermi level to the higher energy side in case of majority spin band, while the corresponding decrease of lattice parameters increases the Fe $d - d$ hybridization, resulting in a band gap at its minority spin channel.

Next, Hall effect measurements were carried out on all the compositions in order to obtain some insight into the magnetic phase of Sb-substitution on Fe_2TiSn . $\rho_{xy}(H)$ data measured at different temperatures is shown in figure 4.9. Apart from the normal Hall

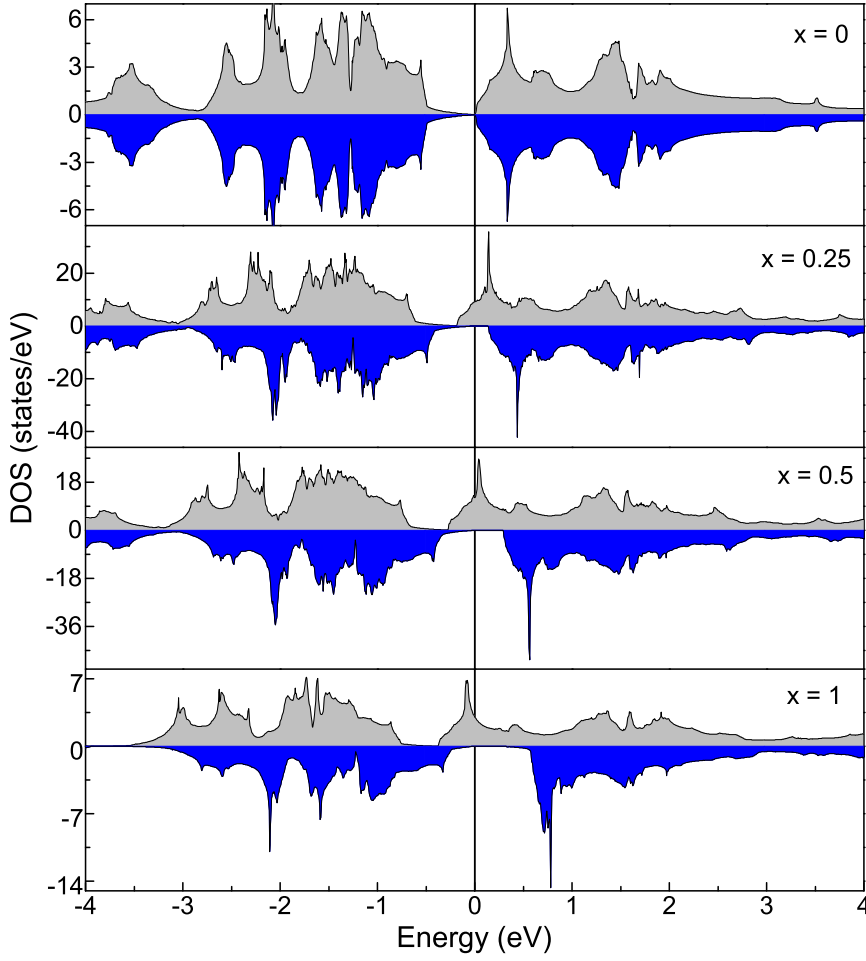


Figure 4.8: Calculated total DOS for $\text{Fe}_2\text{TiSn}_{1-x}\text{Sb}_x$ samples. x values are shown in the graph.

resistance R_0 resulting from Lorentz force on the charge carriers, we observe an anomalous Hall resistance, $\rho_{xy}^{AHE}(H)$ that arises due to spontaneous magnetization in the Sb-substituted compositions. $\rho_{xy}^{AHE}(H)$ is found to steadily increase with increasing Sb - content. The parent composition, Fe_2TiSn , initially shows a negative value of $\rho_{xy}(H)$ at 10 K, and changes to a positive value at $T = 30$ K and above. The change in sign of $\rho_{xy}(H)$ is mainly caused by the band filling effect.

As has been discussed above, the electrical conduction at low temperatures in Fe_2TiSn is governed by a weak localization of charge carriers due to inherent anti-site disorder [21, 62]. At higher temperatures, the system gains enough energy to overcome such localiza-

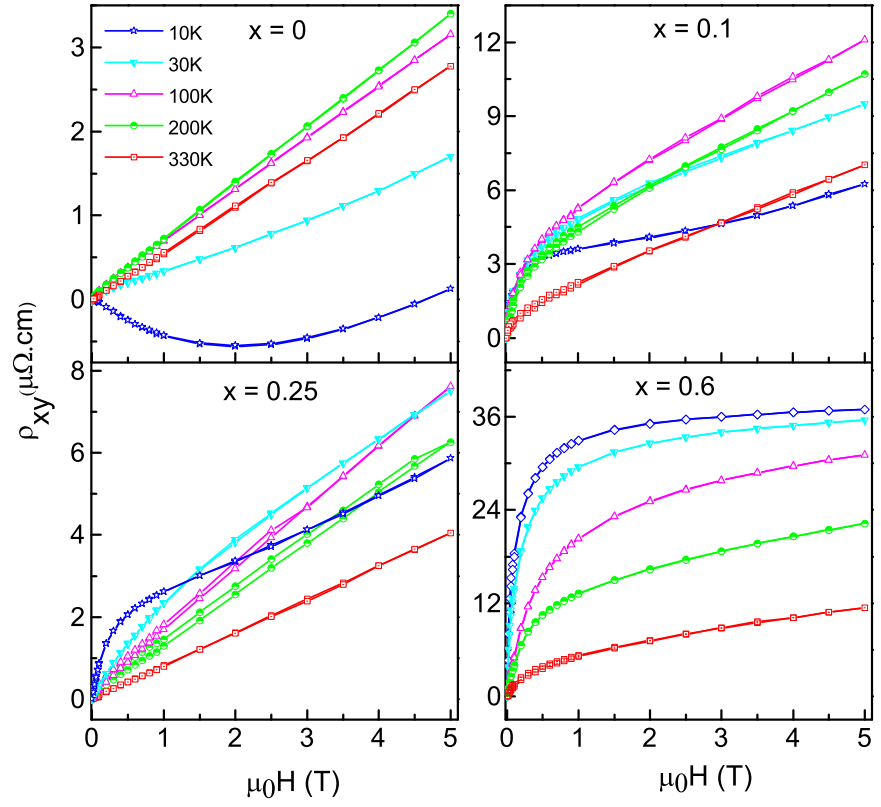


Figure 4.9: Hall resistivity versus temperature for $\text{Fe}_2\text{TiSn}_{0.75}\text{Sb}_{0.25}$ samples. (a) $x = 0$, (b) $x = 0.1$, (c) $x = 0.25$, (d) $x = 0.6$

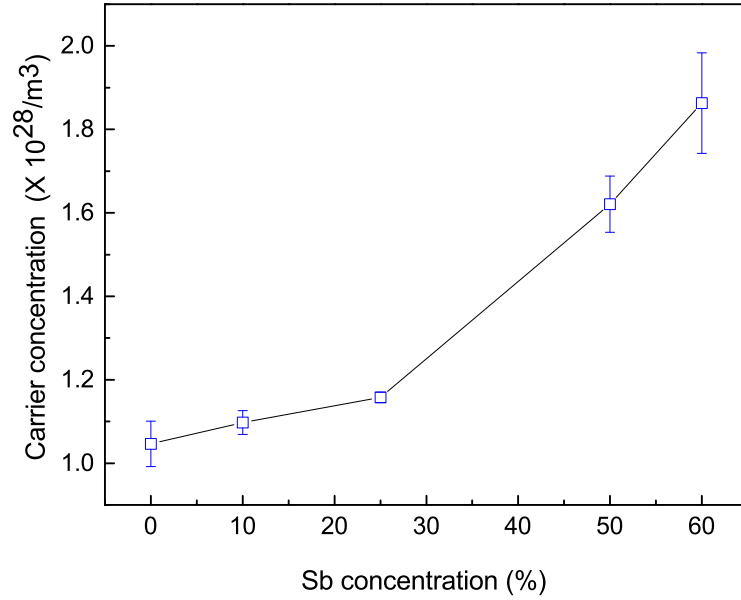


Figure 4.10: Charge carrier density of $\text{Fe}_2\text{TiSn}_{1-x}\text{Sb}_x$ samples as a function of Sb concentration measured at 10 K.

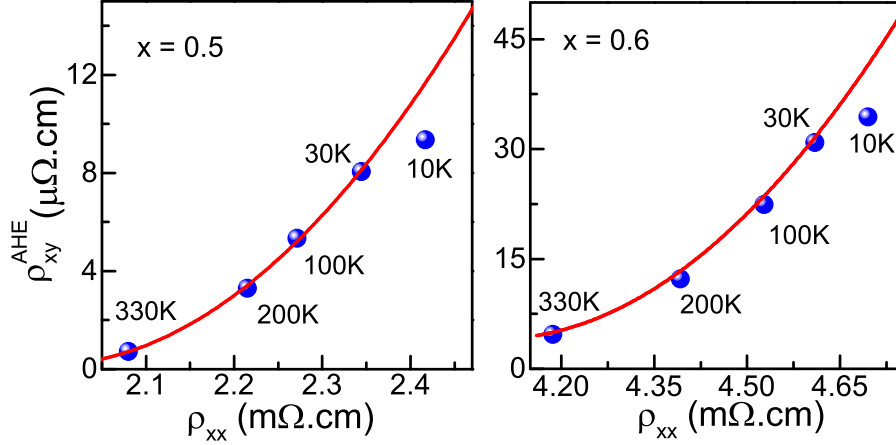


Figure 4.11: Fitted graph of anomalous hall resistivity (ρ_{xy}^{AHE}) versus zero field resistivity (ρ_{xx}), Solid line indicates the fitting with the equation $\rho_{xy}^{AHE}(H) = C(\rho - \rho_R)^2$

tion and typical metallic conduction is established. This argument is further supported by the positive value of $\rho_{xy}^{AHE}(H)$ observed in the Sb-substituted compositions. As the Sb-content increases, disorder decreases and hence $\rho_{xy}^{AHE}(H)$ is not only positive, it systematically grows in magnitude. Further, there is an increase in the carrier concentration (N_e), as Sb has one electron more in the valence band than Sn. N_e can be calculated from the normal Hall co-efficient (R_H) using the relation $N_e = \frac{1}{e \times R_H}$ and its plot as a function of Sb-content is shown in figure 4.10.

ρ_{xy}^{AHE} is commonly attributed to one of the three mechanisms, *viz.*, skew scattering of charge carriers from impurities, side jump mechanism and intrinsic contribution from band structure or the Berry phase effect [89]. Each of these mechanisms can be expressed as some function of longitudinal resistivity (ρ_{xx}). In skew scattering mechanism ρ_{xy}^{AHE} varies linearly with the ρ_{xx} , while side jump and Berry phase mechanisms show a quadratic ρ_{xx} variation. figure 4.11 presents $\rho_{xy}^{AHE}(H)$ as a function of longitudinal resistivity for the samples with $x = 0.5$ and 0.6 . The data fits well with the equation, $\rho_{xy}^{AHE}(H) \propto (\rho - \rho_R)^2$, where ρ_R is the residual resistivity [13]. The coefficient of quadratic part is higher than the linear part, implying that either side jump or intrinsic mechanism can responsible

for the observed anomalous Hall effect. Also it is to be noted that Berry curvature of the Bloch electrons effects in an unequally populated Fermi level, *i.e* unequal number of spin up and spin down electrons, as seems to be the case in the present series. A distinct deviation from the parabolic dependence is observed for the data point corresponding to 10 K . At such low temperature, saturation of magnetization to high magnetic moment may be responsible for the deviation of the anomalous hall resistance from the fit.

4.3 Summary

In summary we investigated the structure, electrical transport and magneto-transport properties of $\text{Fe}_2\text{TiSn}_{1-x}\text{Sb}_x$ series. The anti-site disorder between Fe and Ti decreases drastically upon substitution of Sb at Sn site. However, the electrical resistivity of the Sb-substituted compositions increase, giving rise to a negative temperature coefficient of resistance when $x \geq 0.25$. This is in contrast with the normally anticipated behaviour of increase in conduction with increase in carrier concentration as Sb has one electron more than Sn. The electrical conduction in the low temperature regime can be best described by Mott's variable range hopping model. At higher temperatures the conduction is dominated by electron-phonon interaction rather than electron-magnon scattering. Also, high anomalous hall resistivity(ρ_{AHE}) was observed for $x \geq 0.25$ compositions, and, $\rho_{AHE} \sim \rho_{xx}^2$ implying an intrinsic Berry phase mechanism to be dominant in Hall resistivity. Our electronic structure calculations yield a clear half-metallic DOS for all compositions with $x \geq 0.25$.

Chapter 5

On the origin of magnetic ordering in Z site substituted Fe_2TiSn

5.1 Preamble

In the preceding chapter, it has experimentally been demonstrated that substituting a higher electronegative element like Sb at Sn site decreases the anti-site disorder in Fe_2TiSn and $\geq 25\%$ Sb-substitution leads to a *half-metallic* ground state. From this perspective, Ge and Si being more electronegative than Sn, its substitution at Sn site can also be expected to bring down the anti-site disorder and display exotic ground state. Moreover, electronic structure calculations by Yabuuchi *et al* [93] also indicate tuning of the transport and thermoelectrical properties in a $\text{Fe}_2\text{TiSn}_{1-x}\text{Si}_x$ type solid solution.

With this aim, we carried out a systematic investigation into $\text{Fe}_2\text{TiSn}_{1-x}\text{Z}_x$ ($\text{Z} = \text{Si}, \text{Ge}, \text{Sb}$) compositions. The limit of solubility of Si and Ge in Fe_2TiSn was determined from a detailed X-ray diffraction study carried out using synchrotron X-rays. Measurement of electrical resistivity as a function of temperature and analysis of the obtained data reflect the change taking place in the electronic charge transport of the solid solutions. Study of the magnetic properties indicate a magnetically ordered ground state, which

is an important observation since the pristine Fe_2TiSn composition is non-magnetic in nature, so are the Sb, Ge, and Si substituent. The interaction between constituent atoms that lead to the magnetically ordered state has been explored from the local crystal structural point of view using EXAFS spectroscopy. All the obtained results are matched with our orbital projected density of states calculations carried out using density functional theory.

5.2 Results and discussion

5.2.1 X-ray diffraction analysis

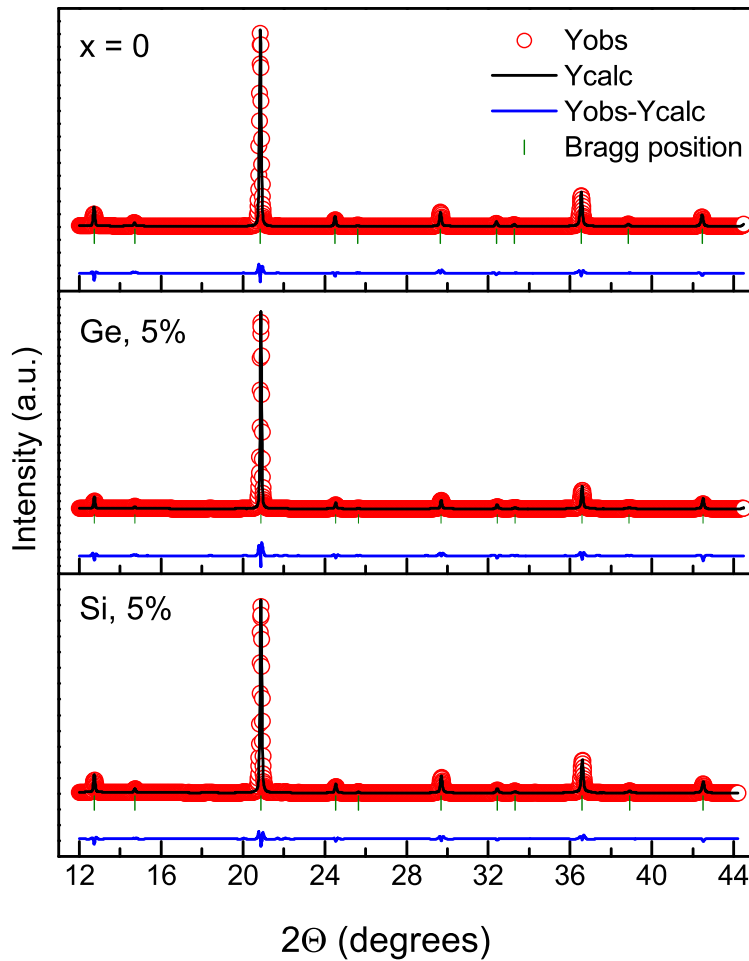


Figure 5.1: Synchrotron X-ray diffraction ($\lambda = 0.776 \text{ \AA}$) patterns obtained for $\text{Fe}_2\text{TiSn}_{0.95}\text{M}_{0.05}$ with $\text{M} = \text{Si}$ and Ge .

Room temperature XRD profiles of $\text{Fe}_2\text{TiSn}_{0.95}\text{X}_{0.05}$ (where X = Si, Ge) compositions recorded using high intensity synchrotron source are shown in figure 5.1. All the peaks can be indexed with a face center cubic lattice with $F\bar{m}3m$ space group, confirming the phase purity of the prepared samples. Besides, the 2θ range over which the XRD profiles have been recorded translates into a d -spacing of $\sim 3.8 \text{ \AA}$ to 1.0 \AA , thus encompassing a sufficiently wide range to identify the presence of any secondary phase.

Table 5.1: Lattice parameters obtained from the Rietveld refinement of the XRD profiles, goodness of fit parameters (R_{Bragg} and χ^2)

Chemical composition	Lattice Parameter (\AA)	R_{Bragg}	χ^2
Fe_2TiSn	6.0656(4)	4.05	2.47
Ge, 5%	6.0619(7)	4.25	2.53
Si, 5%	6.0583(5)	4.79	2.32

No peak other than that of the Heusler phase is found in this range of 2θ for all the XRD patterns discussed here, discounting the formation of any secondary phase. Representative fits to the XRD patterns obtained using the Rietveld refinement technique and implemented through FULLPROF suite [75] are also presented herewith. The extracted lattice parameters are shown in table 5.1. Though atomic size of Si and Ge is much smaller than Sn, the substitution is limited to only 5%. Hence no notable change is seen in the lattice parameters of both the compositions. Increasing the percentage of substitution gives rise to formation of binary phases like Fe_3Ti and FeSn , thus indicating 5% to be the optimal solubility limit that yields single phase Heusler composition. This agrees with the fact that despite theoretical studies predicting significant technological advantages for full Heusler Fe_2TiSi or Fe_2TiGe , no experimental study has been reported till date. In contrast, the solubility of Sb in Fe_2TiSn seems to be quite high as there is only slight difference in the atomic sizes of Sn and Sb. The secondary phase begins to appear only after 60% Sb-substitution. The XRD patterns

for $\text{Fe}_2\text{TiSn}_{1-x}\text{Sb}_x$ with $0 \leq x \leq 0.6$ have been presented in chapter 4.3 and hence not included here. However, the lattice parameters for 25% and 50% Sb is 6.0458(2) Å, and 6.0277(3) Å, respectively. In accordance with Vegard's law, a systematic decrease in unit cell volume with the increasing Sb-content is noticed here.

5.2.2 Resistivity measurement

Resistivity measured as a function of temperature for all prepared samples are shown in figure 5.2. Fe_2TiSn shows the resistivity value of $421 \mu\Omega\text{cm}$ at 300 K, classifying it to be in a dirty metal regime. Surprisingly, a drastic decrease in overall magnitude of resistivity ($\sim 2 \mu\Omega\text{cm}$ at 300 K) is seen with only 5% Si (or Ge) substitution at Sn site, placing these compositions in the good metal regime. The resistivity of pristine Fe_2TiSn is known to be affected by the inherent Fe-Ti anti-site disorder, giving rise to spin-fluctuations and weak localization at low temperature as discussed in chapter 3.3. In ad-

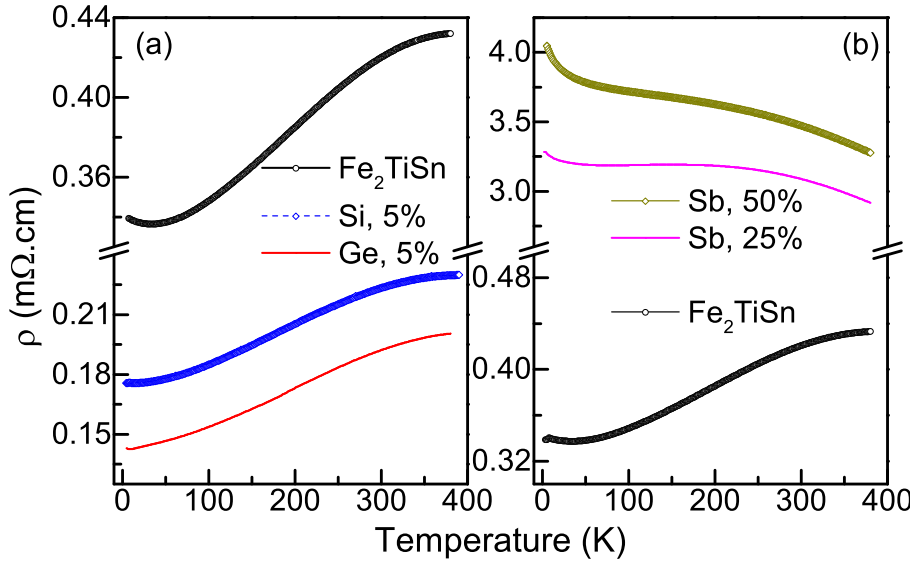


Figure 5.2: Resistivity measured as a function of temperature for (a) $\text{Fe}_2\text{TiSn}_{0.95}\text{M}_{0.05}$ (M = Si, Ge) and, (b) $\text{Fe}_2\text{TiSn}_{1-x}\text{Sb}_x$ ($x = 0.25, 0.5$) compositions.

dition, replacing some of the Sn atoms with Si or Ge will contribute positively to the static chemical disorder of Fe_2TiSn . Hence, to get

a better insight into the low temperature conduction process, the resistivity plots were fitted with the equation $\rho(T) = \rho_0 + BT^2 + CT^5 - DT^{\frac{1}{2}}$. Here, ρ_0 is the residual resistivity and the coefficients B , and C associated with T^2 and T^5 encompasses the electron-electron correlation and phonon-scattering effect, respectively. The term $DT^{\frac{1}{2}}$ represents weak localization of the conduction electrons that can take place at very low temperature and represents the phenomenon of backscattering of charge carriers from the disorders present in the system [41]. The fitting carried out for the present data is shown in figure 5.3 and coefficients of the fit are listed in Table 5.2.

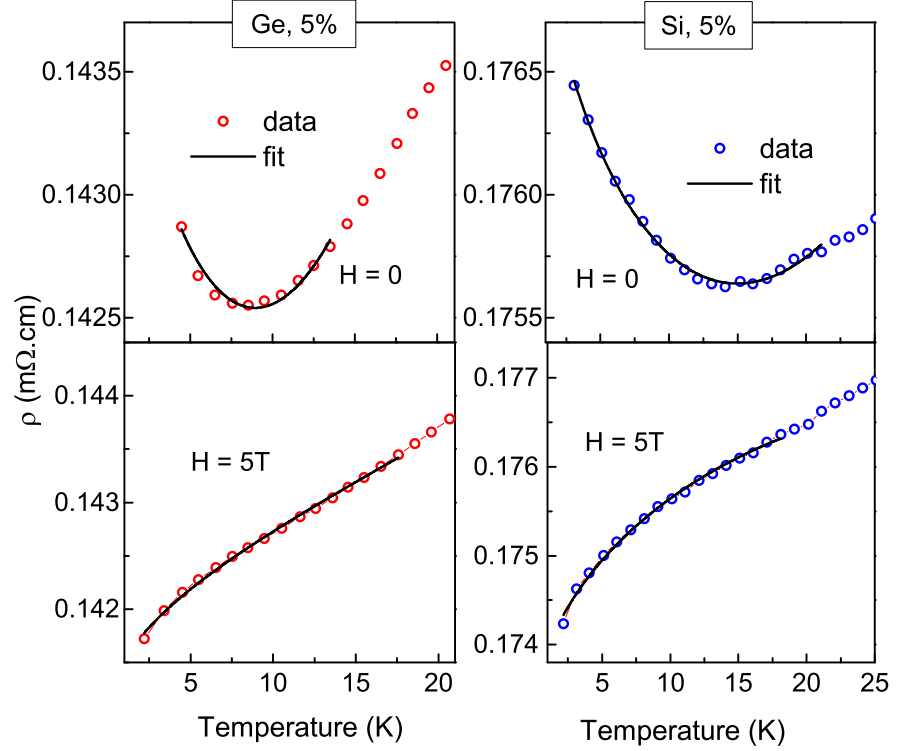


Figure 5.3: Low temperature region of resistivity data for $\text{Fe}_2\text{TiSn}_{0.95}\text{M}_{0.05}$ ($\text{M} = \text{Si}, \text{Ge}$), fitted with the equation given in the text. Bottom panels represent the data recorded with the application of constant magnetic field of 5 T.

With respect to pristine Fe_2TiSn , the Si- and Ge- substituted compositions show a decrease not only in the value of D , but B as well. The fall in the value of D implies a decrease in weak localization of carriers, and appears to be contrary to the expectation of rise

of static disorder in Fe_2TiSn upon substitution. Moreover, decrease in B implies a decrease in spin fluctuations present in Fe_2TiSn as have been discussed in chapter 3.3. Combining the two observation the possible scenario that emerges is that of generation of magnetic order in these system, reducing the scattering of charge carriers.

Table 5.2: Electrical resistivity fitting parameters obtained for the prepared compositions.

Chemical composition	Applied Field	fitting parameters		
		$B \times 10^{-9}$	$D \times 10^{-6}$	$C \times 10^{-14}$
Fe_2TiSn	H = 0T	21.939	16.918	8.417
	H = 5T	- 0.496	0.646	4.959
Ge, 5%	H = 0T	9.458	1.012	1.065
	H = 5T	-1.056	0.636	1.944
Si, 5%	H = 0T	2.992	0.649	0.917
	H = 0T	-0.332	-0.973	0.229

Consequently, B as well as D , should be sensitive towards application of an external magnetic field that will quench the Fermi-liquid-like states causing a decrease in spin fluctuation and destroy the weak localization. Hence $\rho(T)$ was measured under the application of 5 T magnetic field and the corresponding data, fitted using the same equation as above is shown in the lower panel of figure 5.2. As can be seen from the figure as well as the parameters listed in Table 5.2, application of magnetic field indeed decreases B and D . In other words, Si- and Ge- substitution leads to development of magnetic correlations in an otherwise non-magnetic Fe_2TiSn . Sb-substituted compositions, on the other hand, show negative temperature co-efficient of resistivity (figure 5.2(b)), a manifestation of its half-metallic character. An in-depth analysis of the resistivity can be found in chapter 3.3. In here, it suffices to know that the conduction in Sb-substituted compositions occur only through one spin channel and a pseudo-gap develops at Fermi-level for the oppositely oriented spin channel, thus giving rise to a highly polarized density of states.

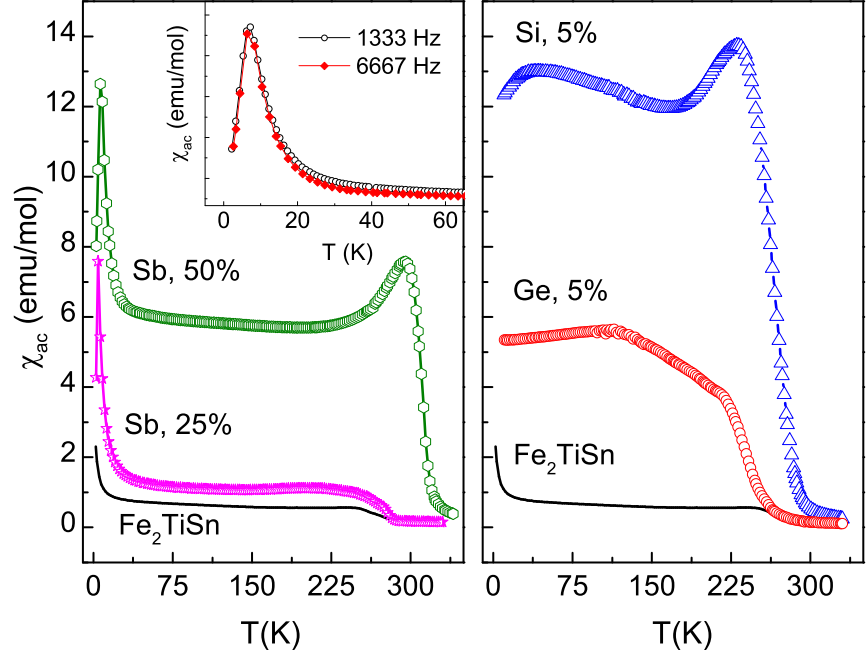


Figure 5.4: χ_{ac} recorded as a function of temperature for $\text{Fe}_2\text{TiSn}_{1-x}\text{Sb}_x$ (left panel) and $\text{Fe}_2\text{TiSn}_{0.95}\text{M}_{0.05}$ ($\text{M} = \text{Si, Ge}$) (right panel). The frequency dependence of peak-like feature at the blocking temperature is shown in the inset.

5.2.3 Magnetic measurement

At this point, it is desirable to investigate the magnetic properties of the Si-, Ge- substituted compositions and contrast the observations with that of Fe_2TiSn and the half metallic, $\text{Fe}_2\text{TiSn}_{1-x}\text{Sb}_x$ compositions. AC susceptibility (χ_{ac}) was hence measured in the temperature range 5 – 330 K to check for any magnetic transition, and resultant plots are shown in figure 5.4. Fe_2TiSn displays a sharp upturn at low temperature signalling a superparamagnetic-like evolution of small magnetic clusters. The magnetic clusters start forming at high temperature (between $\sim 250 - 290$ K) due to the inherent tendency of anti-site disorder between Fe and Ti atoms. Replacement of mere 5% of Sn by Si- causes a dramatic rise in $\chi_{ac}(T)$, indicative of a ferromagnetic-like transition taking place in the vicinity of room temperature. Similar trend is observed for Ge-substituted composition, and thus confirms the decrease in

the overall resistivity and B & D coefficients to be due to magnetic ordering of both these compositions. Further, as compared to 5% Si (or Ge), it takes 50% of Sn atoms to be replaced by Sb in $\text{Fe}_2\text{TiSn}_{1-x}\text{Sb}_x$ to attain the similar ordering temperature, as can be seen from the left hand panel of figure 5.4. Besides, the rise in ordering temperature in all the substituted compositions is an indication of increase in the strength of magnetic interaction. Unfortunately, instrumental limitation does not permit measurements beyond ~ 330 K, hence a truly paramagnetic region could not be accessed in these compositions.

In addition, the Sb-substituted compositions show a sharp peak-like feature in the low temperature region of χ_{ac} . With rising Sb-content, this peak shifts towards the higher temperature and grows in intensity. This low temperature feature is akin to the blocking temperature found in super-paramagnets, where the magnetic clusters that have grown large enough to possess substantial barrier energy do not get re-oriented or flipped when the system temperature is decreased. Subsequently, $\chi_{ac}(T)$ recorded using input signals with different frequencies (see inset to figure 5.4) does not show any shift in the peak position with changing frequencies, ruling out any relaxation dynamics of the magnetic clusters. It also points out that the origin of the magnetic order in Sb-substituted compositions should lie elsewhere, and not the anti-site disorder like in Fe_2TiSn .

Hence, to gain more insight into the magnetic behaviour of these compositions, magnetization recorded as a function of applied field ($M(H)$) at a constant temperature of 10 K is depicted in figure 5.5. A rapid increase in magnetization is observed at low field values followed by near-saturation in high field (5 T) region for Si- and Ge- substituted compositions. In comparison, Fe_2TiSn and Sb-substituted compositions show a slower rise of magnetization at low field, and does not saturate even with field as high as 5 T.

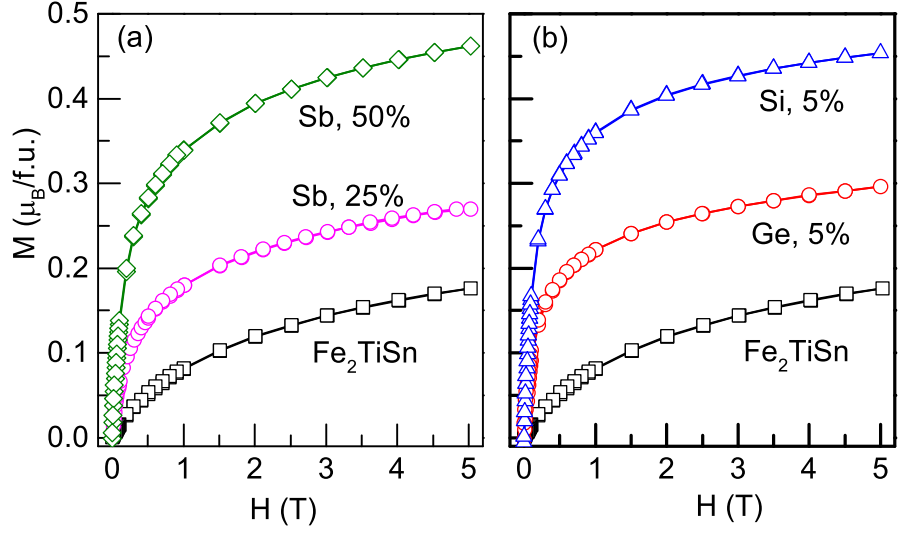


Figure 5.5: M-H curves recorded at 10 K for all the studied compositions.

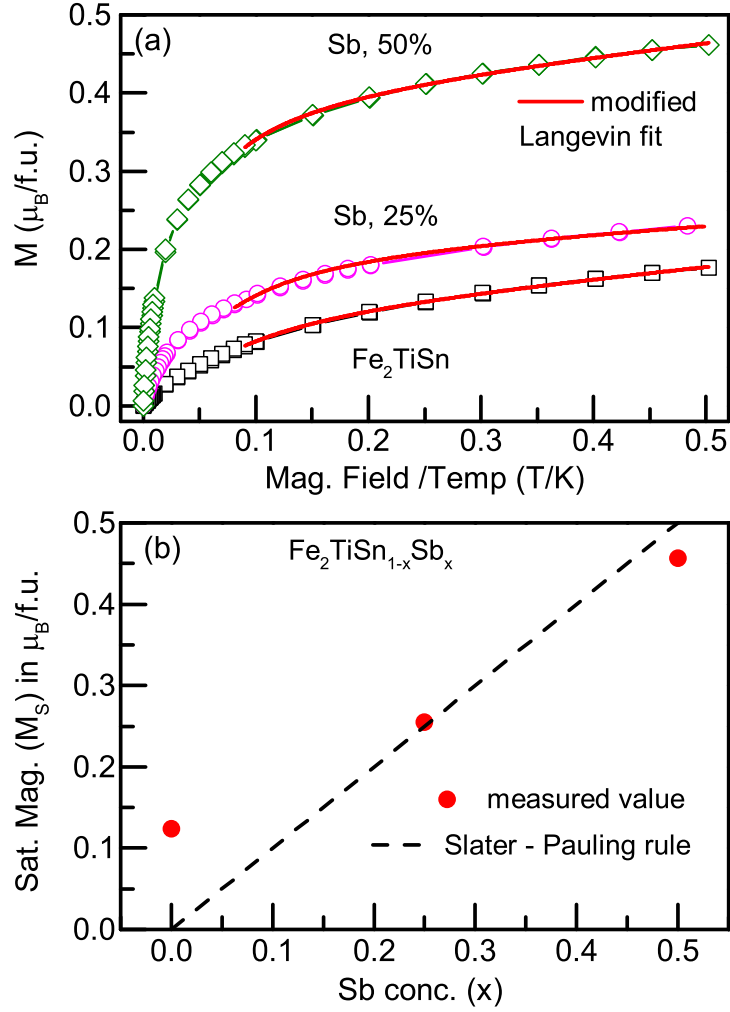


Figure 5.6: (a) M vs. H/T fitted using modified Langevin's function and (b) measured values of saturation magnetization (M_S) plotted along with the Slater-Pauling empirical rule (dotted line) for the Sb-substituted compositions.

The saturation magnetization (M_S) estimated by extrapolating the $M(H)$ curve towards $H \rightarrow 0$ are presented in Table 5.3. The overall magnitude of M_S though quite low, is almost double the value of Fe_2TiSn . Additionally, the $M(H)$ data for Sb-substituted compositions fits the modified Langevin function that includes superparamagnetic and magnetic contribution, as shown in figure 5.6(a). The modified Langevin function is represented as $M(H) = M_S [\coth(\alpha) - \frac{1}{\alpha}] + \chi H$ with $\alpha = \frac{\mu H}{k_B T}$, where μ is the average magnetic moment of the magnetic clusters, M_S is the saturation magnetization and χH represents the paramagnetic contribution. The extracted magnetic moment per cluster are summarized in Table 5.3; μ increases sharply with rising Sb-content.

Next, in congruence with its half-metallic character the M_S for Sb-substituted compositions follow the Slater – Pauling trend [26], as depicted in figure 5.6(b). In the Slater – Pauling empirical rule, the saturation magnetization is given as, $M_S = \text{valence electron number} - 24$, where the valence electrons are qualitatively estimated from the stoichiometry of the respective compositions. On the other hand, M_S values for Si- and Ge- compositions are relatively high and do not lie close to the Slater-Pauling line. This is perplexing since Si or Ge belong to the same group as Sn in the periodic table, and hence the number of valence electrons do not change in these compositions. Yet, these two compositions have M_S values matching with the Sb-based compositions.

Table 5.3: Magnetic moment values measured from $M(H)$ data (M_{exp}), calculated using DFT (M_{cal}), and estimated by from modified Lagrangian fit ($M_{cluster}$), for the present compositions.

	M_{exp} $\mu_B/\text{f.u}$	Total	Fe	M_{cal} Ti	Sn	Sb	$M_{cluster}$ μ_B
Fe_2TiSn	0.124	0	0.002	-0.0006	0	0	32.45
Sb, 25%	0.255	0.295	0.364	-0.063	-0.006	-0.004	41.53
Sb, 50%	0.457	0.547	0.708	-0.117	-0.011	-0.008	75.91
Ge, 5%	0.235						
Si, 5%	0.487						

5.2.4 Local structure measurements

Having observed the contrasts in the magnetic properties of Fe_2TiSn and $\text{Fe}_2\text{TiSn}_{1-x}\text{Z}_x$ ($\text{Z} = \text{Si}, \text{Ge}, \text{Sb}$), it becomes pertinent to determine the origin of the magnetic interactions in the later. It certainly cannot originate from a smaller effect like anti-site disorder found in Fe_2TiSn . In general, magnetic order in Heusler alloys is established via *RKKY* interaction between transition metals, mediated by the conduction electrons and hence depends on the distance between the interacting magnetic ions [38]. Extended X-ray absorption fine structure (EXAFS) spectroscopy, which is a reliable tool to determine any change in the local crystal structure, has been proven highly efficient in study of magnetic interactions in many other Heusler alloys [44, 68]. We carried out the study of local crystal structure of the present compositions using EXAFS measured at Fe *K* edge. The Sb-substituted samples have a distinctive change in lattice parameters as compared to Fe_2TiSn , hence EXAFS recorded using lab source X-rays are sufficient to provide vital information.

In the case of 5% Si- and Ge- substituted compositions there is hardly any change in the lattice parameters. To bring forth any local crystal structural changes, a high intensity and high resolution X-ray source is necessary. Thus EXAFS was recorded using the synchrotron X-ray source for these two compounds. The absorption co-efficient $\chi(k)$, which is the measure of raw spectral data recorded for all the compositions, is shown in the figure 5.7.

The atomic arrangements in the L2_1 full Heusler Fe_2TiSn structure is such that 4 Sn and 4 Ti atoms are equidistant ($\sim 2.6 \text{ \AA}$) from the absorbing atom, Fe. The next coordination shell consists of 6 Fe atoms at a distance of $\sim 3 \text{ \AA}$. Thus the Fe–Ti, Fe–Sn and Fe–Fe correlations that form the direct single-scattering paths for the absorbed X-rays, were used in the structural model to fit the EXAFS data. The raw spectra from figure 5.7 have been Fourier transformed

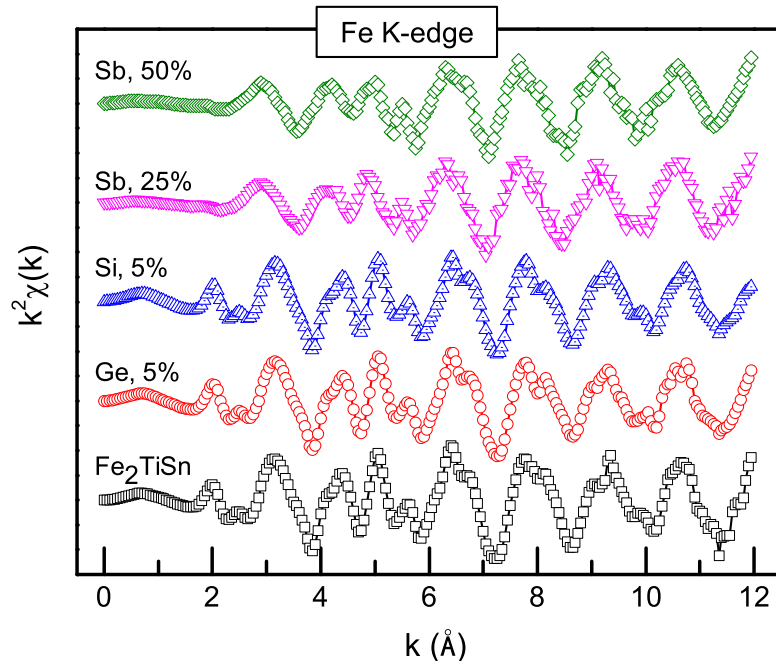


Figure 5.7: k^2 weighted raw Fe K-edge EXAFS spectra for all the present compositions.

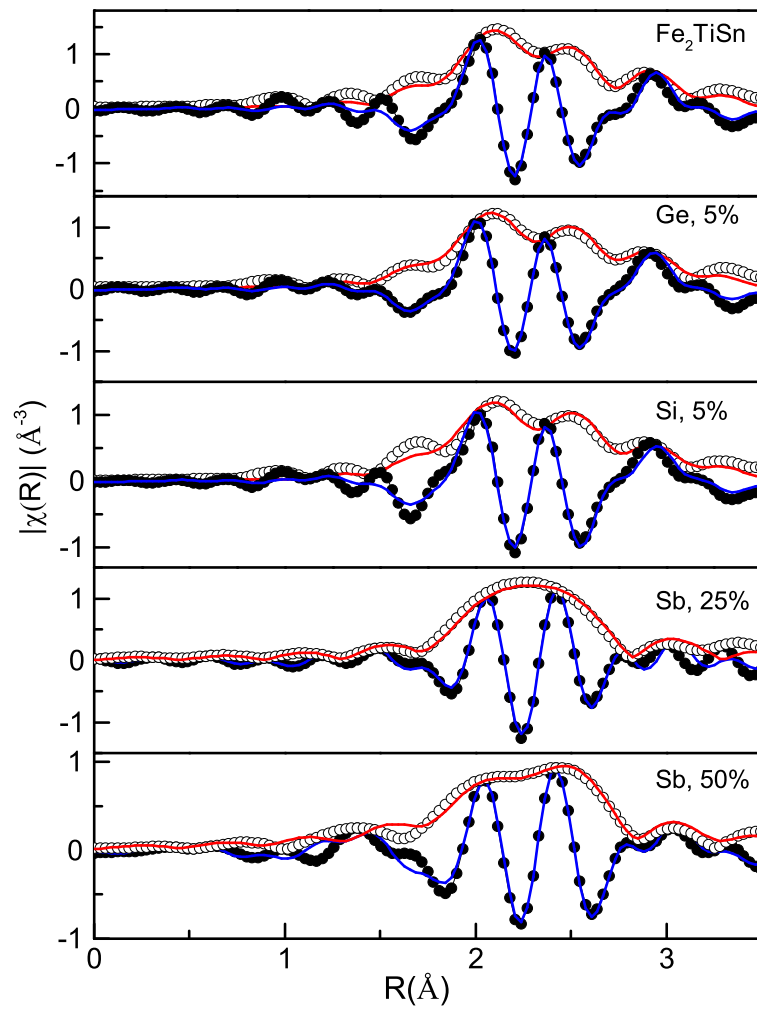


Figure 5.8: Fe K-edge EXAFS spectra fitted in real and k space for all the compositions investigated here.

into R -space such that $\chi(R)$ appears as a function of real distance from center of the absorbing atom. The data in k -range of 2–12 \AA^{-1} was used for this purpose. The background reduction, Fourier transforms and fitting of the crystal structural model to the data was carried out using the DEMETER software package [72]. Keeping the respective coordination number fixed, the bond distance and thermal mean square factor(σ^2) of each of the single-scattering paths were refined until a good fit was achieved in both, real and reciprocal space, shown in figure 5.8. Owing to the fact that Si and Ge substitution is limited to 5%, and the X-ray scattering potentials of Sn and Sb are similar, same fitting strategy as used for Fe_2TiSn was adopted for the substituted compositions.

Table 5.4: Bond distances, thermal mean square variation (σ^2), coordination number (CN), extracted from EXAFS data fitting.

	Bond	CN	R (\AA)	σ^2 (\AA^2)
Fe_2TiSn	Fe–Sn	4	2.6290(40)	0.0062(5)
	Fe–Ti	4	2.5834(69)	0.0115(11)
	Fe–Fe	6	3.0497(102)	0.0153(16)
Ge, 5%	Fe–Sn/Ge	4	2.6231(56)	0.0071(5)
	Fe–Ti	4	2.5813 (77)	0.0129(12)
	Fe–Fe	6	3.0261 (113)	0.0168(17)
Si, 5%	Fe–Sn/Si	4	2.6236(56)	0.0076(7)
	Fe–Ti	4	2.5790(89)	0.0127(15)
	Fe–Fe	6	3.0295(137)	0.0164(19)
Sb, 25%	Fe–Sn/Sb	4	2.6306(49)	0.0084(7)
	Fe–Ti	4	2.5617(68)	0.0142(11)
	Fe–Fe	6	3.0422(143)	0.0208(23)
Sb, 50%	Fe–Sn/Sb	4	2.6225(47)	0.0081(6)
	Fe–Ti	4	2.5552(74)	0.0147(12)
	Fe–Fe	6	3.0257(173)	0.0236(29)

The extracted bond distances and the σ^2 values are listed in Table 5.4. Comparing the values it is seen that the Fe–Ti bonds are consistently smaller than Fe–Sn bonds across all compositions. The stronger $d-d$ hybridization between Fe and Ti bands as compared to the $p-d$ hybridization between Fe and Sn is probably responsible for such an effect. Further, the Fe–Ti and Fe–Sn bond distances do not change after substitution at the Sn site, although

we observe a contraction of the unit cell from the XRD analysis of Sb-compositions. However, the corresponding σ^2 values of Fe–Ti bond is significantly high in all the substituted compositions, a manifestation of local structural disturbance within the unit cell due to the static chemical disorder caused by substitution.

The significant result of the EXAFS analysis is the shortened Fe–Fe distance observed in all the substituted compositions. In Fe_2TiSn , Fe–Fe bond length is 3.049\AA which decreases to 3.026\AA and 3.029\AA for 5% Ge- and Si-substituted samples, respectively. This change is surprising as no significant deviation from the unit cell parameters of Fe_2TiSn was observed upon 5% Si or Ge substitution. It is apparent that due to a large mismatch between the atomic sizes of the constituent Z atoms ($\text{Sn} > \text{Ge} > \text{Si}$), a lot of strain is generated within the unit cell to maintain the $L2_1$ cubic symmetry, which is released by shortening of the Fe–Fe bond. A similar decrease in Fe–Fe bond distance (3.025\AA) is observed when Sn is replaced by 50% Sb atoms. Since the atomic sizes of Sb and Sn are slightly different from each other, its unit cell has a larger tolerance towards substitution as compared to Si- or Ge- compositions. This conjecture also agrees with the fact that it is not possible to synthesize pure bulk forms of cubic Fe_2TiZ ($Z = \text{Si}, \text{Ge}, \text{Sb}$).

5.2.5 Theoretical calculations

Keeping in view the results of magnetization measurements and the fact that $L2_1$ full Heusler alloys are *RKKY* mediated magnetic systems, it is clear that the Fe–Fe interaction here play a vital role in controlling the magnetic ground state.

A decrease in the Fe–Fe bond length points to the fact that *RKKY* exchange is strengthened and so is the magnetic order in the substituted compositions of Fe_2TiSn . To further support our argument, the Heisenberg exchange parameter calculations are presented

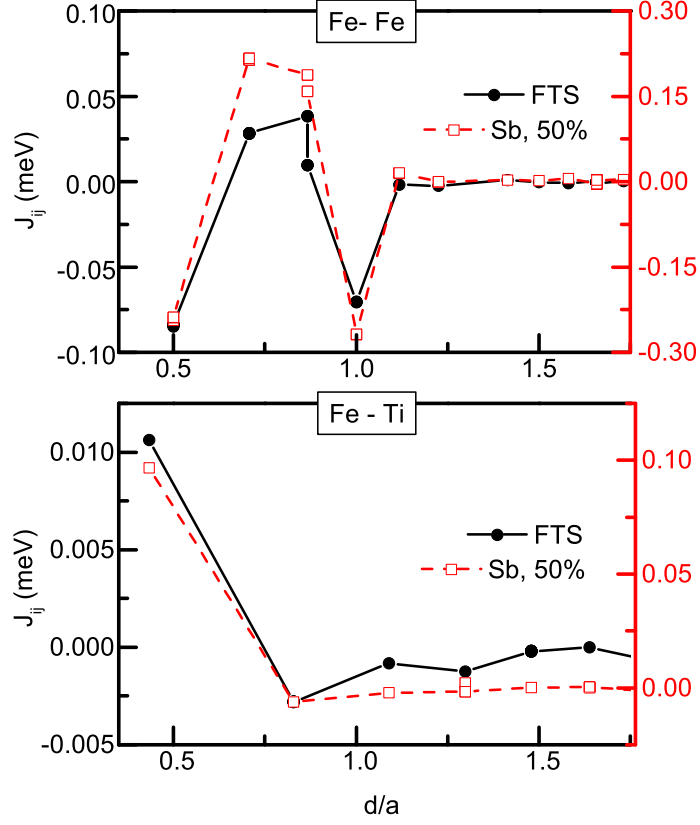


Figure 5.9: Heisenberg exchange coupling parameter, J_{ij} , plotted against Fe – Fe and Fe – Ti distance normalized to the lattice parameter, in Fe_2TiSn (solid line) and 50% Sb substituted (dotted line) composition (see text for details).

in figure 5.9 for pristine Fe_2TiSn and 50% Sb substituted composition. In accordance with the *RKKY* – type exchange, the Fe–Fe coupling energy (J_{ij}) is found to be oscillatory in nature, and its amplitude varies between -0.08 meV to 0.08 meV for Fe_2TiSn . These oscillations become way too strong in 50% Sb - substituted composition, with J_{ij} varying between -0.25 to 0.25 meV. The oscillatory nature of J_{ij} thus clarifies the *RKKY* nature of magnetism and significance of Fe–Fe exchange in influencing the magnetic ground state of these compositions. The total exchange coupling energy, $\sum J_{ij}$, taken over one unit cell yields a value of ~ 0.066 meV for 50% Sb substituted composition as against ~ 0.003 meV for pristine Fe_2TiSn , indicating a ferromagnetic ground state. From the figure 5.9, it is observed that the very first Fe–Fe interaction shell

at half the unit cell distance ($d/a = 0.5$), yields a negative value for J_{ij} , indicating anti-ferromagnetic nature of the exchange correlation.

However, it may be noted that the rest of the Fe–Fe interaction shells present at $0.5 < d/a < 1$ yield a positive J_{ij} value, thus driving the $\sum J_{ij}$ within one unit cell to a positive value. This fact also correlates with our $M(H)$ measurement, where the curves did not saturate even at high magnetic fields indicating presence of competing magnetic interactions.

To further complement our experimental findings, we calculate the site specific magnetic moments for $\text{Fe}_2\text{TiSn}_{1-x}\text{Sb}_x$ (with $x = 0, 0.25, 0.5$) using the spin polarized pseudopotential method. Clearly, the total magnetic moments (Table 5.3), increases with the Sb concentration, in congruence with experimental results. The atomic moment at Fe site which is mere $\sim 0.001\mu_B$ for Fe_2TiSn , increases to $\sim 0.7\mu_B$ for 50% Sb. The total and partial density of states (DOS, and $p\text{DOS}$) of pristine and 50% Sb-substituted compositions are shown in figure 5.10 and 5.11. In Fe_2TiSn the DOS is symmetrical in majority and minority spin bands and a small gap exists at the Fermi level (E_F). The energy region between -3 to 0 eV consists mainly of Fe and Ti $3d$ bands and a small contribution from Sn/Sb p states. The three main peaks near E_F are the bonding and anti-bonding states generated from the Fe–Fe hybridization and a small peak due to $p - d$ hybridization. With 50% Sn sites replaced by Sb, the symmetry between majority and minority spin band breaks down. E_F shifts towards higher energy side in majority spin band whereas it stays within the gap in the minority spin band. Ti $p\text{DOS}$ has a plateau like feature for a large energy range near E_F , which does not change with Sb-substitution. A slight increase in the small $p - d$ hybridization peak at E_F is due to the extra electron contributed by Sb.

So, the increased local moment at Fe site seen in the DOS cal-

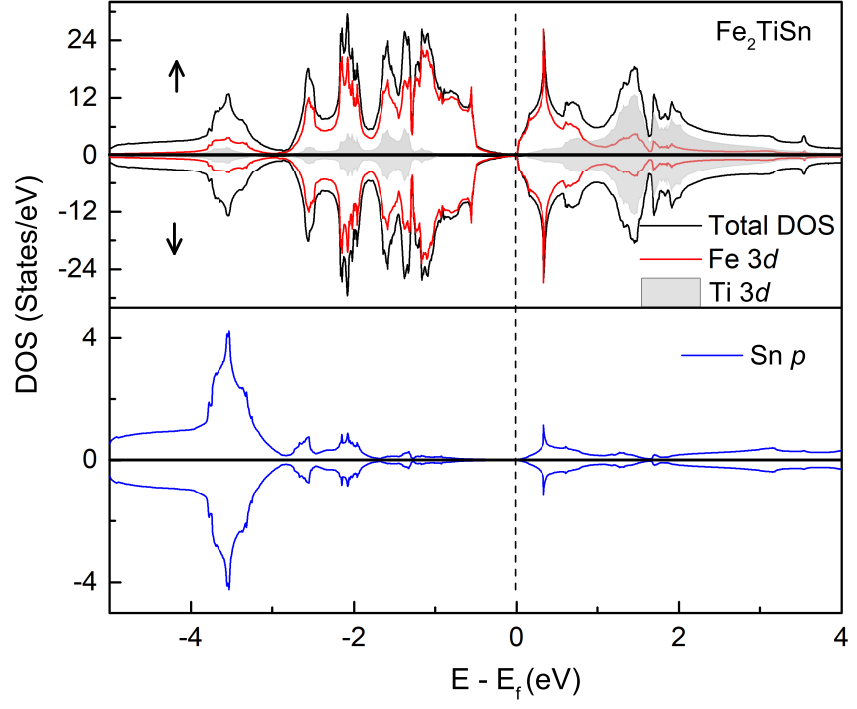


Figure 5.10: Spin projected total and partial DOS for pristine Fe_2TiSn . For clarity of the figure, partial DOS for Sn p -states is shown in the lower panel.

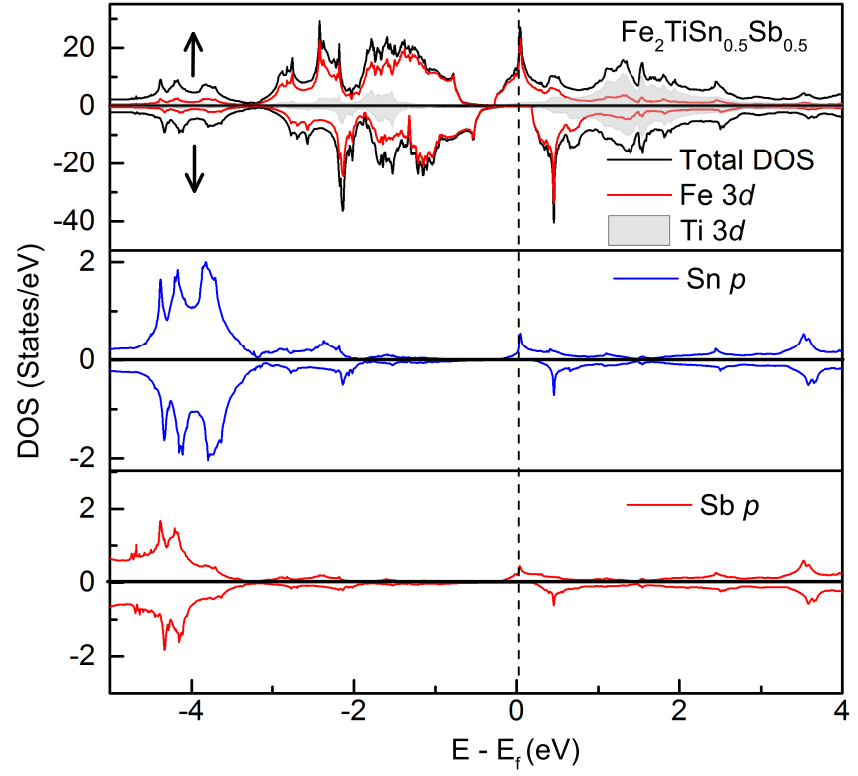


Figure 5.11: Spin projected total and partial DOS for 50% Sb substituted Fe_2TiSn . For clarity of the figure, partial DOS for Sn and Sb p -states is shown in the lower panels.

ulation is due to decrease in Fe–Fe bond distance obtained experimentally from EXAFS. The oscillatory nature of interaction characteristic of *RKKY* mediated exchange is confirmed from the Heisenberg exchange parameter calculations. Thus the magnetic order in cubic Heusler phase of $\text{Fe}_2\text{TiSn}_{1-x}\text{Z}_x$ ($\text{Z} = \text{Si}, \text{Ge}, \text{Sb}$) develops from the strengthening of $d-d$ hybridization, facilitated by the strain in the unit cell caused by chemical substitution.

5.3 Summary

In summary, we found that, pure L2_1 bulk polycrystalline form of $\text{Fe}_2\text{TiSn}_{1-x}\text{Z}_x$ ($\text{Z} = \text{Si}, \text{Ge}$) compositions can be obtained only for $x \leq 0.05$ for Si and Ge. In contrast to theoretical prediction of Fe_2TiGe , Fe_2TiSi to be semiconductors, the experimental results indicate highly reduced electrical resistivity in mere 5% Si and Ge - substituted Fe_2TiSn . This change in resistivity is due to the decrease in scattering of charge carriers upon development of long range magnetic order in these compositions, as seen from our magnetic properties measurements. From EXAFS analysis, and exchange coupling parameter calculation it is seen that the origin of magnetic order lies in the *RKKY* mediated exchange interaction between shortened Fe–Fe bonds. An increased local structure distortion within the cubic symmetry is brought about by the partial replacement of Sn atoms with atoms having different atomic sizes, thus leading to decrease in Fe–Fe bond distance. The spin-projected DOS calculations complement the experimental findings wherein a buildup of a localized moment at Fe site is seen in the substituted compositions is due to the stronger $d-d$ hybridization and responsible for magnetic ground state in Sb-substituted Fe_2TiSn compounds.

Chapter 6

Half-metallicity in Cr substituted Fe_2TiSn

6.1 Preamble

In chapter 4.3 we have shown that substituting Sb at Sn site in Fe_2TiSn can give rise to half metallic ground state with enhanced Curie temperature and magnetic properties. So it would be interesting to see if the system can be driven to half-metallic ground state with the Y site substitution. Consequently the compounds with $\text{Fe}_2\text{Ti}_{1-x}\text{Cr}_x\text{Sn}$ was prepared from small values of x . We find that above 25% substitution of Cr gives rise to un-reacted Cr phase in the compositions. Hence our experiments are restricted to a maximum of 25% Cr substituted Fe_2TiSn compositions.

In this final work of this thesis, we report detailed magnetic and electronic properties of the prepared compositions. Based on the experiments, it was realized that competing AFM and FM interactions develop in the non-magnetic Fe_2TiSn with the substitution of small amount of Cr. With the increase in Cr concentration, a gradual transition to FM phase is observed. Calculated DOS and Heisenberg exchange parameters help to understand the mechanism behind the transition in magnetic ground state. More interestingly, a true half metallic ground state is found in 25% Cr substituted composition, evident from its transport and magnetic measurement result. The calculated DOS supports the experimental results.

Table 6.1: Lattice parameter and goodness of fit parameters for Rietveld refinement of XRD profiles.

Cr conc. (%)	Lattice Parameter Å	R_{Bragg}	χ^2
0	6.0654(3)	2.42	2.51
10	6.0612(1)	2.18	2.16
17	6.0585(1)	1.39	3.7
25	6.0541(2)	2.3	5.3

6.2 Results and Discussion

6.2.1 X ray diffraction

Room temperature X ray diffraction profiles of all the prepared compositions of $\text{Fe}_2\text{Ti}_{1-x}\text{Cr}_x\text{Sn}$ series are shown in figure 6.1. The presence of strong reflection from (111), (200), (220) planes confirms the expected L2_1 structure with $F\bar{m}3m$ space group have formed. The obtained profiles were analyzed using Rietveld refinement method as implemented in FullProf suite [75]. No extra peak except the ones from the L2_1 structure are seen as evident from the figure 6.1. Extracted lattice parameters from the refinement are summarized in table 6.1.

As shown in figure 6.2, lattice parameter decreases linearly with the increase in Cr concentration, since Cr have a slightly smaller atomic radius compared to Ti. The decrease in lattice parameter indicates, Cr occupies the Ti site as intended.

On close observation it can be observed that intensity of the (200) peak increases monotonously with the increase in Cr concentration. Further, $\frac{I_{200}}{I_{220}}$ calculated for all the prepared compositions are plotted in the right axis of figure 6.2. The intensity ratios seem to increase with the increase in Cr concentration, indicating a decrease in anti-site disorder from the pristine Fe_2TiSn after substitution of Cr.

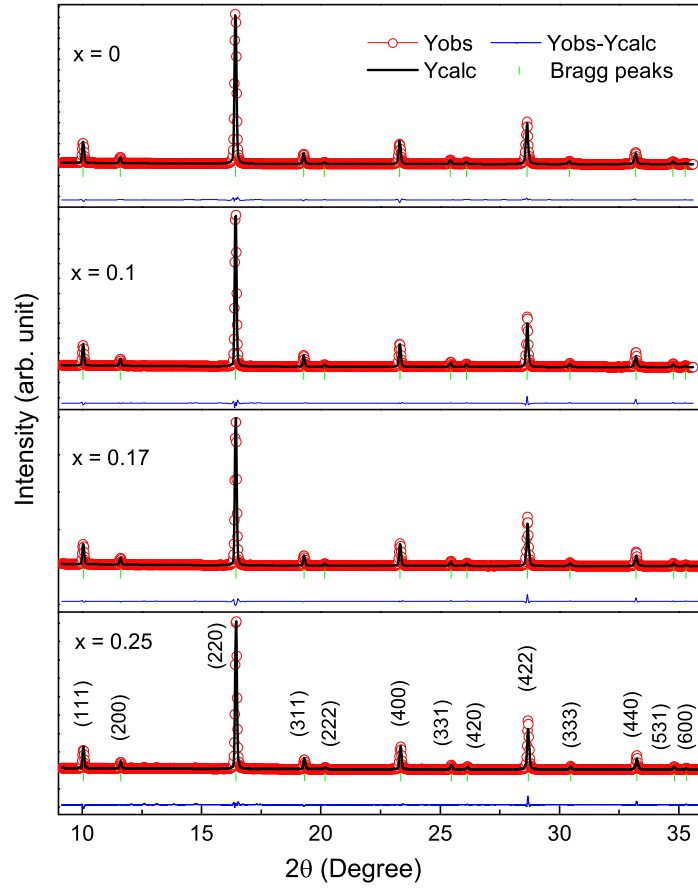


Figure 6.1: X ray diffraction pattern for $\text{Fe}_2\text{Ti}_{1-x}\text{Cr}_x\text{Sn}$ composition recorded using synchrotron based source. Rietveld refinement of the XRD pattern for all compositions are also shown.

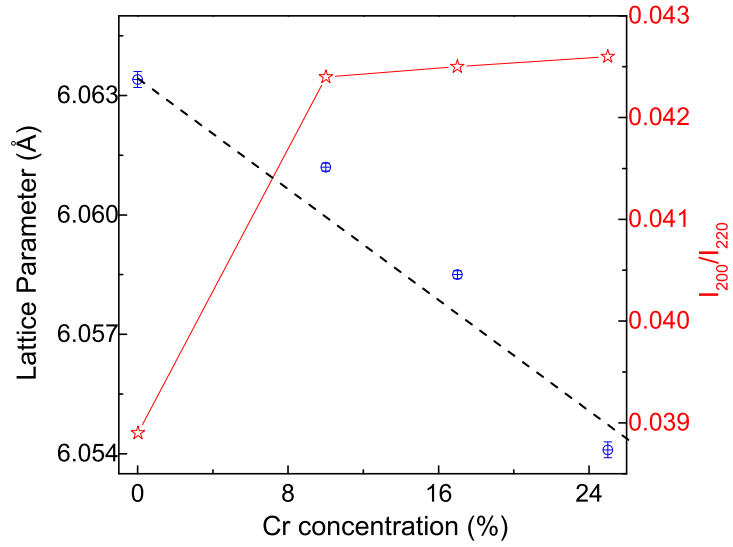


Figure 6.2: Change in lattice parameter and intensity ratio of $\frac{I_{200}}{I_{220}}$ with concentration of Cr.

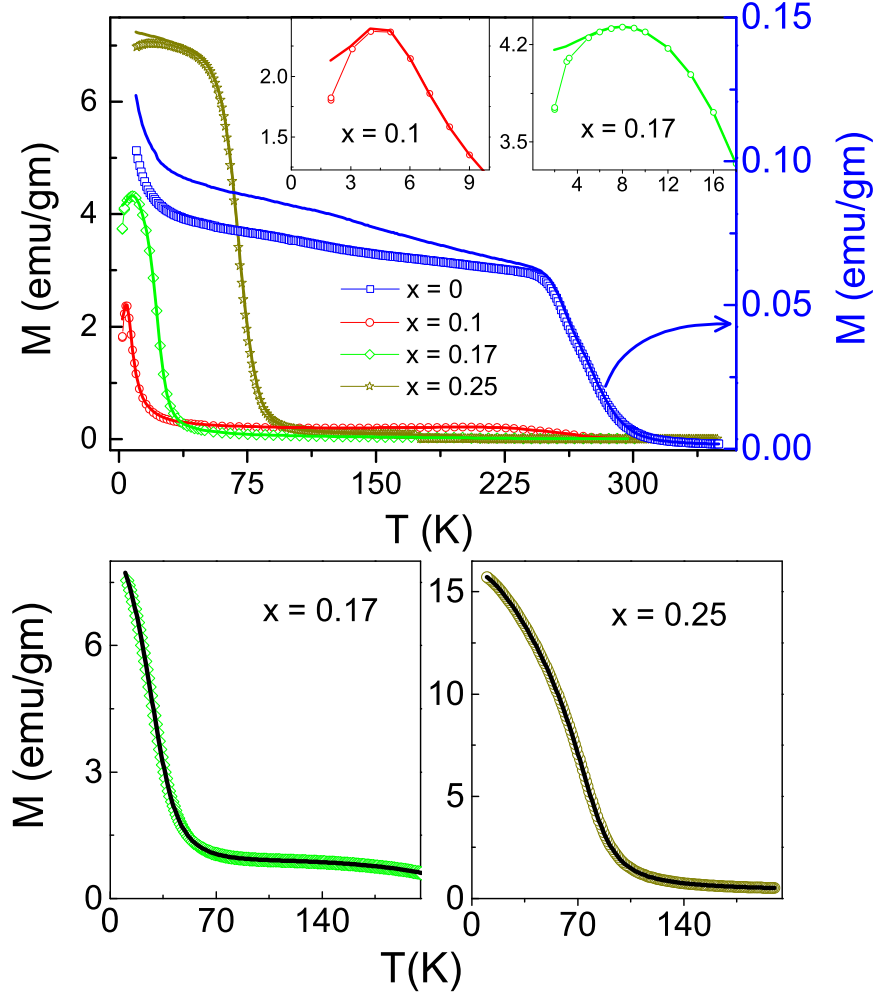


Figure 6.3: (Main Panel) Zero field cooling curve as a function of temperature measured for all prepared composition. (Insets) ZFC and FC curves for (upper) $x = 0$ and (lower) $x = 0.25$ compositions to highlight the bifurcation.

6.2.2 Magnetic properties

Temperature dependence of Magnetism

To understand the magnetic ground of the samples, magnetization as a function of temperature is measured. Temperature variation of magnetization for the $\text{Fe}_2\text{Ti}_{1-x}\text{Cr}_x\text{Sn}$ compositions, measured in zero field cooled (ZFC) and field cooled (FC) protocol, and with the application of 100 Oe. magnetic field are shown in figure 6.3.

The upturn present in $M(T)$ of Fe_2TiSn has been identified as a result of superparamagnetic ordering of magnetic clusters in

chapter 3.3. After substitution of Cr in the composition, a peak like feature starts to appear at low temperature, which shifts to higher temperature with the increases in Cr concentration. A peak in the magnetization can indicate a superparamagnetic blocking temperature, cluster or spin glass phase or an antiferromagnetic (AFM) ordering in the composition. From the magnetization isotherms, an evolution of magnetic ordering has been seen. So, the peak feature probably indicate an AFM ordering in the composition rather than any cluster formation.

Further, Fe_2TiSn have a huge bifurcation between ZFC and FC starting from higher temperature. During ZFC cycle the magnetic clusters in this composition freezes randomly and does not contribute collectively to the net magnetization, but during FC cycle the applied magnetic field try to orient the clusters in the field direction and contribute higher to the total magnetization. In the Cr substituted composition also a small bifurcation between ZFC and FC, below the peak is present, as can be seen from the inset of figure 6.3. The bifurcation further confirms the presence of AFM ordering in these compositions. As shown in the lower panel of figure 6.3, higher field of only 0.1 T can destroy the bifurcation. The small bifurcation and destruction of it with the application of only 0.1 T field indicates the weak nature of AFM ordering in these compositions.

On the other hand, with the increase in Cr concentration the AFM peak widthg increase and in case of 25% Cr substituted composition instead of a peak, magnetization almost saturates below the magnetic ordering temperature. Saturation of M below magnetic transition is a signature of ferromagnetic ordering. So, from here it can be safely concluded that, Inclusion of Cr in the Fe_2TiSn system, gives rise to AFM ordering for small concentration of Cr substitution. With the increase in Cr concentration, the FM ordering in the system becomes dominating.

Magnetic ac susceptibility

Further, magnetic ac susceptibility(χ_{ac}) as a function of temperature was measured for all prepared compositions in the range of 2K to 340K. Figure 6.4 shows the real part of χ_{ac} measured in 0 ac field and frequency ~ 9.9 kHz. The χ_{ac} exhibits a sharp upturn in case of Fe_2TiSn , which has been identified as a result of superparamagnetic ordering of non-interacting magnetic clusters. After only 10% substitution of Cr, a sharp peak like feature appears in the low temperature of χ_{ac} . This feature shifts towards higher temperature as the Cr concentration in the composition increases.

Measurement of χ_{ac} can probe the dynamics of the spin system at a time scale decided by the measuring frequency. Since the above mentioned possibilities act differently with the measuring frequency, lower temperature part of the χ_{ac} was measured at different frequency range as shown in Figure. 6.5. The shift in peak position with the change in frequency is very small. Frequency dependence of χ_{ac} can quantified from the value of Φ as, $\Phi = \frac{\Delta T_B}{T_B \Delta \log(f)}$. The extracted average values of Φ is summarized in Table 6.2 and all values are in the range of 0.002 – 0.0001. In superparamagnetic ordering the Φ values comes in the range of 0.1 – 0.3, where as in case of cluster-glass, spin – glass or interacting cluster the value of Φ stays in the range 0.02 – 0.005 [17, 29, 39]. So the value obtained in our case clearly indicates that the superparamagnetic clusters are not present in the Cr substituted compositions. Rather, the very small values of Φ indicates presence of antiferromagnetic ordering in these samples along with small amount of magnetically interacting clusters.

The magnetic transition temperature(T_N) have been estimated from the local maxima in $\frac{d\chi}{dT}$ vs T graph and are summarized in table 6.2. T_N increases with the increase in Cr concentration, signifies the strengthening of magnetic ordering after substitution

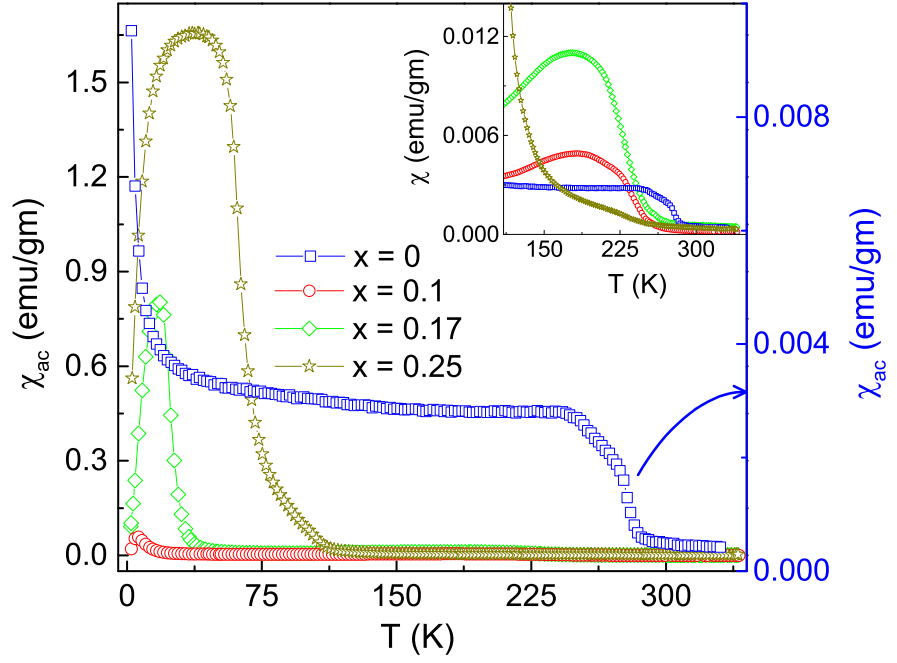


Figure 6.4: χ_{ac} as a function of temperature for $\text{Fe}_2\text{Ti}_{1-x}\text{Cr}_x\text{Sn}$ series.

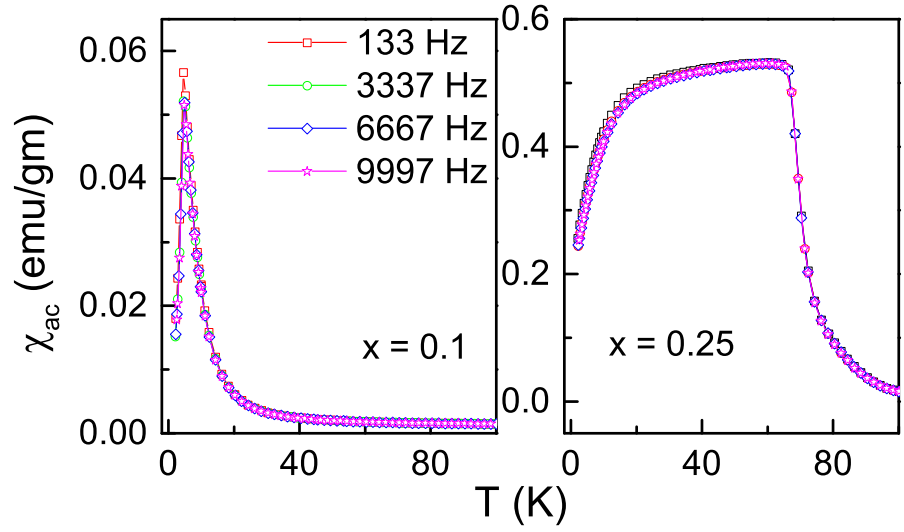


Figure 6.5: Inverse magnetic susceptibility as a function of temperature for $\text{Fe}_2\text{Ti}_{1-x}\text{Cr}_x\text{Sn}$ series.

of Cr.

A step like feature is observed near room temperature in case of parent composition Fe_2TiSn , which has been identified as the onset of ordering of magnetic clusters. The higher temperature region of χ_{ac} for all prepared composition has been shown in the inset of figure 6.4. Clearly the ordering temperature shifts to lower temperature side, as the concentration of Cr increases in the system, which might indicate the weakening of the contribution from clusters in the total magnetization. In case of 25% Cr substituted composition the high temperature feature is not present.

The inverse χ_{ac} does not follow a Curie-Weiss law within the temperature range of our measurement, implying a true paramagnetic state is not achieved even after the magnetic transition. Although a linear region is achieved above room temperature, but the value of χ_{ac} increases abruptly below the temperature, deviating the χ_{ac}^{-1} from linearity. This anomaly have been observed in many other systems having magnetic clusters present [47]. The ordering temperature of magnetic clusters(T_d) have been estimated by extrapolating the higher temperature linear region to $\chi_{ac}^{-1} = 0$ and are summarized in table 6.2. So from all the magnetic measurements it is clear that, after substitution of Cr in Fe_2TiSn the system first order antiferromagnetically. With the increase in Cr concentration the AFM ground of the system progressively orders ferromagnetically. On the other hand the magnetic clusters giving rise to weak magnetism in the Fe_2TiSn , decreases drastically with the increase in Cr concentration.

Field dependence of magnetization

First, to understand the magnetic ground states of the prepared compositions, isothermal magnetization($M(H)$) as function of applied field was recorded. Figure 6.7 depicts the magnetic isotherms

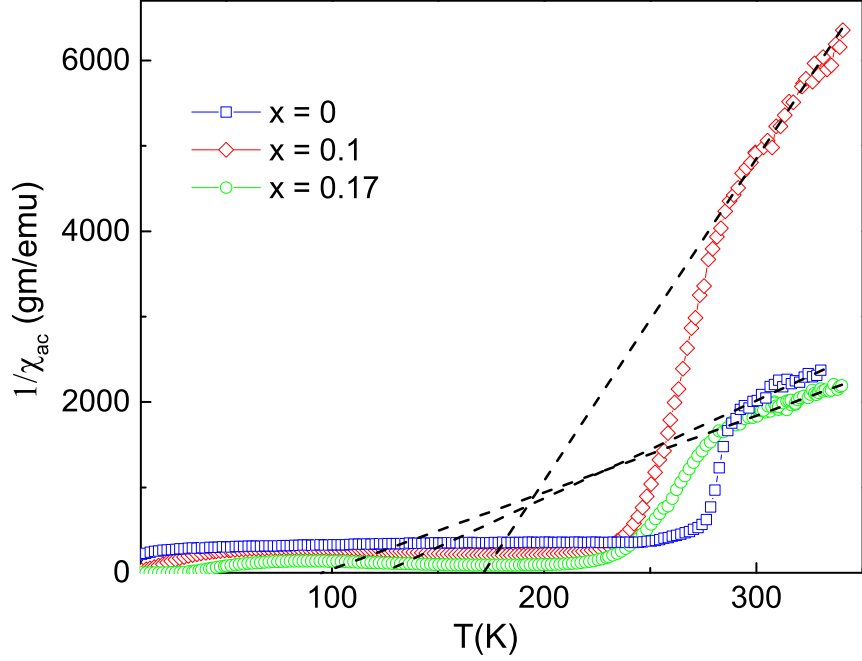


Figure 6.6: Inverse magnetic susceptibility as a function of temperature for $\text{Fe}_2\text{Ti}_{1-x}\text{Cr}_x\text{Sn}$ compositions. The solid line represents a guide to the eye to show the intersection at temperature axis.

Table 6.2: Fitting parameters for magnetization data.

Cr conc. (%)	Φ	T_N K	T_{cl} K	M_s μ_B	M_{sp} μ_B
0	—	—	90.1	0.104	
10	0.0241	6.0	164.8	0.203	0.184
17	0.0001	26.4	81.9	0.369	0.38
25	0.0007	66.7	98	0.698	0.699

measured at 2K. All the curves retraces itself with field change and no remnant magnetization and magnetic coercivity was found. All samples show non saturation of magnetic moment even at a high magnetic field of 5T. As the Cr concentration increases a slow approach towards saturation can be observed from the normalized magnetization plotted in the inset of figure 6.7(b).

Previously it has been shown that, magnetism in otherwise non-magnetic Fe_2TiSn is evolved due to the presence superparamagnetic clusters, which originates as a result of Fe/Ti anti-site disorder. Thus low temperature magnetization isotherms of Fe_2TiSn

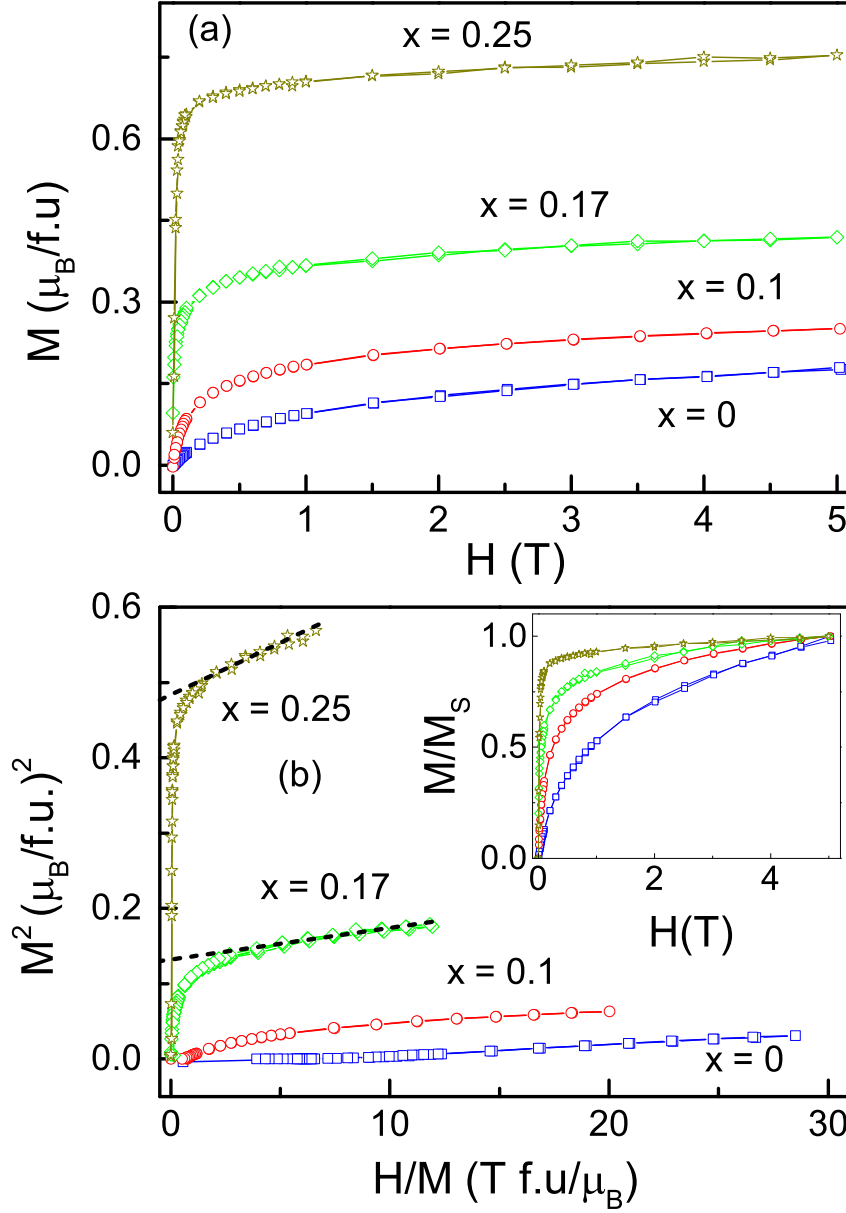


Figure 6.7: (Main Panel) Zero field cooling curve as a function of temperature measured for all prepared composition. (Insets) ZFC and FC curves for (upper) $x = 0$ and (lower) $x = 0.25$ compositions to highlight the bifurcation.

follows a modified Langevin's function given by, $M(H) = M_s L(\alpha) + \chi H$, taking superparamagnetic and paramagnetic contribution into consideration. It is found out that the Cr substituted compositions does not follow the superparamagnetic equation, which indicates the superparamagnetic clusters are not present in the Cr substituted composition. The non-saturating nature of the curves, thus

hints presence of antiferromagnetic ordering in the system.

Spontaneous magnetization(M_{sp}) of the compositions has been extracted from the Arrot plot shown in figure 6.7(b) (by extrapolating the linear part of the plot towards $H/M = 0$) and is tabulated in table 6.2. In case of Fe_2TiSn the linear part intercepts x axis, indicating a paramagnetic phase even at 2K. After substitution of 10% Cr at Ti site, a spontaneous moment of $0.19 \mu_M/\text{f.u.}$ is induced in the system. The positive values M_{sp} indicates that, with the inclusion of Cr, magnetic ordering develops in the system, rather than magnetic clusters. Further, the value of M_{sp} increases with the increase in Cr concentration, and finally reach $\sim 0.7 \mu_M/\text{f.u.}$ in case of 25% Cr substituted composition. The increase of M_{sp} signals the strengthening of magnetic ordering with the increase in Cr concentration in these composition.

6.2.3 Heat capacity Measurement

Further in order to prove the presence of magnetic cluster in the $\text{Fe}_2\text{Ti}_{1-x}\text{Cr}_x\text{Sn}$ compositions heat capacity was measured in the temperature range 2K - 300K and the results are shown in Figure 6.8. The absence of any peak near the magnetic transition indicate the weak nature of magnetism in these compositions.

In general the low temperature specific heat in metallic systems can be expressed as, $C(T) = \gamma T + \beta T^3$, where γ is Sommerfeld's coefficient and represents the electronic contribution, whereas β represents the phonon contribution to specific heat. The equation is valid roughly upto the temperature of $\Theta_D/50$, where Θ_D is the Debye temperature. A plot of C/T vs T^2 curve is expected to be linear at low temperature. But as shown in the inset of Figure 6.8 an upturn can be clearly visible in case of parent composition Fe_2TiSn . The upturn decreases with increasing Cr concentration in the composition.

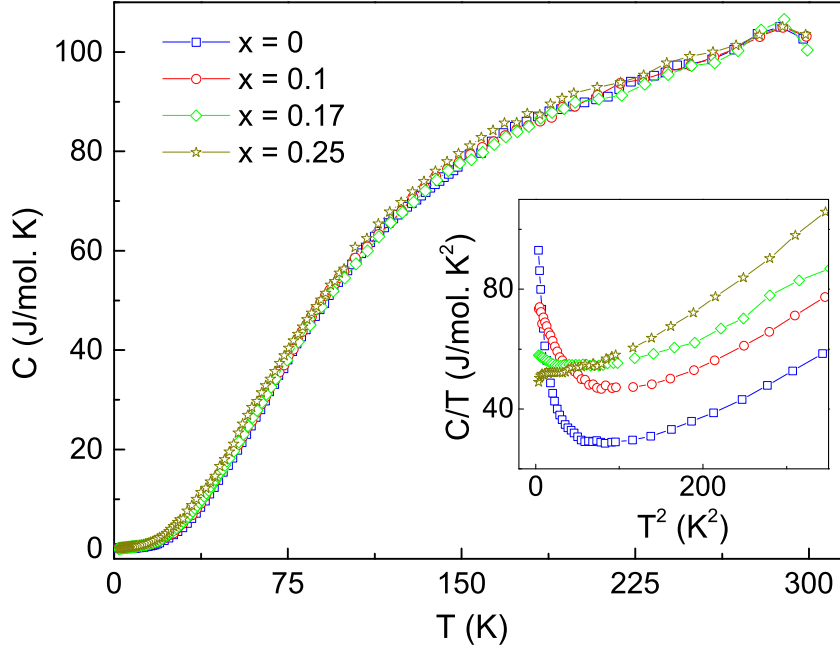


Figure 6.8: Specific heat as a function of temperature of $\text{Fe}_2\text{Ti}_{1-x}\text{Cr}_x\text{Sn}$ compositions. Inset (a) shows the low temperature upturn in C/T .

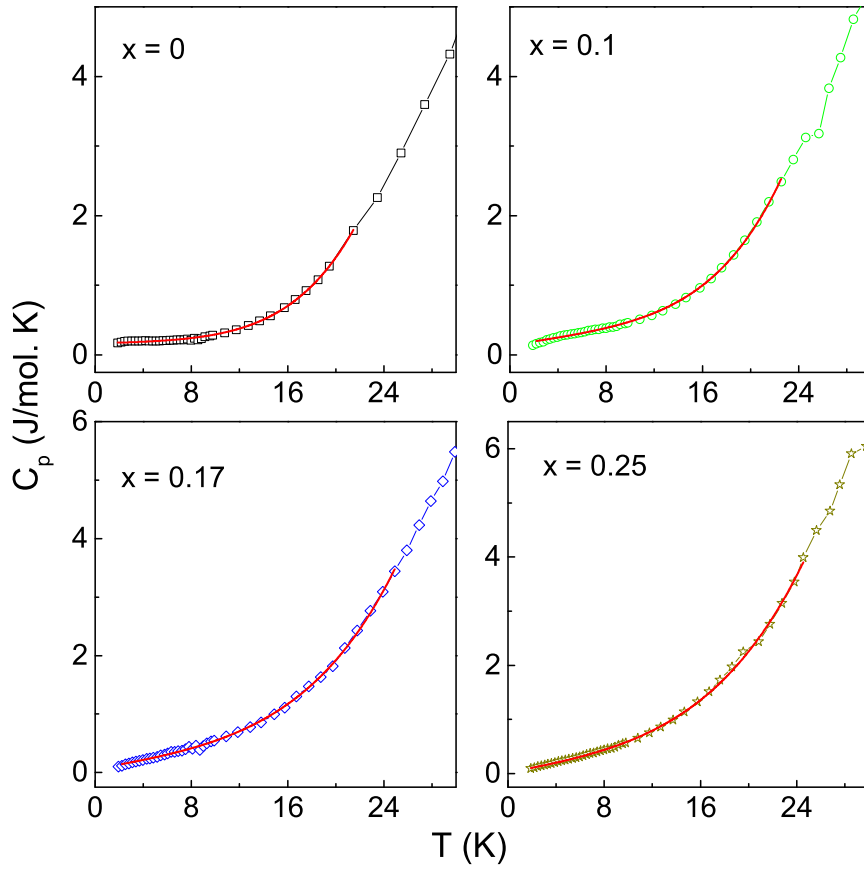


Figure 6.9: Low temperature heat capacity data fitted with the equation $C(T) = C_0 + \gamma T + \beta T^3 + \delta T^5$. The extracted parameters are summarized in Tab. 6.2.

The similar low temperature feature in C/T have also been found in other Heusler alloys like Fe_2VAl [66], Ru_2NbAl [52], where ferromagnetic clusters are present. The ferromagnetic clusters presents in the system rests at lowest energy at low temperature. When an external force like temperature or magnetic field try to alter the cluster magnetization vector, it's energy gets enhanced. This extra energy can be stored in the clusters through local crystal deformation of the clusters and magnetostriction energy.

So due to the thermal excitation the magnetic clusters present in the system oscillate along the direction determined by its magnetic anisotropy, and absorb $k_B T$ amount of thermal energy. This oscillation of the clusters give rise to an extra constant term $C_0 \sim 2k_B N$ in the total specific heat [66, 78], where N is the number of cluster present in the system. However, to fulfill the third law of thermodynamics the heat capacity at $T = 0$ should be 0. So the additional contribution starts gradually losing its strength below a certain temperature called Einstein temperature given by, $T_E = \frac{2\beta H}{k_B}$. T_E generally found to be at less than 1K. Considering the constant C_0 term in the equation for specific heat, the equation modifies to , $C(T) = C_0 + \gamma T + \beta T^3 + \delta T^5$. Since, Θ_D is unknown in our compositions, the δ term is added to take care of the extended temperature range beyond $\Theta_D/50$ [52]. The experimental data fits nicely to the equation in the temperature range 2k –25K as shown in Figure 6.8. The extracted parameters are summarized in table 6.3.

The number of cluster present in the system decreases drastically with the increase in Cr concentration, which is also estimated from the magnetization measurement results presented in the previous sections. However the value of Sommerfeld constant(γ) increases with the increase in Cr concentration. Decrease of magnetic clusters decreases the spin fluctuation in the system, which is supposed to decrease the value of γ . But on the other hand increase in magnetic ordering increase the electron correlation giving rise to

a higher value of γ . So the increase in the Sommerfeld constant value clearly indicates the dominating magnetic ordering in the Cr substituted composition.

Table 6.3: Heat capacity fitting parameters obtained for the prepared compositions.

Cr conc. %	C_0 mJ/ mol.K	γ mJ/mol.K ²	β mJ/mol.K ⁴	δ mJ/mol.K ⁶	N per mol
0	166.59	4.89	0.0598	2.05	1.21
10	141.06	26.59	0.549	1.997	1.02
17	58.51	37.91	0.0969	1.022	0.425
25	19.46	43.72	0.1306	0.9863	0.141

6.2.4 Local structure analysis

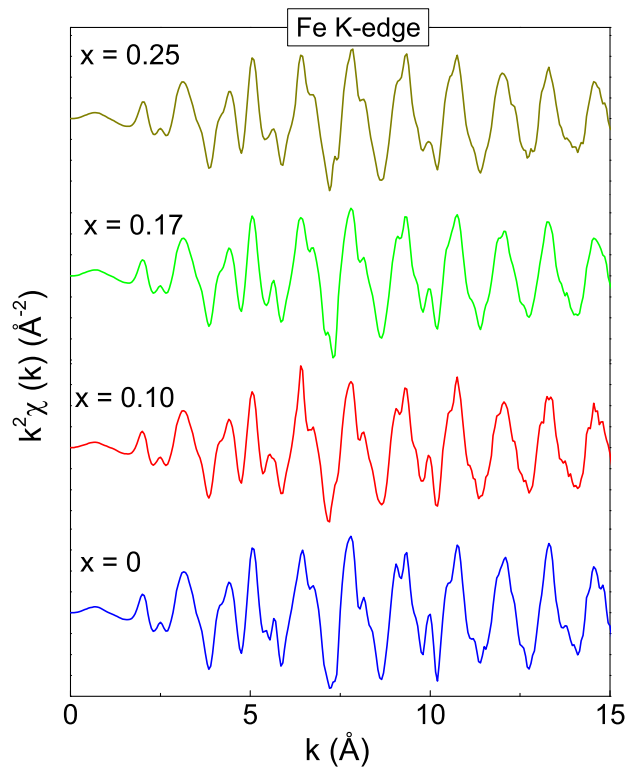


Figure 6.10: EXAFS patterns measured at 30 K for $\text{Fe}_2\text{Ti}_{1-x}\text{Cr}_x\text{Sn}$ compositions.

Next, to find out the origin of this peculiar magnetic ordering, local structure studies using XANES and EXAFS measurement have

been carried out at room temperature and at low temperatures (30 K and 150 K) probing the Fe K edge. The obtained $\chi(k)$ as a function of wave number, k measured for the $\text{Fe}_2\text{Ti}_{1-x}\text{Cr}_x\text{Sn}$ series of samples are shown in figure 6.10. The data shows good oscillation upto 15\AA^{-1} in k space. The $\chi(k)$ data have been Fourier transformed into R space as shown in figure 6.11.

Atomic arrangements in full Heusler system Fe_2TiSn is such that each Fe have 4 Ti and 4 Sn as its nearest neighbor at a distance of $\sim 2.3\text{ \AA}$ and 6 Fe atoms at $\sim 3.03\text{ \AA}$ distance. The first prominent peak around 2.3 \AA is thus formed because of Fe–Ti and Fe – Sn bonds, while the peak at $\sim 3.0\text{ \AA}$ is due to Fe–Fe. Thus, the EXAFS data for $\text{Fe}_2\text{Ti}_{1-x}\text{Cr}_x\text{Sn}$ compositions has been analyzed by considering these three independent direct scattering paths. The primary structural parameters from the X ray diffraction measurement were used as starting guess for the EXAFS analysis. The bond distances and thermal mean square factor(σ^2) of the respective paths have been varied until a good fit is achieved in the range of $1.7\text{--}3.1\text{\AA}$ in R space and the extracted values are shown in table 6.4. Further, XAFS spectra measured at different temperatures is shown in Fig. 6.12 for one nominal composition($\text{Fe}_2\text{Ti}_{0.9}\text{Cr}_{0.1}\text{Sn}$). No drastic change in the pattern proves that there is no structural change present upto room temperature.

It can be clearly seen from the extracted parameters that in all compositions that the Fe–Ti distance is smaller than the Fe–Sn distance even at 300 K, whereas being a cubic X_2YZ Heusler structure Ti and Sn are supposed to be equidistant from Fe. Moreover Fe–Sn and Fe – Fe are in good agreement with the distances calculated from X ray diffraction measurement, whereas Fe–Ti distances are smaller. The mismatch in the bond distance implies a local structural disorder, probably caused by the stronger $d - d$ hybridization between Fe and Ti d orbitals, than Sn p orbital.

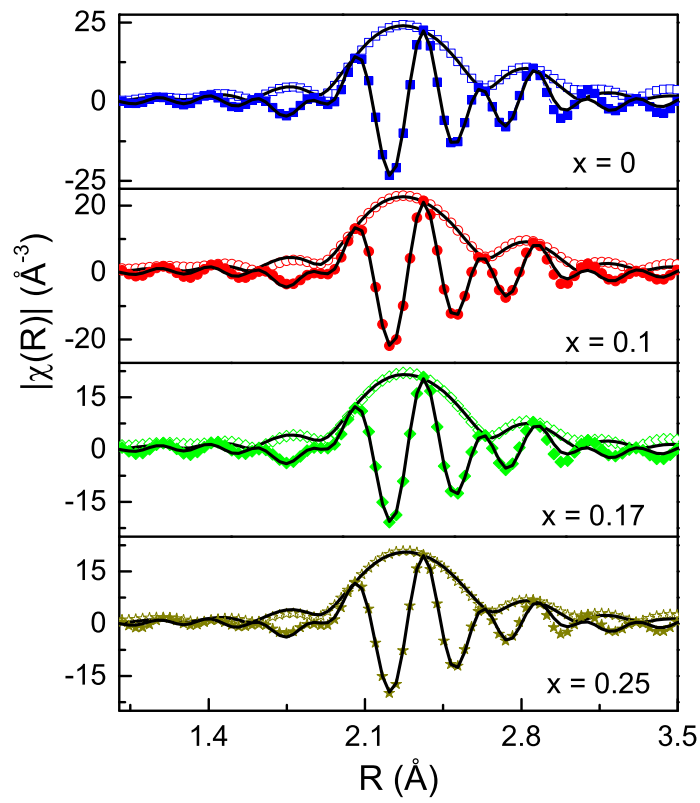


Figure 6.11: EXAFS patterns measured at 30 K for $\text{Fe}_2\text{Ti}_{1-x}\text{Cr}_x\text{Sn}$ compositions.

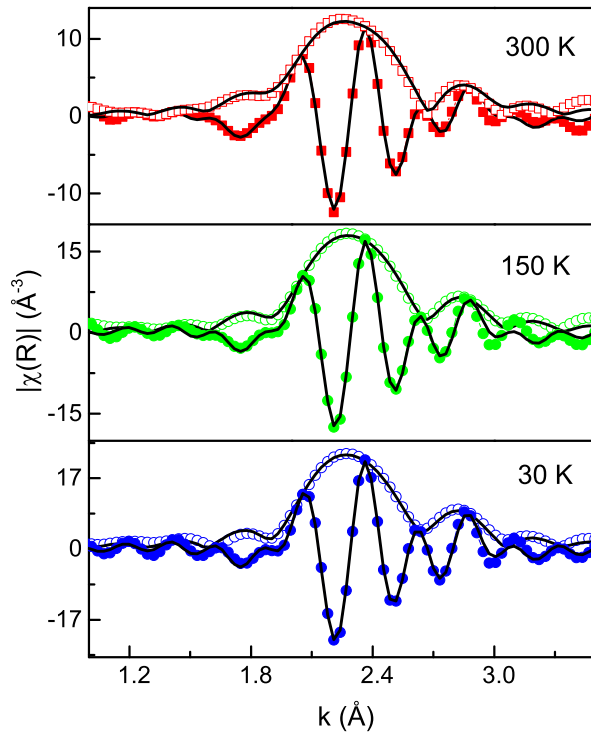


Figure 6.12: EXAFS patterns measured at different temperatures for $\text{Fe}_2\text{Ti}_{0.75}\text{Cr}_{0.25}\text{Sn}$ compositions.

Table 6.4: Bond distances, thermal mean square variation (σ^2), coordination number (CN), extracted from EXAFS data fitting of $\text{Fe}_2\text{Ti}_{1-x}\text{Cr}_x\text{Sn}$ samples measured at 30K. Values of x are shown in the table.

	Bond	CN	R (\AA)	σ^2 (\AA^2)
x = 0	Fe–Sn	4	2.6205(26)	0.0035(3)
	Fe–Ti	4	2.5966(64)	0.0082(9)
	Fe–Fe	6	3.0135(59)	0.0081(8)
x = 0.1	Fe–Sn	4	2.6232(22)	0.0038(2)
	Fe–Ti/Cr	4	2.5964(48)	0.083(7)
	Fe–Fe	6	3.0243 (51)	0.0090(7)
x = 0.17	Fe–Sn	4	2.6236(29)	0.0041(3)
	Fe–Ti/Cr	4	2.5893(60)	0.0107(11)
	Fe–Fe	6	3.0256(75)	0.0164(19)
x = 0.25	Fe–Sn	4	2.6236(33)	0.0043(3)
	Fe–Ti/Cr	4	2.5867(69)	0.091(10)
	Fe–Fe	6	3.0298(90)	0.0117(13)

Upon the substitution of Cr, Fe – Sn distance does not change much, which indicates a very small effect of Fe – Sn bond on the magnetism of these compositions. Fe – Ti distances decreases with the increase of Cr concentration, which is in line with the decrease in lattice parameters after substitution of Ti with Cr. However the interesting point to note here is that, Fe–Fe distance remains almost constant despite contraction of the unit cell.

Since no structural change has been observed, the origin of this anomalous change in scattering path distances probably lies in the electronic structure. The XANES region is good probe to analyze the electronic structure and the same is plotted as a function of applied energy for all prepared compositions are shown in figure 6.11(a). The edge feature we focus on is marked by “A”. A comparison between the two patterns presented in figure 6.13(a) shows that, whereas the other feature remains unchanged upon Cr substitution, only a subtle change in A feature is observed. In case of pure Fe_2TiSn a clear shoulder can be observed before the main absorption jump, but after 25% Cr substitution the feature becomes fairly smooth.

To find the origin of this change, XANES pattern was simulated for pristine Fe_2TiSn and Fe_2CrSn composition using Full multiple scattering technique [24] implemented in FEFF9 code [73].

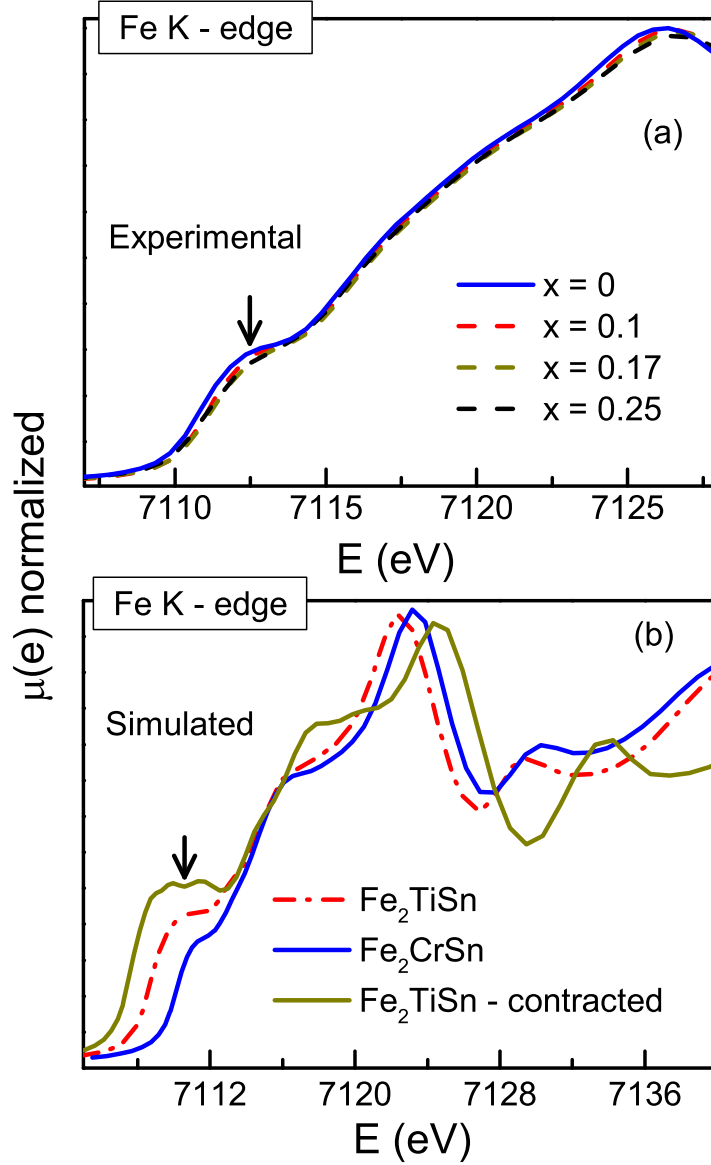


Figure 6.13: (a) XANES pattern for $\text{Fe}_2\text{Ti}_{1-x}\text{Cr}_x\text{Sn}$ compositions at 30K temperature. (b) Simulated XANES patterns for Fe_2TiSn and Fe_2CrSn .

A huge cluster of 115 atoms was considered to ensure convergence cycle. Calculation of XANES spectrum was done considering both dipole and quadrupole transition. To check the effect of lattice shrinking on Cr substitution a XANES pattern was also simulated for Fe_2TiSn using a contracted lattice parameter, with the value

matching with calculated lattice parameter of Fe_2CrSn . All the simulated patterns are plotted in figure 6.13(b). A feature to feature matching is obtained in experimental XANES spectrum are present in the simulated patterns. The “A” feature indeed become smoother in case of Fe_2CrSn composition. Calculation of the XANES pattern for the contracted lattice shows that, the “A” feature becomes more sharp, so clearly the change in the feature comes from electronic structure and not from lattice shrinking. It has been previously reported [40, 57] that the “A” feature appearing in the main absorption edge of Fe, comes from $\text{Fe } 1s \rightarrow 3d$ dipolar transition.

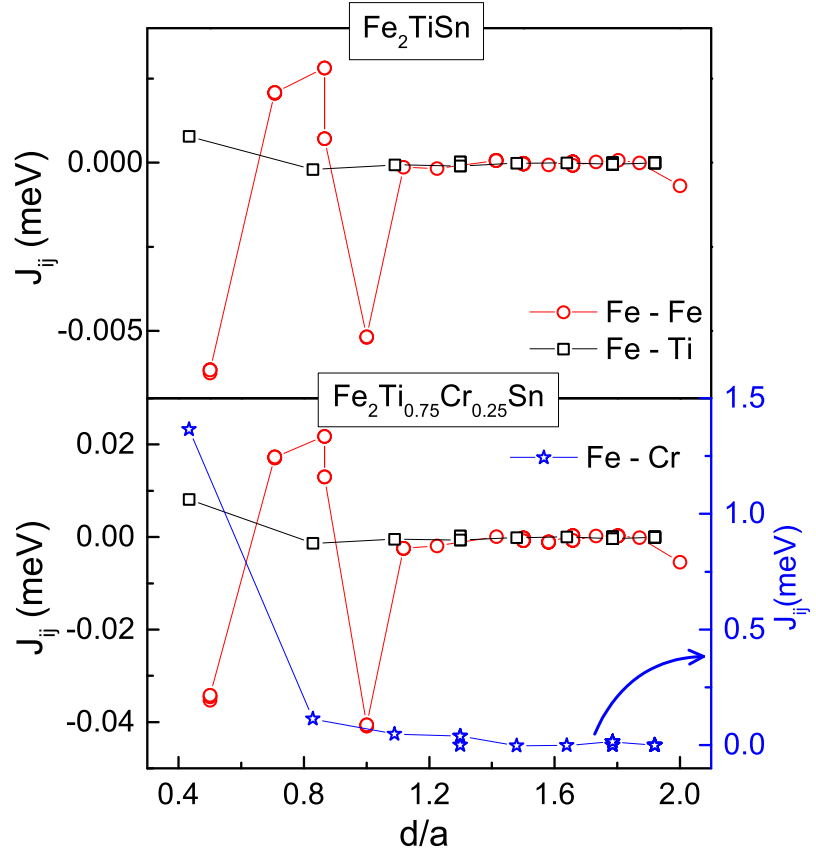


Figure 6.14: Heisenberg exchange coupling parameter, J_{ij} , plotted against Fe–Fe, Fe–Cr and Fe–Ti distance normalized to the lattice parameter, in Fe_2TiSn (solid line) and 25% Cr–substituted composition.

This feature gets enhanced for a $\text{Fe } 3d - 4p$ orbital mixing. So a diminishing nature of “A” indicates less mixing of $3d$ and $4p$ orbital in $\text{Fe}_2\text{Ti}_{0.75}\text{Cr}_{0.25}\text{Sn}$ than pristine Fe_2TiSn .

Electronic structure-wise Fe_2TiSn is a semimetal with a pseudo gap at Fermi level. The electronic states in the vicinity of E_F are populated by Fe $3d$ states [82] and the $4p$ states stay above the E_F . So less mixing of the occupied $3d$ band and unoccupied $4p$ orbital, that takes place in Cr substituted compositions, indicate decrease in the Fe – Fe interaction and probably leads to a band gap opening near the Fermi level.

Thus the XANES plots explicitly shows that, with the increase in Cr concentration the Fe $3d$ - $4p$ decreases. Simultaneously, the EXAFS analysis shows increase in the Fe - Fe scattering path distance.

6.2.5 Theoretical calculation

To further understand the impact of changing the $3d$ - $4p$ hybridization between Fe atoms, Heisenberg exchange coupling parameter (j_{ij}) was calculated using SPRKKR package. The exchange coupling parameter for Fe – Fe, Fe–Ti and Fe–Cr bonds, for pristine and 25% Cr substituted Fe_2TiSn are shown in figure 6.14. The Fe–Fe coupling energy is oscillatory in nature in both of the compositions in accordance with the RKKY exchange between the atoms. In case of Fe_2TiSn the oscillation varies between -0.08 meV to 0.08 meV, which becomes stronger after the substitution of Cr, with j_{ij} varying between -0.35 meV to 0.3 meV. But on the other hand, in 25% Cr substituted composition Fe–Cr bond gives rise to a huge value of $j_{ij} = 1.4$ meV. The non-oscillatory nature of this exchange energy indicates a localized magnetic moment. So, the competition between RKKY exchange between Fe atoms and localized moment at the Cr site gives rise to the compensating nature of magnetism in this compositions.

Further, the origin of localized moment is observed in the spin polarized total DOS and orbital projected DOS (pDOS), calculated

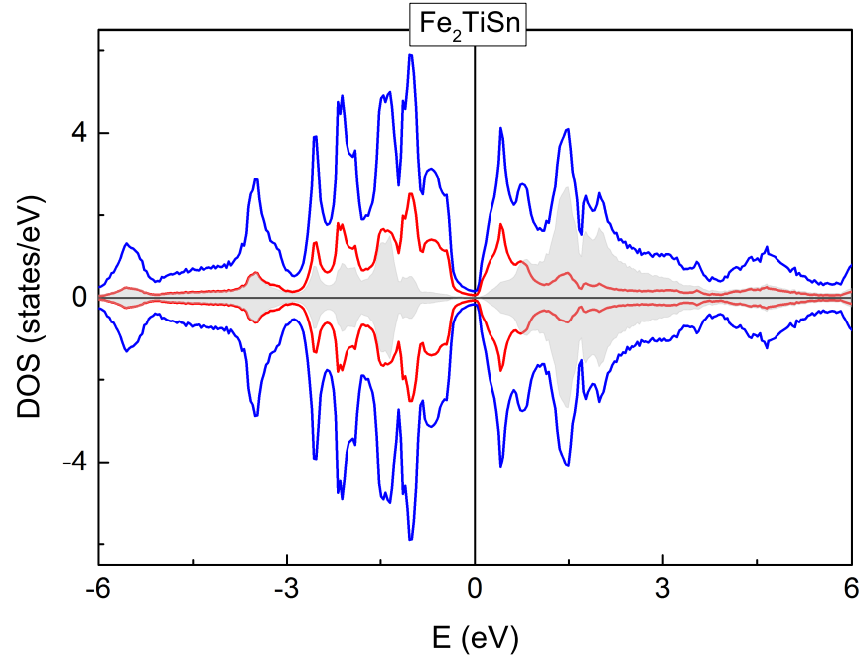


Figure 6.15: Spin projected total and partial DOS for pristine Fe_2TiSn composition.

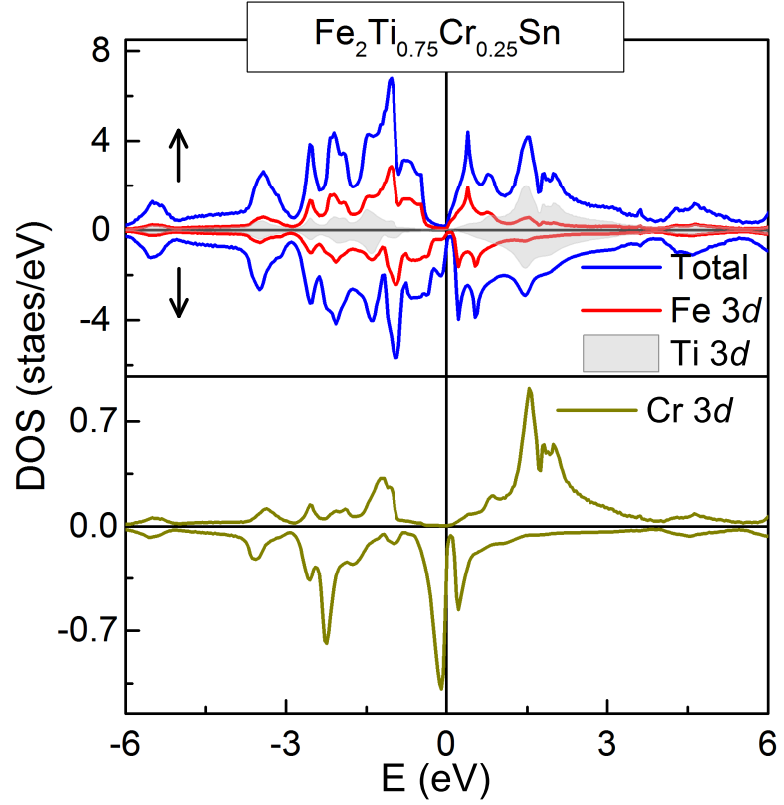


Figure 6.16: Spin projected total and partial DOS for 25% Cr substituted Fe_2TiSn . For clarity pDOS of the Cr d state is shown in the lower panel.

for pristine and 25% Cr substituted Fe_2TiSn as shown in figure 6.15 and figure 6.16 respectively. The DOS in pristine Fe_2TiSn is symmetric in both spin channels and small pseudogap is present at the Fermi level. Most of the bands near Fermi level are from Fe 3d bands, and no strong hybridization can be observed between the other atoms. With 25% substitution of Cr, the symmetry between majority and minority spin band breaks down. Fermi level in the majority spin band stays in the gap but in minority spin band it is shifted outside the gap, thus making the system half-metallic.

The lower panel of figure 6.16 shows the pDOS for Cr d band. A strong peak in the pDOS of Cr indicates strong electron localization in Cr in accordance with the localized magnetic moment seen from j_{ij} parameters at Cr site. This localization of Cr moment gives rise to the ferromagnetic moment in 25% Cr substituted composition.

6.2.6 Resistivity Measurement

Temperature dependent resistivity ρ of $\text{Fe}_2\text{Ti}_{1-x}\text{Cr}_x\text{Sn}$ measured in the temperature range 2K – 300K, using standard four probe method is shown in figure 6.17. As evident from the $\rho(T)$ curves, behavior of the $\rho(T)$ distinctively changes after the inclusion of Cr in the system. The Cr substituted compositions shows a typical metallic behavior at low temperature, and as the temperature increases, a drop in resistivity is observed at higher temperature. The transition temperatures for resistivity(T_{tr}) is extracted from the experimental data. T_{tr} for $x = 0.1, 0.17$ and 0.25 compositions are 183 K, 60 K and 100 K respectively. Possibility of any first order phase transition can be ruled out, as there is no hysteresis present between heating and cooling curve of resistivity. Moreover EXAFS measured at different temperatures, as shown in Fig. 6.12 also did not show any sign of crystal structural change. On the other hand,

sharp decrease in resistivity at the onset of magnetic ordering is well known in other ferromagnetic systems including Fe [79] and Ni [98] metals. Similar resistivity maxima has also been seen in full Heusler systems like Co_2TiZ ($Z = \text{Si}, \text{Ge}$ [9], Al [30]). In the magnetically ordered phase spin scatterings freezes out and as a result a decrease in resistivity with temperature is achieved. The anomalous resistivity behavior have been theoretically investigated by Kataoka [34] and according to him, a change in resistivity behavior is expected in general at the magnetic transition temperature but few parameters like, small number of charge carriers, low stability of magnetic order and large value of electron mean free path gives rise to a negative gradient of resistivity at the magnetically disordered state of a system. Since, in the present compositions the magnetic transition temperature (T_{cl}) are very close to the resistivity transition temperature (T_{tr}), the reason for the observed anomalous $\rho(T)$ behavior is magnetic in nature.

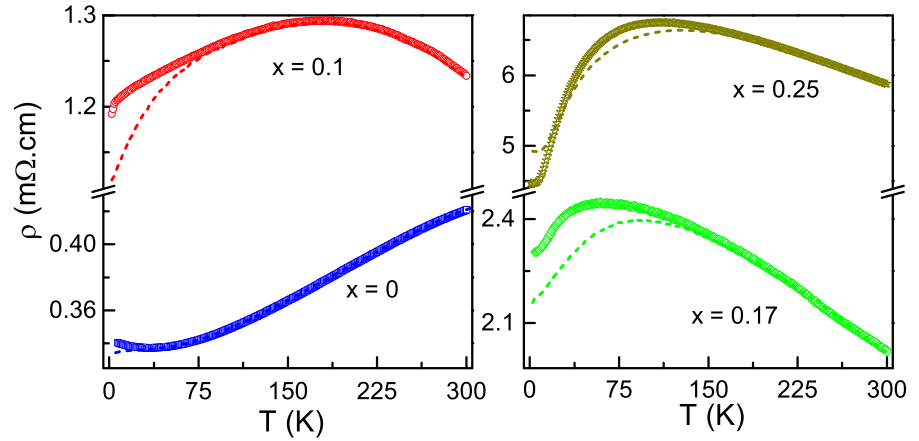


Figure 6.17: Variation of resistivity as a function of temperature for all prepared compositions of $\text{Fe}_2\text{Ti}_{1-x}\text{Cr}_x\text{Sn}$ series. The dotted line represents $\rho(T)$ under the application of 5T magnetic field.

On the other hand absolute value of ρ increases drastically with the increase in Cr concentration in the system. Resistivity of the parent compound Fe_2TiSn shows a metallic behaviour with $335 \mu\Omega$ at 2K. Only a substitution of 10% Cr in the system increases the resistivity to $1100 \mu\Omega$. Electronic transport in the Fe_2TiSn compo-

sition is dominated by hole type carrier as evident from its positive Seebeck coefficient (chapter 3.3). Substitution of Cr introduces electron in the system thus decreasing the total carrier number, justifying the overall increase in resistivity. Also stronger electron-electron correlation play a part in decreasing electronic conductivity.

The residual resistivity ratios ($RRR = \frac{\rho(300)}{\rho(2)}$) of the compositions decreases after the substitution of Cr at Ti site. For pristine Fe_2TiSn the RRR value is 1.23 which decreases to 0.876 after 17% Cr substitution. Further inclusion of Cr increases the RRR value to 1.321. Since there is no experimental evidence of significant change in atomic disorder, this low RRR values probably indicate residual spin disorder scattering upto the lowest temperature. Origin of this spin disorder scattering lies in the presence of magnetic cluster in the system. In case of 25% Cr substituted composition, cluster contribution is negligible and hence an increase in RRR is observed.

The low temperature part of $\rho(T)$ was fitted using a power law, given by $\rho(T) = A + BT^\alpha$. Fitting of the resistivity curves using the power law for two nominal compositions are shown in figure 6.18. For pristine and 10% Cr substituted Fe_2TiSn , the value of α come out to be close to 0.5, which indicates the dominating weak localization effect in these compositions [41]. In case of 17% Cr substituted composition the value of α is 2, which indicates a normal metallic transport, dominated by electron – electron scattering. For $x = 0.25$ composition the value of α is close to 3. Although there is no theoretical explanation for this kind of power law, numerous half-metallic systems known to follow a T^3 temperature dependence of resistivity [20, 25]. Since in our case the value of exponent is very close to 3, it might indicate a half metallic ground state in the system.

In case of half metallic system the electron–electron and electron–magnon scattering drastically damps down because

of the presence of a band gap at one of the spin channel. These processes are spin flip scattering process and thus needs the presence of both spins to complete a full spin wave. According to Watts *et. al.* [91] the absence of spin down electron decreases the electron–magnon scattering exponentially, and the resistivity should follow the rule, $\rho(T) = \rho_0 + AT^2 \exp(-\frac{E_g}{k_B T})$ in the half metallic region. This empirical law has been used to explain many other half metallic systems like CrO_2 [8], Fe_2CoSi [20] etc. Since our previous power law fitting of resistivity indicates a half metallic ground state, our resistivity data was further fitted using the exponential law. The experimental data fits nicely to the equation in the temperature range 2 K – 25 K. The obtained band gap from the fitting is 1.4 meV.

Further $\rho(T)$ was also measured with the application of 5T magnetic field as shown in figure 6.17. Except the case in 25% Cr substituted composition, resistivity decreases after the application of magnetic field. Decrease in resistivity in the presence of magnetic field is in accordance with our observation of electron scattering mechanism at low temperature region of $\rho(T)$ since, both weak localization and electron – electron scattering decrease with the application of magnetic field. On the other hand, an increase in the value of resistivity can occur in very specific cases. To understand the effect of magnetic field on resistivity, magnetoresistance was measured for the compositions.

6.2.7 Magnetoresistance

Figure 6.19(a) shows the temperature variation of magnetoresistance ($\text{MR} = \% \frac{\rho_H - \rho_0}{\rho_0} \times 100$) results of the $\text{Fe}_2\text{Ti}_{1-x}\text{Cr}_x\text{Sn}$ series in the range of 2K to 300K, under the application of 5T magnetic field. As expected, the MR has a negative value for upto 17% Cr substitution of Ti in Fe_2TiSn in the the whole temperature range. Interestingly, the 25% Cr substituted composition have positive MR

at low temperature, and changes to negative near 30 K temperature. Generally negative MR is observed in ferromagnetic alloys as the electrical conduction at low temperature is always dominated by electron–electron scattering. Application of magnetic field decreases this Fermi liquid like states. As a result, the resistivity decreases, giving rise to negative value of MR. For comparison MR was also measured as function of applied field at 5K temperature and the results are plotted in figure 6.19. Clearly upto 17% Cr substituted compositions show negative MR upto high magnetic field, whereas 25% Cr substituted composition shows a crossover from negative to positive MR and indicates different scattering mechanism. A positive value of MR can be achieved in general due to Lorentz force on resistivity in the presence of magnetic field [32]. But in case of Lorentz force effect MR follows a quadratic magnetic field dependence, and saturate at higher field. In the current observation MR of 25% Cr substituted composition changes linearly with the applied field as shown in the figure 6.19(b). On the other hand, in half metallic system, electron – magnon scattering freezes out at low temperature due to spin polarization. So at this temperature electron – defect scattering becomes important. Electron–defect scattering increases after application of magnetic field, which give rise to a positive magnetoresistance in half metallic system. The same has been theoretically expected [4] and experimentally observed in many half metals like, Mn_2CoAl [61], Fe_2CoSi [20]. Now revisiting the isothermal magnetization data shows that the experimental saturation magnetization ($0.69 \mu_B/\text{f.u.}$) is very close to what is expected from Slater–Pauling rule ($0.5\mu_B/\text{f.u.}$) for half metallic full Heusler systems [26]. The slight difference might come from the small amount of magnetic clusters present in the system.

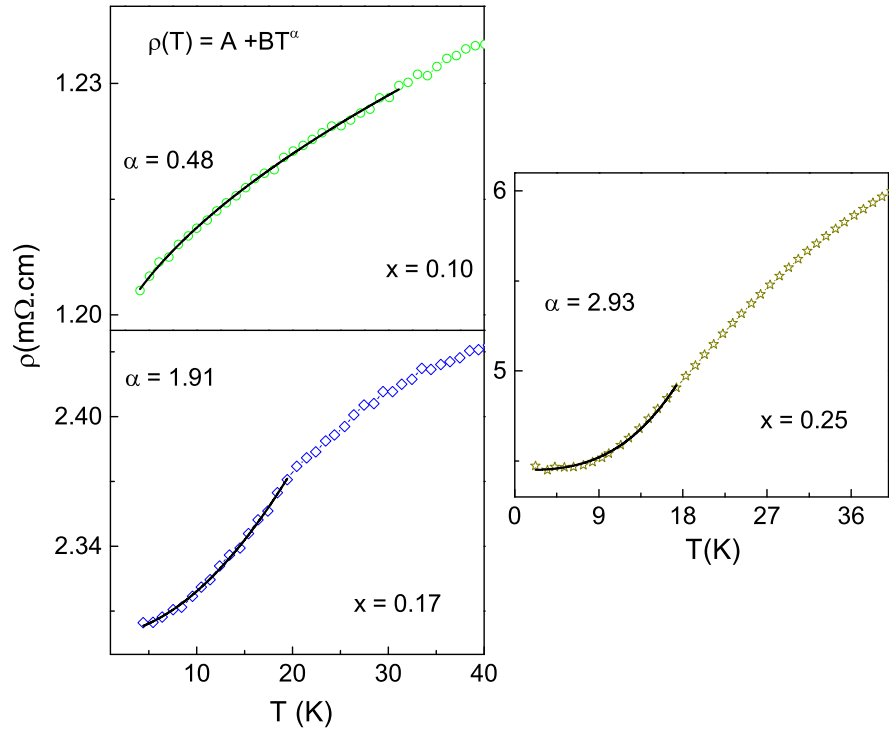


Figure 6.18: Power law fitting of resistivity for two nominal compositions, the red line represents the fitting. Fitting equation and values of the α are shown in the figure.

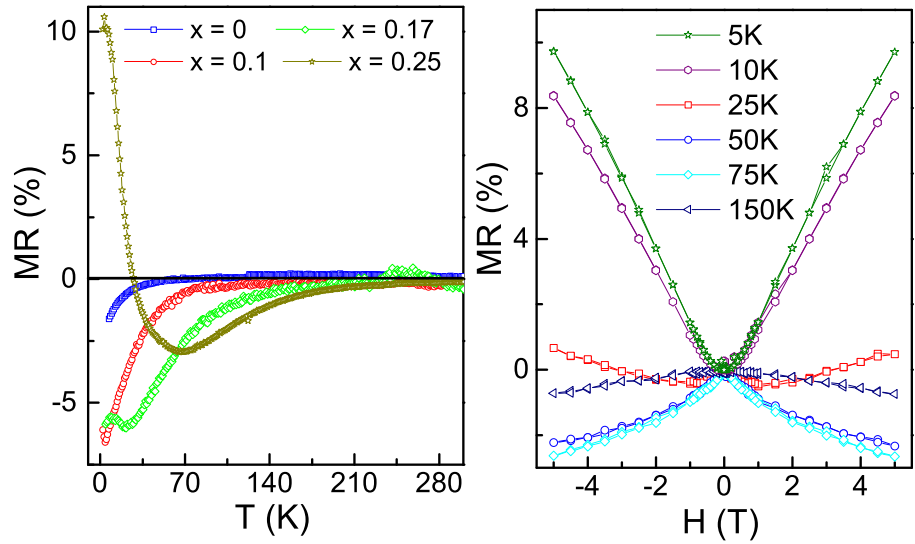


Figure 6.19: (a) Magnetoresistance of the prepared compositions as a function of temperature. inset shows the same as a function of applied magnetic field. (b) MR of the 25% Cr substituted Fe_2TiSn measured at different temperatures.

6.2.8 Summary

In summary, we have investigated the $\text{Fe}_2\text{Ti}_{1-x}\text{Cr}_x\text{Sn}$ compositions in search for half metallic ferromagnetism. Magnetization measurements results shows that, with the increase in Cr concentration, at first antiferromagnetic and ferromagnetic interactions compete, which finally resulting in a ferromagnetic order after 25% substitution of Cr. Density of States and Heisenberg exchange parameter calculation helps to understand the magnetic ordering in these compositions. The local magnetic moment at Cr site and RKKY exchange between Fe sites is responsible for the signatures of competing magnetic interactions observed in the magnetic measurements. The magnetic phase transition affects the resistivity and a metal to semiconductor transition. Analysis of low temperature $\rho(T)$ indicates that 25% Cr substituted composition has a half metallic ground state. DOS calculation and magnetoresistance resistance measurements supports this claim.

Chapter 7

Conclusions and Future scope

7.1 Preamble

We summarize the main findings and conclusions from the thesis work in this chapter. At the end of the chapter we provide an outlook on further study. We have prepared and analyzed three set of samples, $\text{Fe}_{2-x}\text{Ti}_{1+x}\text{Sn}$, $\text{Fe}_2\text{TiSn}_{1-x}\text{M}_x$ (with $\text{M} = \text{Si}, \text{Ge}$ and Sb) and $\text{Fe}_2\text{Ti}_{1-x}\text{Cr}_x\text{Sn}$ using various experimental and theoretical procedures. The major conclusions from the work are the following.

7.2 Major findings

1. It was found that small decrease in Fe concentration can successfully decrease the antisite disorder between Fe/Ti in Fe_2TiSn although it increases strain in the system. Replacing Fe with higher amount of Ti eventually leads to increase the disorder.
2. The origin of anomalous low temperature upturn present in resistivity of Fe_2TiSn was of much debate in literature. Our work suggests that the low temperature anomaly might come from weak localization of electrons in the disordered system, which goes away as the disorder decreases.

3. Our work found that the previously anticipated weak ferromagnetism in Fe_2TiSn is due to presence of fluctuation in the system. The spin fluctuation eventually gives rise to superparamagnetic ordering of magnetic clusters at low temperature.
4. Substitution of higher electronegative element at the Sn site can also effectively decrease the antisite disorder in Fe_2TiSn , evident from the $\text{Fe}_2\text{TiSn}_{1-x}\text{Sb}_x$ series of compositions, also $\geq 25\%$ Sb substitution can show half metallic ground state.
5. Large mismatch between the atomic radii of Sn with the substituent atom might not be effective to decrease the disorder as seen from $\text{Fe}_2\text{TiSn}_{0.95}\text{M}_{0.05}$.
6. Magnetic ordering in $\text{Fe}_2\text{TiSn}_{1-x}\text{Sb}_x$ series originates due to decreased Fe–Fe bond distance and increased p – d hybridization between Fe with main group elements.
7. Magnetic ordering in $\text{Fe}_2\text{TiSn}_{0.95}\text{M}_{0.05}$ originates solely because of the decrease in Fe–Fe bond distance, which strengthen the RKKY exchange between the only magnetic atoms in the system, giving rise to higher itinerant magnetization in these samples.
8. Substitution of Cr at Ti site of Fe_2TiSn can successfully decrease the antisite disorder as well as generate half metallicity.
9. The Cr substituted compositions show interesting FM/AFM competing magnetic ordering which evolves due to two factors, localized moment at Cr site and itinerant magnetization for Fe–Fe RKKY exchange.

7.3 Future scope

This research work have shown some very interesting results and can be extended for further explorations and utilizations as summarized below:

1. The scheme we used to control disorder in Fe_2TiSn can be checked for its universality in other systems.
2. We found indirect proof of half metallic ground state in Sb and Cr substituted Fe_2TiSn , so an experimental band structure study using Photo Emission spectroscopy(PES) might be helpful to confirm it.
3. The half metallicity we found in Sb and Cr substituted Fe_2TiSn can be checked for device application.

Chapter 8

Appendix

8.1 Preamble

Two new experimental set up was designed to measure temperature dependent resistivity($\rho(T)$) and Seebeck co-efficient(S) upto low temperature using a liquid Helium based closed cycle refrigerator. Instrument specification and working principle of this two instruments are discussed in the following sections.



Figure 8.1: Resistivity measurement probe with a standard sample mounted on it.

8.2 Resistivity measurement set up

Functionally the measurement system consists of mainly four parts, the sample holder, vacuum unit, temperature control unit and mea-

surement and data acquisition unit. The measurement system is shown in figure 8.1.

A picture of the sample holder is shown in figure 8.2. It is part of a printed circuit board(PCB) having four parallel strip of copper, which act as voltage and current probes. Fine copper wires are soldered on one side of this PCB, to connect it to the source meter and Voltmeter. The sample is mounted on the four copper strips using G-vernice. Further to ensure electrical connection very small amount of silver paste is used. The sample holder assembly is placed on the cold finger of the cryostat by using Apiezon N Grease, which is a good thermal conductor and works at very low temperature.

The measurements are carried out in an evacuated chamber in order to insulate the sample from outer environment. Figure 8.1 shows the measurement chamber. It is connected to a turbo molecular pump(Oerlikon, Turbolab 80), which is used to evacuate the chamber upto 10^{-4} mbar. The temperature control unit consists of three component, a liquid He based closed cycle refrigerator(Sumitomo, HC-4E1), a cold head(Sumitomo, CH-202) and a temperature controller(Lakeshore, 330 temperature controller).

The system is automated using LabView program. The front panel of the resistivity measurement program is shown in figure 8.3.

8.3 Seebeck co-efficient measurement set up

A schematic of Seebeck co-efficient measurement set up is shown in figure 8.4. Here a rectangular piece of sample is placed over two Copper pole. Heater wire is wound on one of the pole. So, when current passes through the heater wire, the pole gets heated while the other

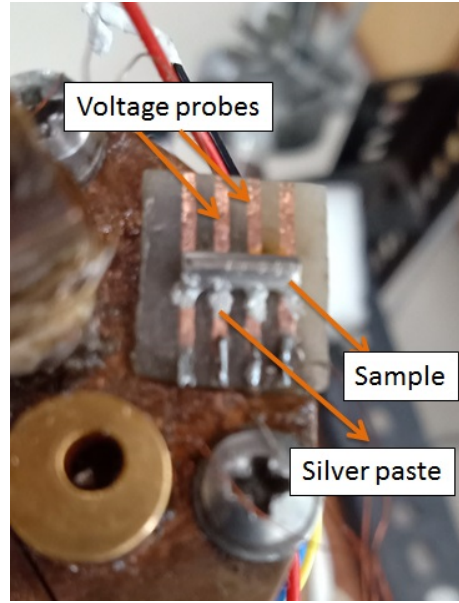


Figure 8.2: Reactivity measurement probe with a standard sample mounted on it.

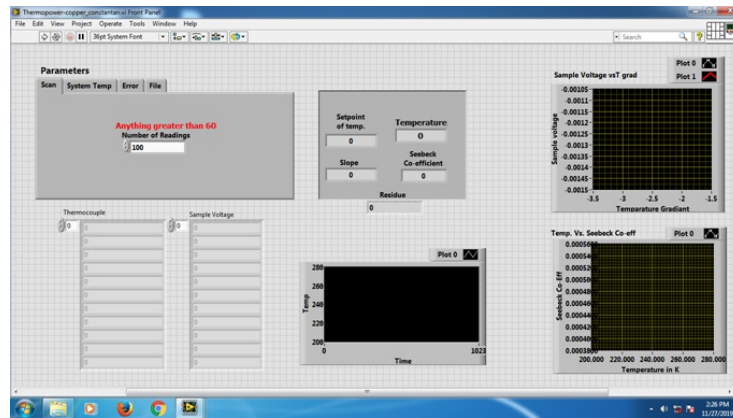


Figure 8.3: Front panel of reactivity measurement program in LabView.

pole remains in the system temperature. This temperature gradient between the two poles generate Seebeck voltage in the sample. The voltage To measure the thermal gradient Copper–Constantan thermocouple was used, which gives stable Seebeck voltage within a temperature range of 80 K – 300 K. Hence, our Seebeck co-efficient measurement system gives reliable data upto 80 K.

A photograph of the measurement system is shown in figure 8.5

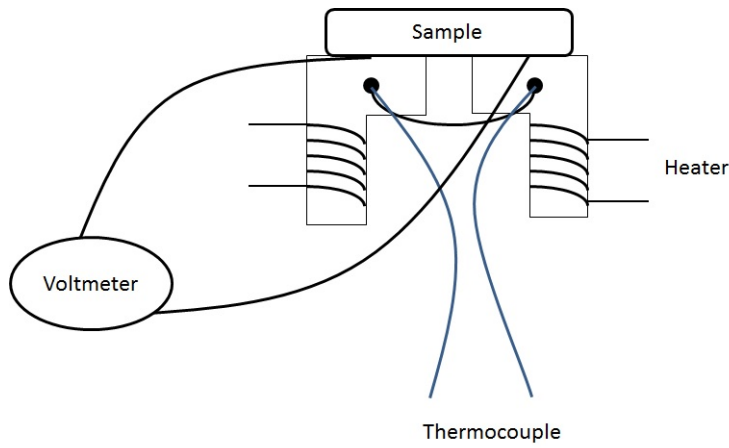


Figure 8.4: Schematic of the seebeck co-efficient measurement set-up.

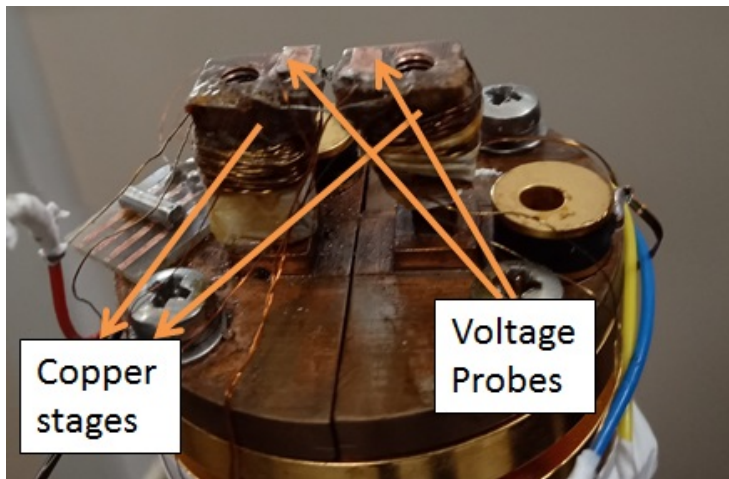


Figure 8.5: The seebeck co-efficient measurement set-up.

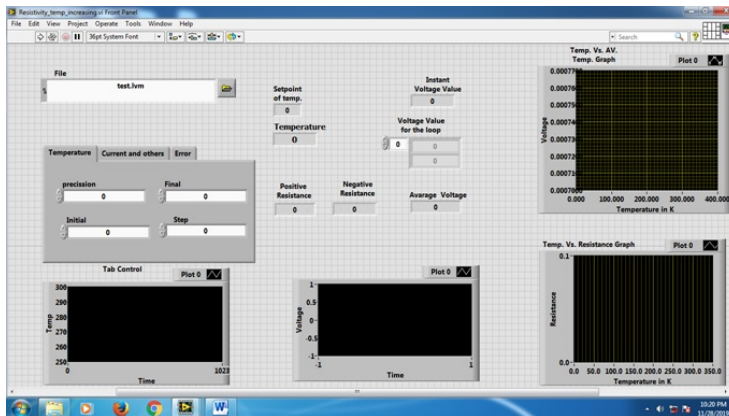


Figure 8.6: Front panel of the seebeck co-efficient measurement set-up program in LabView.

Bibliography

- [1] <http://hydrogen.physik.uni-wuppertal.de/hyperphysics/hyperphysics/hbase/solids/squid.html>.
- [2] <https://www.hindawi.com/journals/jnm/2011/606714/fig2/>.
- [3] <http://canfield.physics.iastate.edu/course/HC18A.pdf>.
- [4] A. A. Abrikosov. Quantum magnetoresistance. *Phys. Rev. B*, 58:2788–2794, Aug 1998.
- [5] Hiro Akinaga, Takashi Manago, and Masafumi Shirai. Material design of half-metallic Zinc-blende CrAs and the synthesis by molecular-beam epitaxy. *Japanese Journal of Applied Physics*, 39(Part 2, No. 11B):L1118–L1120, nov 2000.
- [6] James D. Aldous, Christopher W. Burrows, Ana M. Sánchez, Richard Beanland, Ian Maskery, Matthew K. Bradley, Manuel dos Santos Dias, Julie B. Staunton, and Gavin R. Bell. Cubic MnSb: Epitaxial growth of a predicted room temperature half-metal. *Phys. Rev. B*, 85:060403, Feb 2012.
- [7] Lakhan Bainsla, M Manivel Raja, A K Nigam, B S D Ch S Varaprasad, Y K Takahashi, K G Suresh, and K Hono. Investigation of the quaternary $\text{Fe}_{2-x}\text{Co}_x\text{MnSi}$ ($0 \leq x \leq 0.6$) alloys by structural, magnetic, resistivity and spin polarization measurements. *Journal of Physics D: Applied Physics*, 48(12):125002, mar 2015.

- [8] A. Barry, J. M. D. Coey, L. Ranno, and K. Ounadjela. Evidence for a gap in the excitation spectrum of CrO_2 . *Journal of Applied Physics*, 83(11):7166–7168, 1998.
- [9] Joachim Barth, Gerhard H. Fecher, Benjamin Balke, Siham Ouardi, Tanja Graf, Claudia Felser, Andrey Shkabko, Anke Weidenkaff, Peter Klaer, Hans J. Elmers, Hideki Yoshikawa, Shigenori Ueda, and Keisuke Kobayashi. Itinerant half-metallic ferromagnets Co_2TiZ ($Z = \text{Si, Ge, Sn}$): Ab initio calculations and measurement of the electronic structure and transport properties. *Phys. Rev. B*, 81:064404, Feb 2010.
- [10] S. Bedanta, O. Petravic, M. Aderholz, and W. Kleemann. A sample holder design for high temperature measurements in superconducting quantum interference device magnetometers. *Review of Scientific Instruments*, 76(8):083910, 2005.
- [11] A. Bhattacharyya, Deepti Jain, V. Ganesan, S. Giri, and S. Majumdar. Investigation of weak itinerant ferromagnetism and critical behavior of Y_2Ni_7 . *Phys. Rev. B*, 84:184414, Nov 2011.
- [12] Daniel I. Bilc, Geoffroy Hautier, David Waroquiers, Gian-Marco Rignanese, and Philippe Ghosez. Low-dimensional transport and large thermoelectric power factors in bulk semiconductors by band engineering of highly directional electronic states. *Phys. Rev. Lett.*, 114:136601, Mar 2015.
- [13] Dirk Bombor, Christian G. F. Blum, Oleg Volkonskiy, Steven Rodan, Sabine Wurmehl, Christian Hess, and Bernd Büchner. Half-metallic ferromagnetism with unexpectedly small spin splitting in the Heusler compound Co_2FeSi . *Phys. Rev. Lett.*, 110:066601, Feb 2013.
- [14] Scott Calvin and Kirin Emlet Furst. *XAFS for everyone*. Boca Raton : CRC Press,, 2013.

- [15] D. Choudhury, P. Mandal, R. Mathieu, A. Hazarika, S. Rajan, A. Sundaresan, U. V. Waghmare, R. Knut, O. Karis, P. Nordblad, and D. D. Sarma. Near-room-temperature colossal magnetodielectricity and multiglass properties in partially disordered $\text{La}_2\text{NiMnO}_6$. *Phys. Rev. Lett.*, 108:127201, Mar 2012.
- [16] R. A. de Groot, F. M. Mueller, P. G. van Engen, and K. H. J. Buschow. New class of materials: Half-metallic ferromagnets. *Phys. Rev. Lett.*, 50:2024–2027, Jun 1983.
- [17] J. A. De Toro, M. A. López de la Torre, M. A. Arranz, J. M. Riveiro, J. L. Martínez, P. Palade, and G. Filoti. Nonequilibrium magnetic dynamics in mechanically alloyed materials. *Phys. Rev. B*, 64:094438, Aug 2001.
- [18] A. R. Denton and N. W. Ashcroft. Vegard’s law. *Phys. Rev. A*, 43:3161–3164, Mar 1991.
- [19] S. V. Dordevic, D. N. Basov, A. Ślebarski, M. B. Maple, and L. Degiorgi. Electronic structure and charge dynamics of the Heusler alloy Fe_2TiSn probed by infrared and optical spectroscopy. *Phys. Rev. B*, 66:075122, Aug 2002.
- [20] Y. Du, G. Z. Xu, X. M. Zhang, Z. Y. Liu, S. Y. Yu, E. K. Liu, W. H. Wang, and G. H. Wu. Crossover of magnetoresistance in the zero-gap half-metallic Heusler alloy Fe_2CoSi . *EPL (Europhysics Letters)*, 103(3):37011, aug 2013.
- [21] W J Fan, L Ma, and S M Zhou. Sign change of skew scattering induced anomalous hall conductivity in epitaxial $\text{NiCo}(002)$ films: band filling effect. *Journal of Physics D: Applied Physics*, 48(19):195004, mar 2015.
- [22] Claudia Felser and Atsufumi Hirohata. *Heusler Alloys Properties, Growth, Applications*. Cham Springer International Publishing 2016.

- [23] J H J Fluitman, R Boom, P F De Chatel, C J Schinkel, J L L Tilanus, and B R De Vries. Possible explanations for the low temperature resistivities of Ni_3Al and Ni_3Ga alloys in terms of spin density fluctuation theories. *J. Phys. F: Met. Phys.*, 3(1):109, 1973.
- [24] Takashi Fujikawa. Basic features of the short-range-order multiple scattering XANES theory. *Journal of the Physical Society of Japan*, 62(6):2155–2165, 1993.
- [25] Nobuo Furukawa. Unconventional one-magnon scattering resistivity in half-metals. *Journal of the Physical Society of Japan*, 69(7):1954–1957, 2000.
- [26] I. Galanakis, P. H. Dederichs, and N. Papanikolaou. Slater-Pauling behavior and origin of the half-metallicity of the full-Heusler alloys. *Phys. Rev. B*, 66:174429, Nov 2002.
- [27] U. Geiersbach, A. Bergmann, and K. Westerholt. Structural, magnetic and magnetotransport properties of thin films of the Heusler alloys Cu_2MnAl , Co_2MnSi , Cu_2MnGe and Co_2MnSn . *J. Magn. Magn. Mater.*, 240(1):546 – 549, 2002.
- [28] P Giannozzi et al. Advanced capabilities for materials modelling with Quantum Espresso. *J. Phys.: Condens. Matter*, 29(46):465901, oct 2017.
- [29] G. F. Goya and V. Sagredo. Spin-glass ordering in $\text{Zn}_{1-x}\text{Mn}_x\text{In}_2\text{Te}_4$ diluted magnetic semiconductor. *Phys. Rev. B*, 64:235208, Nov 2001.
- [30] Tanja Graf, Joachim Barth, Benjamin Balke, Sascha Populoh, Anke Weidenkaff, and Claudia Felser. Tuning the carrier concentration for thermoelectrical application in the quaternary Heusler compound $\text{Co}_2\text{TiAl}_{1-x}\text{Si}_x$. *Scripta Materialia*, 63(9):925 – 928, 2010.

- [31] Tanja Graf, Claudia Felser, and Stuart S.P. Parkin. Simple rules for the understanding of Heusler compounds. *Progress in Solid State Chemistry*, 39(1):1 – 50, 2011.
- [32] J.-P. Jan. Galvamomagnetic and thermomagnetic effects in metals. volume 5 of *Solid State Physics*, pages 1 – 96. Academic Press, 1957.
- [33] J. D. Joannopoulos, Th. Starkloff, and Marc Kastner. Theory of pressure dependence of the density of states and reflectivity of Selenium. *Phys. Rev. Lett.*, 38:660–663, Mar 1977.
- [34] Mitsuo Kataoka. Resistivity and magnetoresistance of ferromagnetic metals with localized spins. *Phys. Rev. B*, 63:134435, Mar 2001.
- [35] Anton Kokalj. Xcrysden new program for displaying crystalline structures and electron densities. *Journal of Molecular Graphics and Modelling*, 17(3):176 – 179, 1999.
- [36] A Kolodziejczyk and J Spalek. Spin fluctuations in a very weak itinerant ferromagnet: Y_4Co_3 . *J. Phys. F: Met. Phys.*, 14(5):1277, 1984.
- [37] J. Kübler. Curie temperatures of zinc-blende half-metallic ferromagnets. *Phys. Rev. B*, 67:220403, Jun 2003.
- [38] J. Kübler, A. R. William, and C. B. Sommers. Formation and coupling of magnetic moments in Heusler alloys. *Phys. Rev. B*, 28:1745–1755, Aug 1983.
- [39] Devendra Kumar and A Banerjee. Coexistence of interacting ferromagnetic clusters and small antiferromagnetic clusters in $\text{La}_{0.5}\text{Ba}_{0.5}\text{CoO}_3$. *Journal of Physics: Condensed Matter*, 25(21):216005, may 2013.
- [40] S. Lafuerza, H. Gretarsson, F. Hardy, T. Wolf, C. Meingast, G. Giovannetti, M. Capone, A. S. Sefat, Y.-J. Kim, P. Glatzel,

- and L. de' Medici. Evidence of Mott physics in Iron pnictides from X-ray spectroscopy. *Phys. Rev. B*, 96:045133, Jul 2017.
- [41] Patrick A. Lee and T. V. Ramakrishnan. Disordered electronic systems. *Rev. Mod. Phys.*, 57:287–337, Apr 1985.
- [42] Y. H. Li, B. P. Uberuaga, C. Jiang, S. Choudhury, J. A. Valdez, M. K. Patel, J. Won, Y.-Q. Wang, M. Tang, D. J. Safarik, D. D. Byler, K. J. McClellan, I. O. Usov, T. Hartmann, G. Baldinozzi, and K. E. Sickafus. Role of antisite disorder on preamorphization swelling in Titanate Pyrochlores. *Phys. Rev. Lett.*, 108:195504, May 2012.
- [43] T. T. Lin, X. F. Dai, R. K. Guo, Z. X. Cheng, L. Y. Wang, X. T. Wang, and G. D. Liu. Anti-site-induced diverse diluted magnetism in LiMgPdSb-type CoMnTiSi alloy. *Scientific reports*, 7:42034, 2017.
- [44] D. N. Lobo, K. R. Priolkar, P. A. Bhobe, D. Krishnamurthy, and S. Emura. Correlation between local structure distortions and martensitic transformation in Ni₂MnIn alloys. *Applied Physics Letters*, 96(23):232508, 2010.
- [45] Y Machida, T Yoshida, T Ikeura, K Izawa, A Nakama, R Higashinaka, Y Aoki, H Sato, A Sakai, S Nakatsuji, N Nagasawa, K Matsumoto, T Onimaru, and T Takabatake. Anomalous enhancement of seebeck coefficient in Pr-based 1-2-20 system with non-Kramers doublet ground states. *JPS Conf. Proc.*, 592(1):012025, 2015.
- [46] B. R. Maddox, C. S. Yoo, Deepa Kasinathan, W. E. Pickett, and R. T. Scalettar. High-pressure structure of half-metallic CrO₂. *Phys. Rev. B*, 73:144111, Apr 2006.
- [47] M.K. Majee, P.A. Bhobe, and A.K. Nigam. Griffiths phase in antiferromagnetic CuCr_{0.95}Ti_{0.05}O₂. *J. Magn. Magn. Mater*, 485:112 – 117, 2019.

- [48] L. Makinistian, Muhammad M. Faiz, Raghava P. Panguluri, B. Balke, S. Wurmehl, C. Felser, E. A. Albanesi, A. G. Petukhov, and B. Nadgorny. On the half-metallicity of Co_2FeSi Heusler alloy: Point-contact Andreev reflection spectroscopy and ab initio study. *Phys. Rev. B*, 87:220402, Jun 2013.
- [49] Kenji Makoshi and Tôru Moriya. Effect of spin fluctuations on the specific heat of weakly and nearly ferromagnetic metals. *J. Phys. Soc. Jpn.*, 38(1):10–20, 1975.
- [50] Dan Mendels and Nir Tessler. Thermoelectricity in disordered organic semiconductors under the premise of the gaussian disorder model and its variants. *The Journal of Physical Chemistry Letters*, 5(18):3247–3253, 2014. PMID: 26276340.
- [51] Koichi Momma and Fujio Izumi. *VESTA3* for three-dimensional visualization of crystal, volumetric and morphology data. *Journal of Applied Crystallography*, 44(6):1272–1276, Dec 2011.
- [52] Sanchayita Mondal, Chandan Mazumdar, R. Ranganathan, Eric Alleno, P. C. Sreeparvathy, V. Kanchana, and G. Vaitheeswaran. Ferromagnetically correlated clusters in semimetallic Ru_2NbAl Heusler alloy and its thermoelectric properties. *Phys. Rev. B*, 98:205130, Nov 2018.
- [53] G. E. Moore. Cramming more components onto integrated circuits. *Proceedings of the IEEE*, 86(1):82–85, Jan 1998.
- [54] Tôru Moriya. Theory of itinerant electron magnetism. *J. Magn. Magn. Mater.*, 100(1):261 – 271, 1991.
- [55] VD Mote, Y. Purushotham, and BN Dole. Williamson-Hall analysis in estimation of lattice strain in nanometer-sized ZnO particles. *J. Theor. Appl. Phys.*, 6(1):6, Jul 2012.

- [56] N. F. MOTT and E. A. DAVIS. *Electronic Processes in Non-crystalline Materials*. Claredon Press • OXFORD, 1982.
- [57] Bassim Mounssef, Marli R. Cantarino, Eduardo M. Bittar, Tarsis M. Germano, Andreas Leithe-Jasper, and Fernando A. Garcia. Hard x-ray spectroscopy of the itinerant magnets $\text{RFe}_4\text{Sb}_{12}$ ($\text{R} = \text{Na}, \text{K}, \text{Ca}, \text{Sr}, \text{Ba}$). *Phys. Rev. B*, 99:035152, Jan 2019.
- [58] Naoto Nagaosa, Jairo Sinova, Shigeki Onoda, A. H. MacDonald, and N. P. Ong. Anomalous hall effect. *Rev. Mod. Phys.*, 82:1539–1592, May 2010.
- [59] N. Naghibolashrafi, S. Keshavarz, Vinay I. Hegde, A. Gupta, W. H. Butler, J. Romero, K. Munira, P. LeClair, D. Mazumdar, J. Ma, A. W. Ghosh, and C. Wolverton. Synthesis and characterization of Fe-Ti-Sb intermetallic compounds: Discovery of a new slater-pauling phase. *Phys. Rev. B*, 93:104424, Mar 2016.
- [60] Y. Okimoto, T. Katsufuji, T. Ishikawa, A. Urushibara, T. Arima, and Y. Tokura. Anomalous variation of optical spectra with spin polarization in double-exchange ferromagnet: $\text{La}_{1-x}\text{Sr}_x\text{MnO}_3$. *Phys. Rev. Lett.*, 75:109–112, Jul 1995.
- [61] Siham Ouardi, Gerhard H. Fecher, Claudia Felser, and Jürgen Kübler. Realization of spin gapless semiconductors: The Heusler compound Mn_2CoAl . *Phys. Rev. Lett.*, 110:100401, Mar 2013.
- [62] Himanshu Pandey and R. C. Budhani. Structural ordering driven anisotropic magnetoresistance, anomalous hall resistance, and its topological overtones in full-Heusler Co_2MnSi thin films. *Journal of Applied Physics*, 113(20):203918, 2013.
- [63] Linus Pauling. The nature of the interatomic forces in metals. *Phys. Rev.*, 54:899–904, Dec 1938.

- [64] John P. Perdew, Kieron Burke, and Matthias Ernzerhof. Generalized gradient approximation made simple. *Phys. Rev. Lett.*, 77:3865–3868, Oct 1996.
- [65] John P. Perdew, Adrienn Ruzsinszky, Gábor I. Csonka, Oleg A. Vydrov, Gustavo E. Scuseria, Viktor N. Staroverov, and Jianmin Tao. Exchange and correlation in open systems of fluctuating electron number. *Phys. Rev. A*, 76:040501, Oct 2007.
- [66] S. M. Podgornyykh, A. D. Svyazhin, E. I. Shreder, V. V. Marchenkov, and V. P. Dyakina. Low-temperature electron properties of Heusler alloys Fe_2VAl and Fe_2CrAl : Effect of annealing. *Journal of Experimental and Theoretical Physics*, 105(1):42–45, Jul 2007.
- [67] Joseph C. Prestigiacomo, David P. Young, Philip W. Adams, and Shane Stadler. Hall effect and the magnetotransport properties of $\text{Co}_2\text{MnSi}_{1-x}\text{Al}_x$ Heusler alloys. *Journal of Applied Physics*, 115(4):043712, 2014.
- [68] K. R. Priolkar, D. N. Lobo, P. A. Bhole, S. Emura, and A. K. Nigam. Role of Ni-Mn hybridization in the magnetism of the martensitic state of Ni-Mn-In shape memory alloys. *EPL (Europhysics Letters)*, 94(3):38006, apr 2011.
- [69] D. P. Rai, Sandeep, A. Shankar, R. Khenata, A. H. Reshak, C. E. Ekuma, R. K. Thapa, and San-Huang Ke. Electronic, optical, and thermoelectric properties of $\text{Fe}_{2+x}\text{V}_{1-x}\text{Al}$. *AIP Advances*, 7(4):045118, 2017.
- [70] M. P. Raphael, B. Ravel, Q. Huang, M. A. Willard, S. F. Cheng, B. N. Das, R. M. Stroud, K. M. Bussmann, J. H. Claassen, and V. G. Harris. Presence of antisite disorder and its characterization in the predicted half-metal Co_2MnSi . *Phys. Rev. B*, 66:104429, Sep 2002.

- [71] M.P. Raphael, B. Ravel, M.A. Willard, S.F. Cheng, B.N. Das, R.M. Stroud, K.M. Bussmann, J.H. Claassen, and V.G. Harris. Magnetic, structural, and transport properties of thin film and single crystal Co_2MnSi . *Applied Physics Letters*, 79(26):4396–4398, 2001. cited By 103.
- [72] B. Ravel and M. Newville. *ATHENA, ARTEMIS, HEPHAESTUS*: data analysis for X-ray absorption spectroscopy using *IFEFFIT*. *J. Synchrotron Radiat.*, 12(4):537–541, Jul 2005.
- [73] John J. Rehr, Joshua J. Kas, Fernando D. Vila, Micah P. Prange, and Kevin Jorissen. Parameter-free calculations of x-ray spectra with FEFF9. *Phys. Chem. Chem. Phys.*, 12:5503–5513, 2010.
- [74] H. M. Rietveld. A profile refinement method for nuclear and magnetic structures. *Journal of Applied Crystallography*, 2(2):65–71, Jun 1969.
- [75] Juan Rodríguez-Carvajal. Recent advances in magnetic structure determination by neutron powder diffraction. *Physica B*, 192(1):55 – 69, 1993.
- [76] Lue C. S. and Kuo Y.K. Thermal and transport properties of the Heusler-type compounds Fe_2TiSn . *J. Appl. Phys.*, 96(5):2681–2683, 2004.
- [77] G. Schmidt, D. Ferrand, L. W. Molenkamp, A. T. Filip, and B. J. van Wees. Fundamental obstacle for electrical spin injection from a ferromagnetic metal into a diffusive semiconductor. *Phys. Rev. B*, 62:R4790–R4793, Aug 2000.
- [78] K. Schröder and C. H. Cheng. Correlation of low-temperature caloric and magnetic effects in TiFe . *J. Appl. Phys.*, 31(12):2154–2155, 1960.

- [79] L. W. Shacklette. Specific heat and resistivity of iron near its curie point. *Phys. Rev. B*, 9:3789–3792, May 1974.
- [80] Xuwen Shi, Nianduan Lu, Guangwei Xu, Jinchen Cao, Zhiheng Han, Guanhua Yang, Ling Li, and Ming Liu. An analytical seebeck coefficient model for disordered organic semiconductors. *Phys. Lett. A*, 381(40):3441 – 3444, 2017.
- [81] J. C. Slater. The ferromagnetism of nickel. ii. temperature effects. *Phys. Rev.*, 49:931–937, Jun 1936.
- [82] A. Ślebarski. Electron-correlation effects in a disordered Fe₂TiSn Heusler alloy. *J. Phys. D: Appl. Phys.*, 39(5):856, 2006.
- [83] A. Ślebarski, M. B. Maple, E. J. Freeman, C. Sirvent, D. Tworuszka, M. Orzechowska, A. Wrona, A. Jezierski, S. Chizbaian, and M. Neumann. Weak ferromagnetism induced by atomic disorder in Fe₂TiSn. *Phys. Rev. B*, 62:3296–3299, Aug 2000.
- [84] A. Ślebarski, M. B. Maple, A. Wrona, and A. Winiarska. Kondo-type behavior in Fe_{2-x}M_xTiSn (M = Co, Ni). *Phys. Rev. B*, 63:214416, May 2001.
- [85] Piyada Suwanpinij, Audtaporn Worabut, Ratchadaporn Suprunangnet, and Hans Henning Dickert. Analysis of precipitation and dissolution of the microalloying elements by X-ray absorption spectroscopy (XAS). *AIMS Materials Science*, 4:856, 2017.
- [86] Yota Takamura, Ryosho Nakane, and Satoshi Sugahara. Analysis of L2₁-ordering in full-Heusler Co₂FeSi alloy thin films formed by rapid thermal annealing. *J. Appl. Phys.*, 105(7):07B109, 2009.
- [87] K. Ueda. Effect of magnetic field on spin fluctuations in weakly ferromagnetic metals. *Solid State Commun.*, 19(10):965 – 968, 1976.

- [88] David Vanderbilt. Soft self-consistent pseudopotentials in a generalized eigenvalue formalism. *Phys. Rev. B*, 41:7892–7895, Apr 1990.
- [89] E. Vilanova Vidal, H. Schneider, and G. Jakob. Influence of disorder on anomalous hall effect for Heusler compounds. *Phys. Rev. B*, 83:174410, May 2011.
- [90] S. H. Vosko, L. Wilk, and M. Nusair. Accurate spin-dependent electron liquid correlation energies for local spin density calculations: a critical analysis. *Canadian Journal of Physics*, 58(8):1200–1211, 1980.
- [91] S. M. Watts, S. Wirth, S. von Molnár, A. Barry, and J. M. D. Coey. Evidence for two-band magnetotransport in half-metallic Chromium dioxide. *Phys. Rev. B*, 61:9621–9628, Apr 2000.
- [92] Peter J. Webster. Heusler alloys. *Contemp. Phys.*, 10(6):559–577, 1969.
- [93] Shin Yabuuchi, Masakuni Okamoto, Akinori Nishide, Yosuke Kurosaki, and Jun Hayakawa. Large seebeck coefficients of Fe_2TiSn and Fe_2TiSi : First-principles study. *Appl. Phys. Express*, 6(2):025504, 2013.
- [94] E. A. Yelland, S. J. C. Yates, O. Taylor, A. Griffiths, S. M. Hayden, and A. Carrington. Ferromagnetic properties of ZrZn_2 . *Phys. Rev. B*, 72:184436, Nov 2005.
- [95] M. Zhang, S. Lenhert, M. Wang, L. Chi, N. Lu, H. Fuchs, and N. Ming. Regular arrays of copper wires formed by template-assisted electrodeposition. *Advanced Materials*, 16(5):409–413, 2004. cited By 68.
- [96] Xingfeng Zhu, Yaxu Wang, Lu Wang, Yafei Dai, and Chenglin Luo. Pressure and disorder effects on the half-metallic character and magnetic properties of the full-Heusler alloy Co_2FeSi .

Journal of Physics and Chemistry of Solids, 75(3):391 – 396, 2014.

- [97] Mohd Zubair Ansari and Neeraj Khare. Thermally activated band conduction and variable range hopping conduction in $\text{Cu}_2\text{CZnSnS}_4$ thin films. *Journal of Applied Physics*, 117(2):025706, 2015.
- [98] F. C. Zumsteg and R. D. Parks. Electrical resistivity of Nickel near the Curie point. *Phys. Rev. Lett.*, 24:520–524, Mar 1970.